# STUDYING NUCLEAR DEFORMATION DURING MIGRATION OF CELLS THROUGH CONFINING ENVIRONMENTS

A Dissertation

by

ADITYA KATIYAR

Submitted to the Graduate and Professional School of
Texas A&M University
in partial fulfillment of the requirements for the degree of

DOCTOR OF PHILOSOPHY

| | |
|---|---|
| Chair of Committee, | Tanmay P. Lele |
| Committee Members, | Kristen C. Maitland |
| | Wonmuk Hwang |
| | Pushkar P. Lele |
| Head of Department, | Michael J. McShane |

August 2022

Major Subject: Biomedical Engineering

# ABSTRACT

Fibroblasts, immune cells, and cancer cells migrating through pores and fibers in tissue must deform their cell nucleus in order to move. The role of the nuclear protein lamin A/C in limiting nuclear deformation and passage has been studied in pores and microchannels with a smooth contiguous surface. However, cells such as fibroblasts and cancer cells also encounter slender extracellular matrix fibers as they migrate through interstitial tissue. To study this process, we micro-fabricated closely spaced, flexible obstacles with bending rigidity similar to collagen fibers and imaged cell migration around these obstacles. In contrast to its limiting role in nuclear passage through confining channels, lamin A/C facilitated nuclear deformation and passage through fibrous environments because nuclei in lamin-null (*Lmna* $^{-/-}$) cells lost their overall morphology and became entangled around the obstacles. We propose that, analogous to surface tension-mediated deformation of a liquid drop, lamin A/C imparts a surface tension on the nucleus preventing nuclear entanglement and allowing nuclear passage through fibrous environments. We investigated a related long-standing question of how the cell shapes the nucleus in migrating cells. We cultured cells on surfaces with micro-patterned fibronectin such that narrow fibronectin lines (5 microns in width) culminated into wider rectangles. Nuclei in cells on 1-D lines had folds in the nuclear lamina, which disappeared as the cells migrated onto the 2-D rectangles and the nucleus reached a steady-state shape. These data confirmed the prediction of our previously proposed model that the resistance to nuclear shape changes in low so long as there are folds in the nuclear lamina. We also validated another model prediction- that the nuclear surface should move in response to local cell protrusions – through dynamic vertical imaging and tracking of protrusions and nuclear shapes in breast cancer cells. To address the errors in vertical imaging in these studies

due to the well-known phenomenon of refractive index mismatch, we developed a new approach for improved imaging of the x-z cross-section of fluorescent samples. Finally, we reported the discovery that Barrier-to-autointegration Factor (BAF) mediates the repair of the nuclear envelope after nuclear envelope rupture during confined cell migration.

DEDICATION

*To my advisor, who made me the researcher I am*

# ACKNOWLEDGEMENTS

I want to thank my advisor Dr. Tanmay Lele for his excellent mentorship, constant guidance, and unparalleled support during hardships, Dr. Richard Dickinson for his mentorship, and my committee members, Dr. Kristen Maitland, Dr. Wonmuk Hwang, and Dr. Pushkar Lele for their suggestions.

I am incredibly grateful to Dr. Qiao Zhang for teaching me the basics of experimental design, good lab practices and inspiring me to outperform myself, Dr. V.J. Tocco for directing me towards microfabrication which has become a substantial part of this dissertation, Dr. Andrew Tamashunas for helping me with programming, Dr. Yifan Yu for assisting me with analysis and Dr. Yuan Li for introducing me to several basic techniques.

I would also like to extend my gratitude to Brendan McKee, Siddhika Chunchuwar, Tanaya Roy, and Kelechi Ndukwe-Ajala for their assistance with experiments, and my lab members Purboja Purkayastha, Ting-Ching Wang, Christina Dubell, Kavya Pendyala, Julie Jameson, Dr. Sasanka Chukkapalli, Dr. Anurag Purushothaman, Dr. Ishita Singh and Dr. Pankaj Singh for making work a positive experience.

I am also grateful to my friends Sarthak Rout, Aditya Bharadwaj, Chintal Shah, Animesh Shah, and Dr. Sayane Shome for extending their friendship and being there for me during my ups and downs throughout this journey.

At last, I'd like to thank my parents for instilling in me a strong value system and high work ethic, giving me the best possible opportunities to learn and grow, training me to be able to walk this walk from an early age, thinking for me way above and beyond their self-interests and sacrificing whatever they could for my happiness.

CONTRIBUTORS AND FUNDING SOURCES

## Contributors

Microfabrication was supported by David Hays at the Nanoscale Research Facility, University of Florida, Gainesville. SEM imaging was performed at the Electron Microscopy Core, Interdisciplinary Center for Biotechnology Research at the University of Florida, Gainesville, and Microscopy and Imaging Center at Texas A&M University, College Station. A custom program to track the deflection of microposts described in Chapter 3, and the 3-D printed chamber to perform distortion-free axial imaging described in Chapter 5 were provided by Dr. Jyot D. Antani under the supervision of Dr. Pushkar P. Lele at Artie McFerrin Department of Chemical Engineering, Texas A&M University, College Station. 3-D collagen gel experiments described in Chapter 3 were performed in collaboration with Dr. Jian Zhang in the lab of Dr. Cynthia A. Reinhart-King at the Department of Biomedical Engineering, Vanderbilt University, Nashville. Dr. Kyle Roux's research group at Sanford Research, Sioux Falls, provided the data on laser-induced nuclear envelope rupture experiments (described in Chapter 4), engineered cell lines stably expressing fluorescent proteins and certain plasmids. Assistance in several experiments described in Chapter 2 and analyses was provided by Dr. Vincent J. Tocco, Dr. Yuan Li, Dr. Ian Kent, and Dr. Andrew C. Tamashunas.

All other work conducted for the thesis (or) dissertation was completed by Aditya Katiyar independently.

**Funding Sources**

This work was made possible in part by the National Institutes of Health (NIH) under Grant Number U01 CA225566, awarded to Dr. Tanmay Lele and Dr. Richard Dickinson, and a CPRIT established investigator award under Grant Number RR200043 awarded to Dr. Tanmay Lele. Its contents are solely the responsibility of the authors and do not necessarily represent the official views of the funding sources.

# NOMENCLATURE

| | |
|---|---|
| 1-D | One Dimensional |
| 2-D | Two Dimensional |
| 3-D | Three Dimensional |
| AFM | Atomic Force Microscopy |
| ANOVA | Analysis of Variance |
| ASTM | American Society for Testing and Materials |
| ATCC | American Type Culture Collection |
| BAF | Barrier-to-Autointegration Factor |
| BSA | Bovine Serum Albumin |
| CAD | Computer Aided Design |
| DBS | Donor Bovine Serum |
| DMEM | Dulbecco's Modified Eagle Medium |
| DMSO | Dimethyl Sulfoxide |
| DNA | Deoxyribonucleic Acid |
| DNMT | DNA methyltransferase |
| DPBS | Dulbecco's Phosphate Buffered Saline |
| ECM | Extracellular Matrix |
| EGF | Epidermal Growth Factor |
| ER | Endoplasmic Reticulum |
| FBS | Fetal Bovine Serum |

| | |
|---|---|
| FIJI | Fiji Is Just ImageJ |
| FWHM | Full Width at Half Maximum |
| GFP | Green Fluorescent Protein |
| HAT | Histone acetyltransferase |
| HEPES | N-2-Hydroxyethylpiperazine-N'-2-Ethanesulfonic Acid |
| LEM | LAP2, Emerin, MAN1 |
| MCF | Michigan Cancer Foundation |
| MDCK | Madin-Darby Canine Kidney |
| MEF | Mouse Embryonic Fibroblasts |
| N.A. | Numerical Aperture |
| NE | Nuclear Envelope |
| NHS | N-Hydroxysuccinimide |
| NIH | National Institutes of Health |
| NLS | Nuclear Localization Sequence |
| NMMII | Non-Muscle Myosin II |
| PBS | Phosphate Buffered Saline |
| PDGF | Platelet Derived Growth Factor |
| PDMS | Polydimethylsiloxane |
| PLL-g-PEG | Poly(L-lysine) graft Poly(Ethylene Glycol) |
| r-FN | Rhodamine-Conjugated Fibronectin |
| RFP | Red Fluorescent Protein |
| R.I. | Refractive Index |

| | |
|---|---|
| ROI | Region of Interest |
| SEM | Standard Error of Mean |
| WT | Wild-Type |
| v/v | Volume by Volume |
| w/v | Weight by Volume |
| w/w | Weight by Weight |

TABLE OF CONTENTS

Page

Page

LIST OF FIGURES

Page

Page

LIST OF TABLES

Page

# CHAPTER 1

# INTRODUCTION

Cell migration plays a central role in the development and maintenance of multicellular organisms. Migrating cells orchestrate early embryonic development, formation of blood vessels, tissue formation, regeneration and repair, immune response, and cancer metastasis. As cells migrate, they must navigate a heterogeneous tissue microenvironment, including extracellular matrices (ECM) proteins like collagen, fibronectin, laminin, and proteoglycans. These proteins oligomerize and cross-link to form fibrillar structures, the architectural meshwork of the tissue microenvironment, and pose obstacles to the migrating cells [1]. Consequently, the cell must deform itself to fit in between the interstitial spaces of ECM fibrils and migrate past them.

A major limiting component in cell deformation is the nucleus owing to its size and mechanical stiffness [2]. The stiff nuclear lamina and softer chromatin primarily contribute to the resistance of the nucleus to deformation [3-5]. Several lines of evidence suggest that the mechanical behavior of the nucleus is important for cell functions. For example, mutations in the *Lmna* gene that encodes lamin A and C are associated with a wide variety of human diseases, including laminopathies and Hutchinson-Gilford progeria syndrome. Lamins A/C levels decrease in a number of cancers, including colon cancer and breast cancer [6]. A decrease in lamin A/C levels is associated with nuclear softening [7-9], which may make nuclei more vulnerable to mechanical stresses from the extracellular microenvironment [10], and also contributes to altered nuclear shapes [11], which are a hallmark of human cancers. Lamin levels are also sensitive to the mechanical properties of the micro-environment [12], implying that lamins may play key roles in the process of

cell mechanotransduction. For example, the ratio of lamin A/C to lamin B1 correlates with tissue stiffness [13]; lamin A/C levels are low in the brain and high in muscle [13].

Furthermore, downregulation of nuclear lamin A/C promotes the possibility of nuclear envelope rupture under mechanical stress, and the resulting DNA damage can contribute to cancer progression [14,15]. Likewise, chromatin condensation causes an overall nuclear stiffening, while chromatin decondensation causes an overall nuclear softening. Chromatin decondensation promotes nuclear contour irregularities [5], which are common in cancer. Finally, the stiffness of the nucleus allows it to transmit mechanical stresses between different parts of the cell during cell migration [16,17], which is crucial for normal persistent migration. Thus, nuclear mechanics has emerged as central to a number of cellular functions and is important in the context of a number of human diseases. This motivates our interest in understanding how the nucleus behaves mechanically in cells.

Given the high mechanical stiffness of the nucleus (relative to the cytoplasm), that is conferred to it by nuclear lamins and chromatin, how cells with nuclei of typical sizes of 5-10 microns efficiently move through fibrous meshes with pore sizes as small as 10% of the nuclear size [2] is not fully understood. In particular, there is controversy over whether the deformed nucleus stores elastic energy in its deformed shape. Early tensegrity models of the cytoskeleton and the nucleus modeled the nucleus as storing elastic energy in its shape [18,19], implying that nuclear structural component such as the deformed nuclear lamina and chromatin store energy. Consistent with this hypothesis, rounding of trypsinized cells results in rounded nuclei, which supports the concept that flattened nuclei relax to a rounded shape upon release of the forces that keep them flattened. Mechanical force application with micropipette aspiration to nuclei [3,20,21] to deform

them, and then removal of the force results in a relaxation of the deformation, clearly showing that the nucleus can store elastic energy in its shape under applied forces by probes.

In contrast to the notion that the nucleus stores elastic energy in its deformed shape, collaborative work between the Lele laboratory and the Dickinson laboratory has resulted in the hypothesis that the nucleus is shaped irreversibly. This hypothesis implies that the nucleus does not store elastic energy that would cause it to recover its shape upon removal of external stress. The hypothesis was tested by removing the cell from around the nucleus of single elongated fibroblasts with micro-dissection [22]. There was no shape relaxation of the elongated nucleus long after removal of the cell [22]. Similarly, abnormally shaped breast cancer nuclei did not relax after removal of the cytoplasm. In a separate study, laser ablation was used to sever stress fibers that abut the nuclear surface in elongated fibroblasts. Again, laser ablation of stress fibers produced no expansion in the nuclear cross-section [16]. These findings seem to confirm the hypothesis that the nucleus stores no elastic energy in its shape inside cells. They also have important implications for the nature of the mechanical stresses that shape the nucleus and how nuclei become misshapen in cancer.

Chapter 3 provides new data that is further consistent with the hypothesis proposed by Lele, Dickinson, and co-workers. To study how the migrating cell deforms the nucleus, we developed a novel platform based on upright flexible PDMS microposts, which present barriers to cell migration. The posts have a flexural rigidity similar to that of single collagen fibers. Measurement of the deflection of the microposts allowed us to calculate the force on the nucleus as it deformed around the micropost. We found (1) lower forces for more significant and slow (many minutes) deformations of the nuclear surface as compared to AFM measurements taken on a shorter time scale (seconds), (2) a lack of correlation between force and invagination length at deeper

invaginations, (3) a liquid-like behavior of the nucleus where the shape of the nuclear lobes between the microposts was determined primarily by the nuclear pressure and surface tension mediated by lamin A/C, and (4) qualitative differences between nuclear shapes indented with a probe in several seconds and nuclear shapes that invaginate over several minutes around microposts in migrating cells. All these findings are consistent with the notion that any elastic energy stored in the deformed nuclear shape dissipates on the much longer time scale of cell migration [23].

A related long-standing question in the field of nuclear mechanics is how the migrating cell shapes the nucleus to fit it through confined spaces. The cell deforms the nucleus in such a way that the nuclear shape is approximately coordinated with the shape of the cell. For example, when cells are patterned into varying aspect ratios, elongated cells exhibit elongated nuclei [22,23]. Further, the degree of nuclear elongation scales with the degree of cell elongation. Competing models have been proposed to explain the coordination of cell and nuclear shapes. In one model, the shape of the nucleus is the result of a balance between compressive stresses exerted by actomyosin stress fibers abutting the nucleus and elastic restoring stress of the deformed nuclear shape [22,24-26]. In these models, differences in the nuclear shapes in cells with different degrees of elongation or spreading are typically explained by differences in the spatial distributions of the actomyosin stress fibers. The Lele and Dickinson laboratories have previously proposed an alternative viscous coupling model for stress generation on the nucleus, whereby movement of the cell boundaries transmits viscous stress through the intervening cytomatrix to a highly compliant nucleus [9,23,27]. A key feature of this model is that the surface area of the nuclear lamina is in excess of that of a sphere of the same volume, which is hypothesized to permit dynamic transitions between a wide range of shapes during spreading and migration. The excess surface area is

hypothesized to allow nuclear shape changes to mirror those of the cell with little mechanical resistance.

We tested the basic premise of this model by studying cell migration on micropatterned fibronectin shapes in Chapter 2. The patterns consist of long fibronectin lines (~5-micron width) terminating into wide fibronectin rectangles. Areas outside the fibronectin patterns are passive toward protein adsorption and therefore do not support cell adhesion. Cell culture on these fibronectin patterns results in elongated cells on the fibronectin lines (called 1-D lines due to their low aspect ratio) with elongated nuclei. The elongated nuclei featured folds in their nuclear lamina. When the elongated cells migrated from the 1-D lines to the wide 2-D rectangles, the narrow cell became wide, and the nucleus widened in response. Further, the nucleus stopped widening when the folds in the nuclear lamina disappeared. These results support our hypothesis that nuclear shape changes in cells occur till there is an excess area on the nuclear surface in the form of folds or wrinkles.

We also tested another prediction of the viscous coupling model in the context of cancer cells – that formation of cell protrusions proximal to the nuclear surface should cause stress on it, which can result in nuclear deformation. The Lele laboratory has shown previously that the process of cell spreading amplifies nuclear shape abnormalities in MDA-MB-231 breast cancer cells but not in non-malignant human mammary epithelial cells (MCF-10A) [23]. These findings suggest the hypothesis that cell protrusions may contribute, at least in part, to local abnormal nuclear deformations in breast cancer cells. In Chapter 2, we report the existence of vertical, apical cell protrusions in cultured MDA-MB-231 breast cancer cells which are absent in MCF-10A cells. These protrusions were associated with vertically upward nuclear deformations. Dynamic x-z confocal imaging of the cell membrane and the nucleus revealed that nuclear deformations

developed as a consequence of dynamic cell protrusion, and vertical nuclear shapes dynamically conform to vertical shapes of the cell boundary, again consistent with the viscous coupling model.

Because x-z confocal fluorescence imaging of nuclear and cellular cross-sections proved to be a powerful tool for testing our model, we next set out to develop methods to reduce the error associated with vertical imaging due to the well-known phenomenon of refractive-index mismatch. In chapter 5, we present a method to mount fluorescent samples parallel to the optical axis. This mounting allows direct imaging of what would normally be an x-z cross-section of the object in the x-y plane of the microscope. With this approach, the x-y cross-sections of fluorescent beads were observed to have significantly lower shape-distortions as compared to x-z cross-sections reconstructed from confocal z-stacks. We further tested the method for imaging nuclear and cellular heights in cultured cells and found that they were significantly flatter than previously reported. This approach enables improved imaging of the x-z cross-section of fluorescent cells and nuclei.

The migration of cells through narrow confining regions in tissue results in significant nuclear stresses that can rupture the nuclear envelope [14, 28]. The nuclear envelope (NE) separates and protects the nuclear contents like DNA from cytosolic DNA-damaging enzymes. Rupture in the NE allows free diffusion of these DNA-degrading enzymes, like endoplasmic reticulum (ER)-associated exonuclease TREX1 [15], into the nucleus, consequently causing damage to chromatin. This damage has been shown to promote invasive cancer cell migration [14,15], accelerated cell senescence [15], and has also been implicated in laminopathies [29] and auto-immune diseases [30]. Cells have intrinsic mechanisms to restore the nuclear envelope integrity to minimize the damage to chromatin. A previous study [14] identified the role of a family of proteins, called the endosomal sorting complexes-III (ESCRT-III) proteins, in mediating the repair process, but the mechanism

by which these protein complexes are recruited to the repair site, as well as their role in repair, is not well understood. To better understand envelope repair, we imaged confined cell migration in a microfluidic device previously described in [31]. Dynamic imaging of migrating fibroblasts stably expressing relevant fluorescent proteins (like GFP-BAF and mCherry-NLS or GFP-NLS) showed that Barrier-to-autointegration factor (BAF), a protein that cross-bridges two strands of nuclear dsDNA and promotes DNA compaction [32], plays a key role in the repair of the nuclear membrane. These results are discussed in Chapter 4.

# CHAPTER 2

# OBSERVATIONS OF NUCLEAR DEFORMATION CAUSED BY CELL PROTRUSION [*]

## 2.1 Overview

The mechanisms by which mammalian nuclear shape and size are established in cells and become abnormal in disease states are not understood. Here, we tracked motile cells that underwent systematic changes in cell morphology as they moved from 1-D to 2-D micro-patterned adhesive domains. The motion of the cell boundaries during cell motility caused a dynamic and systematic change in nuclear volume. Short time scales (~ 1 h) distinguished the dilation of the nucleus from the familiar increase that occurs during the cell cycle. Nuclear volume was systematically different between cells cultured in 3-D, 2-D, and 1-D environments. Dilation of the nuclear volume was accompanied by dilation of chromatin, a decrease in the number of folds in the nuclear lamina, and an increase in nucleolar volume. Treatment of 2-D cells with non-muscle myosin-II inhibitors decreased cell volume and proportionately caused a decrease in nuclear volume. These data suggest that nuclear size changes during cell migration may potentially impact gene expression through the modulation of intranuclear structure.

## 2.2 Introduction

Nuclear mechanics and morphology are characteristic of cell phenotype and become significantly abnormal in human pathologies. Unlike the smooth, ellipsoidal shape of normal



[*] Reproduced from "Katiyar, A., Tocco, V. J., Li, Y., Aggarwal, V., Tamashunas, A. C., Dickinson, R. B., & Lele, T. P. (2019). Nuclear size changes caused by local motion of cell boundaries unfold the nuclear lamina and dilate chromatin and intranuclear bodies. Soft matter, 15(45), 9310–9317. https://doi.org/10.1039/c9sm01666j" with permission from the Royal Society of Chemistry.

Reproduced from "Kent, I.A., Zhang, Q., Katiyar, A., et al. Apical cell protrusions cause vertical deformation of the soft cancer nucleus. J Cell Physiol. 2019; 234: 20675– 20684. https://doi.org/10.1002/jcp.28672" with permission from John Wiley & Sons, Inc.

nuclei, cancer nuclei tend to have highly abnormal nuclear shapes with irregular contours consisting of lobes and invaginations 10,35, which have prognostic and diagnostic significance 36. The mechanisms by which nuclear shape becomes abnormal in human pathologies are not fully understood [33,34] but are thought to be related to changes in cell and nuclear mechanics [35].

In addition to nuclear shape, nuclear size, as measured by its volume, also becomes significantly altered in human pathologies like cancer (reviewed in [36]). These alterations to nuclear size are not primarily due to alterations to DNA [37]; rather, a key determinant of nuclear size in cells is the cytoplasmic volume. For example, nuclear size or volume has been shown to correlate with cell size in yeast [38,39]. Similarly, nuclear volume scales with cytoplasmic volume in *Xenopus* egg extracts [40]. In *Xenopus*, nuclear size sensitivity to the amount of cytoplasm around it may be due to the availability of cytoplasmic factors such as importin α [41] and dynein-dependent transport of lipid membranes [40]. Consistent with these studies, osmotically induced changes to cell volume cause proportionate changes to nuclear volume [42,43].

Changes to actomyosin tension can also alter nuclear volume [19,27,44]. Because actomyosin tension is dynamically modulated during cell migration [45,46], here we examined the extent to which local and dynamic changes in cell shape cause changes in nuclear volume. There was a substantial increase in nuclear volume as cells crawled on fibronectin-coated patterns from 1-D lines to 2-D rectangles. Nuclear dilation was accompanied by a corresponding decrease in folds in the nuclear lamina and dilation of chromatin and intranuclear bodies. Myosin inhibition reduced cell volume and caused a proportionate decrease in nuclear volume. These results demonstrate that nuclear size and intranuclear structure are dynamically controlled during cell crawling.

## 2.3 Dynamic changes in nuclear volume are driven by changes in cell shape during cell migration

Fibroblasts *in vivo* have markedly elongated nuclear shapes, as seen in stained cross-sections of tissue. Such elongated, physiologically relevant phenotype of fibroblasts can be reproduced by culture in 3-dimensional collagen gels. We observed instances in collagen gel culture in which a narrow, elongated fibroblast locally widened as it migrated (an example is in Figure 1A). The shape of the GFP-histone H1.1 labeled nucleus coincided closely with the local shape of the cell; as the cell began to widen near the nucleus, the nucleus widened as well (yellow arrow in Figure 1A). To study this shape-change more reproducibly, we micro-patterned the surface of a polymer coverslip with a fibronectin shape (Figure 1B) consisting of a 5-micron-wide line (1-D) of sufficiently long length terminating in a 50-micron by 100-micron rectangle (2-D) (Figure 1B). This pattern enabled the imaging of highly elongated fibroblasts on the narrow ("1-D") region as they approached and moved onto the broader ("2-D") region.

We performed laser-scanning confocal fluorescence microscopy of the GFP-histone labeled nucleus during migration from the 1-D to 2-D region and examined the x-z and x-y views of the nucleus (Figure 1C). Cell nuclei expanded in the cross-sectional area when they reached the interface between the 1-D and 2-D regions, coinciding closely with the widened local cell shape (Figure 1C, x-y view). As nuclei translated during migration from the 1-D to the 2-D region, the height decreased slightly (x-z plane images in Figure 1C) while the cross-section area in the x-y plane widened significantly (x-y plane images in Figure 1C). Such a significant increase in the area of the cross-section was observed consistently across several cells over the ~ 450 min of migration from 1-D to the 2-D region (see pooled data in Figure 1D). We quantified the nuclear volume from confocal z-stacks during the migration and observed a nearly 20% increase upon

migration from the 1-D to the 2-D region (Figure 1D, see also materials and methods for volume measurements and reference [27]). These results suggest that a widening of the cell shape during cell migration, which drives the widening of the local nuclear shape, can increase the volume of the nucleus. The relatively short timescale of the volume changes (within 75 minutes) and the fact that they occur reproducibly upon migration from the 1-D to the 2-D pattern argues against the possibility that the nuclear volume changes are cell-cycle related. Also, these volume changes did not occur over a similar time frame when cells were on the 1-D line (Figure 1D, -180 min to 0 min).

Fibroblasts on 1-D lines are more elongated than cells on 2-D areas, while fibroblasts in 3-D culture tend to have branched shapes. Given these differences in cell shape, we compared nuclear volumes between fibroblasts cultured overnight and then fixed on micropatterned fibronectin lines, on tissue culture dishes, inside three-dimensional collagen gels, and on the surface of these gels. There were systematic differences in nuclear volume in these different culture conditions. Nuclear volumes on the 1-D lines and on the collagen gel surface were similar and lower than the volume on 2-D tissue culture dishes, which was, in turn, lower than the volume in 3-D gels (Figure 1E). These experiments reveal that there are systematic differences in fibroblast nuclear volume in different culture conditions.

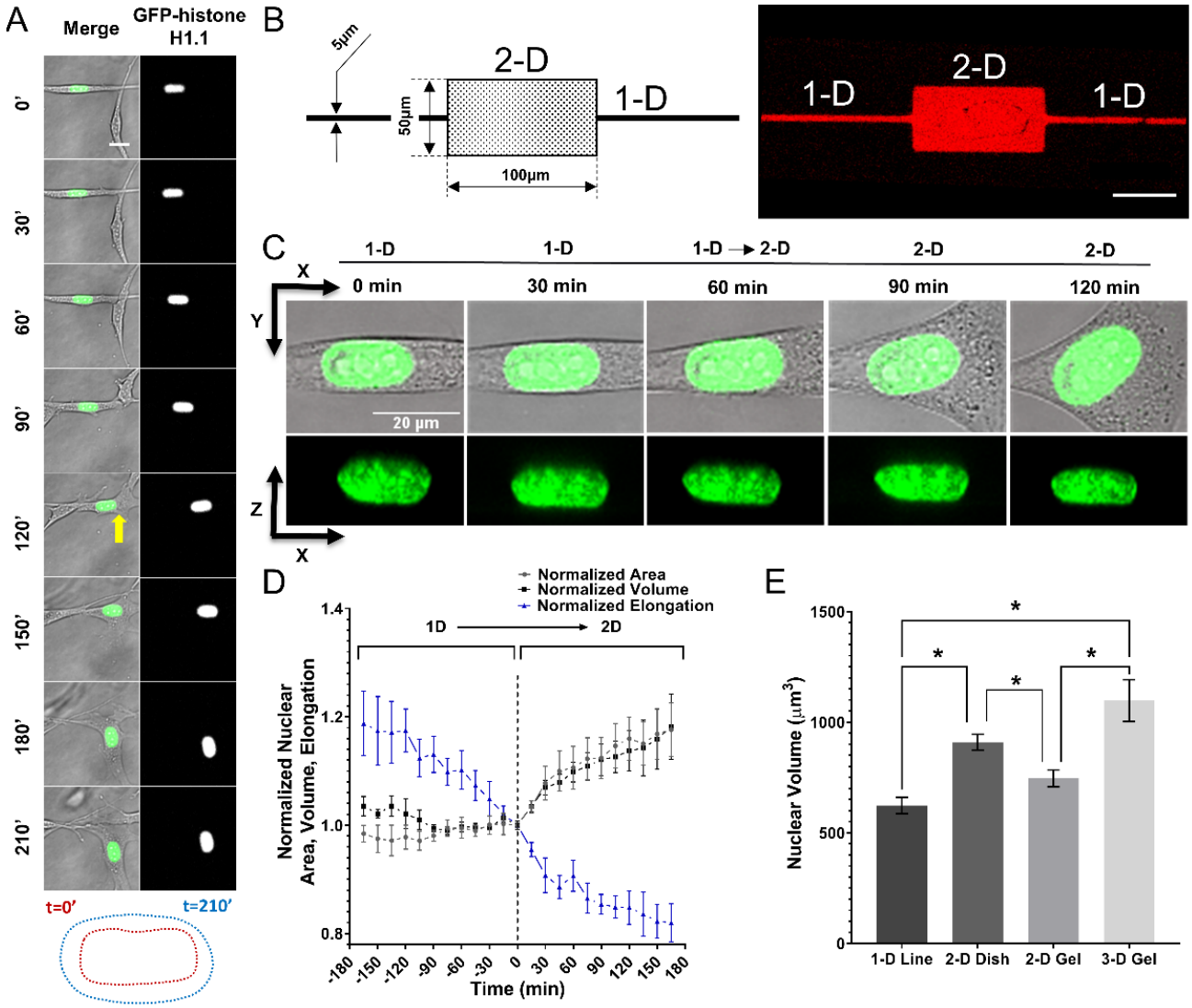


**Figure 1. Nuclear volume in migrating cells and in different culture conditions. (A) A migrating NIH3T3 fibroblast expressing GFP-histone H1.1 in 3-D collagen gel. The yellow arrow indicates local cell widening accompanied by nuclear widening. Scale bar is 20 μm. Dotted lines show a comparison between the nuclear boundary at time 0 and 210 minutes. (B) Left: Design of the pattern on a silicon master wafer used to make PDMS negative molds for micro-patterning. Right: An image of rhodamine-fibronectin micropatterned into 5-μm-**

**wide 1-D lines that terminate into a 2-D rectangle. Scale bar is 50 µm. (C) Image shows x-y and x-z cross-sections of a GFP-histone H1.1 expressing nucleus as it migrates from the 1-D line to a 2-D rectangle. Scale bar is 20 µm. (D) Pooled plots of nuclear volume, nuclear x-y area, and nuclear x-y elongation (measured as width/length) over time during the transition from the 1-D to 2-D shapes. The time data for all cells was corrected such that t=0 is the time at which the leading edge of the nucleus reached the edge to the 2-D fibronectin pattern. Data are mean ± SEM for 8 cells from at least 4 different experiments. (E) Nuclear volume of NIH 3T3 cells on 1-D fibronectin lines (36 cells), fibronectin-coated culture dishes (43 cells), upon collagen gels (34 cells), and cultured within collagen gels (36 cells). Data are mean ± SEM from three independent experiments. *p<0.05 with Student's *t*-test.**

### 2.4 Nuclear expansion dilates chromatin, unfolds the nuclear lamina, and alters nuclear bodies

Chromatin is molecularly linked to the nuclear lamina[47], which suggested to us that the observed increase in nuclear volume during migration could cause dilation of chromatin. To test this hypothesis, we examined the fate of regions of chromatin in the nucleus as the nucleus dilated during cell migration from 1-D to 2-D fibronectin patterns. Chromatin regions were tracked by photoconverting Dendra2-Histone H3.3, a protein stably integrated into nucleosomes[48], in defined spatial regions, and then imaging its dynamics during nuclear shape changes. We first confirmed that the protein did not exchange and lose fluorescence in the photoactivated spot by tracking the fate of photoactivated Dendra2-Histone H3.3 in fibroblasts. The photoactivated pattern was stable and did not blur over a time scale of two hours (Figure 2), which is longer than the time scale for nuclear widening (compare with Figure 1C and D).

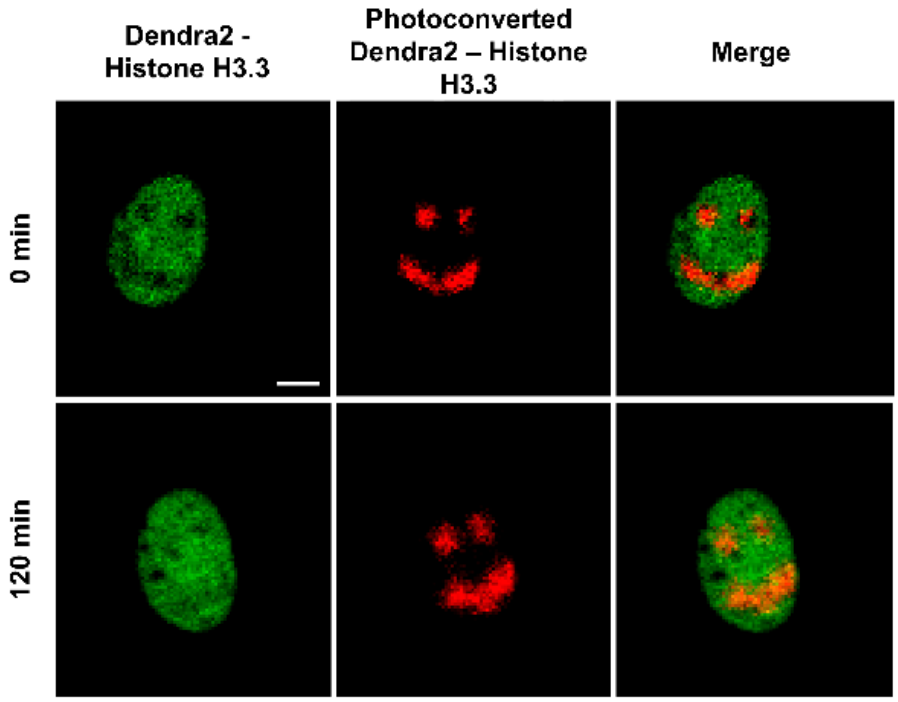


**Figure 2. Images show photoconverted Dendra2-Histone H3.3 in a single fibroblast in a defined pattern tracked for 2 hours. Scale bar is 10 µm.**

Next, we tracked the change in the shape of a photoconverted spot as the nucleus migrated from the 1-D to the 2-D region. Because photoconversion is not confined to a single plane, we performed confocal imaging and captured multiple planes at different z-positions. Figure 3A shows a time-lapse image sequence of a typical nucleus in which there is a clear expansion of the photoactivated spot upon nuclear expansion. Further, the photoconverted spot in each confocal plane underwent a similar expansion (Figure 3B and C). We pooled measured areas in different imaging planes and at different times from multiple cells migrating from 1-D to 2-D patterns and found a strong correlation between normalized spot area and normalized nuclear area (Figure 3D). These data collectively show that nuclear widening during cell migration causes chromatin expansion.

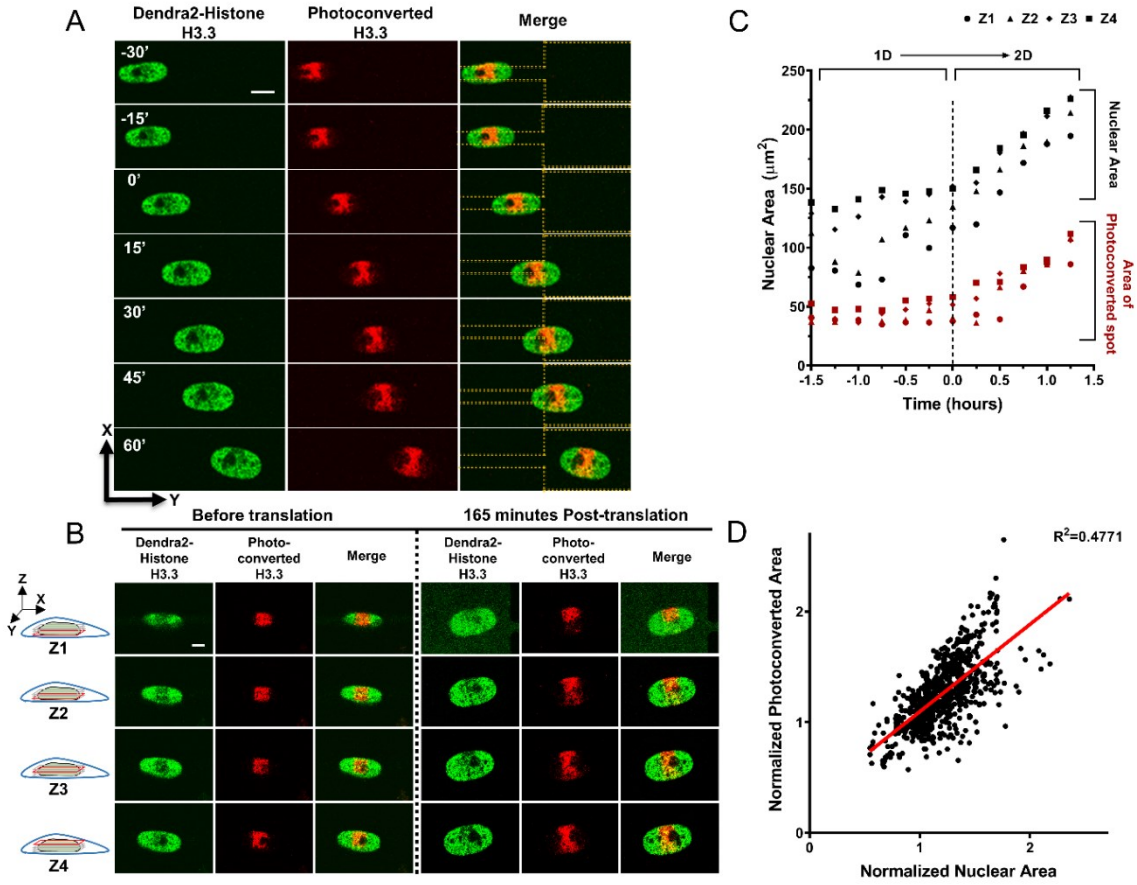


**Figure 3. Chromatin dilation during 1-D to 2-D migration. (A) Images show a photoconverted Dendra2-Histone H3.3 spot in an elongated nucleus in a cell on the 1-D fibronectin line, and the same nucleus tracked over time during and after translation onto the 2-D fibronectin area. Scale bar is 10 µm. (B) Images of the photoconverted spot in distinct confocal planes imaged at different vertical (z-axis) positions. Scale bar is 5 µm. (C) Quantification of nuclear area and area of a photoconverted spot in the different image planes in figure 3B over time. (D) Scatterplot of normalized photoconverted area versus normalized nuclear area; data were pooled from time-lapse images of 8 different Dendra2-Histone H3.3 expressing cells that migrated from 1-D to 2-D patterns. The red line was determined by linear regression; $R^2 = 0.4771$.**

We asked if changes in nuclear volume in 1-D and 2-D cells altered the geometry of chromatin-associated structures in the nucleus. Consistent with the expansion of chromatin, Srm160 labeled splicing speckles that reside in interchromatin spaces [49] underwent a dynamic translation away from each other during the nuclear expansion (Figure 4A). However, quantitative comparisons of speckle geometry and volume between 1-D and 2-D nuclear shapes proved to be unreliable owing to their small size and also network-like appearance in the nucleus. We therefore chose to quantify the volume of nucleoli stained for fibrillarin, which had a more condensed and discrete appearance in the fibroblast nucleus (Figure 4B). Total nucleolar volume per cell was larger in 2-D culture than in 1-D culture, consistent with the corresponding nuclear volume differences. These results show that nuclear volume dilation caused by local widening of the cell body causes a dynamic dilation of intranuclear structures like chromatin, nucleoli, and intranuclear bodies like splicing speckles, all of which may potentially alter key cellular processes like gene expression.

We have previously proposed that the flattening of the nucleus during cell spreading reaches a steady state when the wrinkled nuclear lamina in the rounded nucleus becomes fully unfolded during the process of flattening. As the nucleus similarly reached a steady-state shape after migrating from the 1-D to the 2-D pattern, we examined the spatial distribution of GFP lamin A in fibroblasts during the migration. Figure 4C shows a single nucleus migrating from the 1-D pattern to the 2-D pattern. On the 1-D pattern, folds were observed in the GFP lamin A expressing nucleus throughout the time it was on the 1-D line.

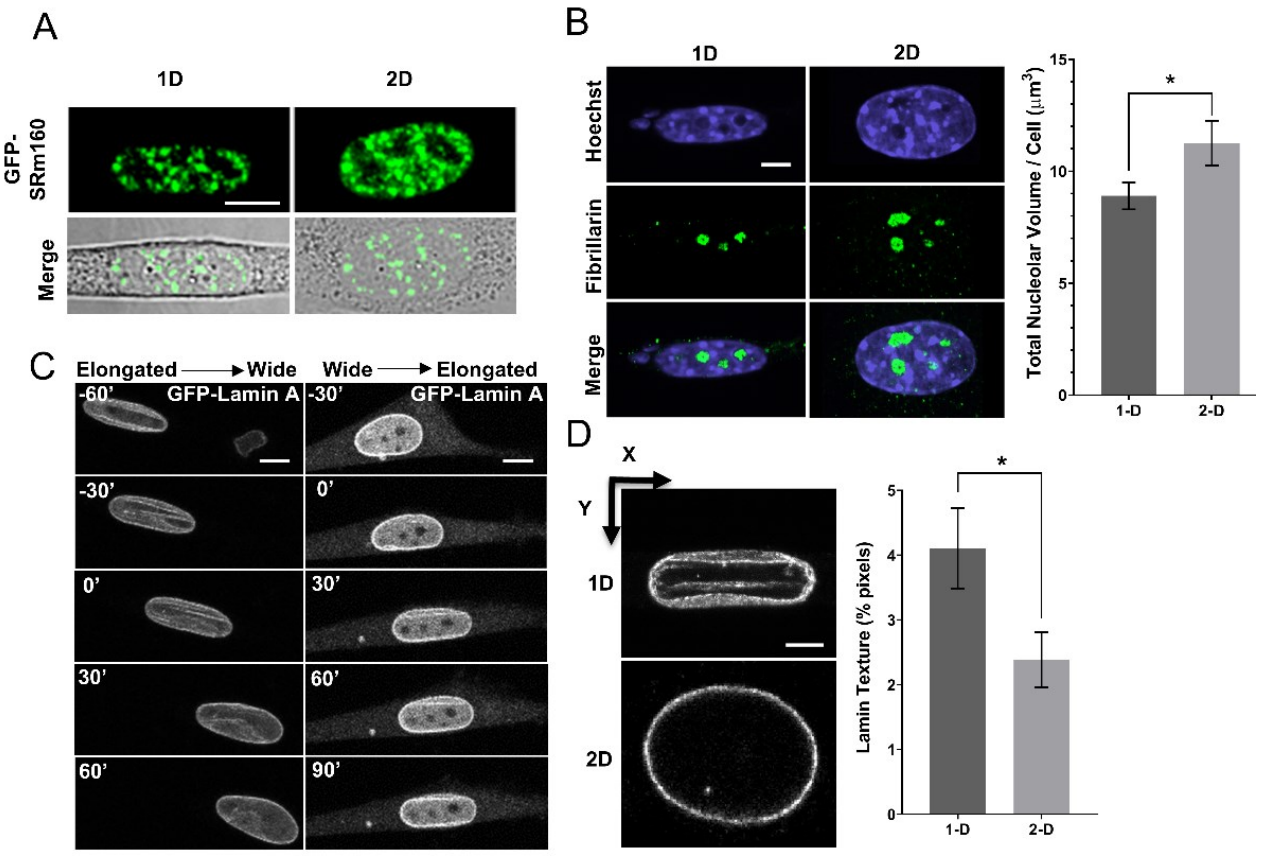


**Figure 4. Dilation of nuclear contents and unfolding of the nuclear lamina during the 1-D to 2-D transition. (A) Images of an NIH 3T3 fibroblast nucleus expressing splicing speckle protein GFP-SRm160 on the 1-D fibronectin line and subsequently on the 2-D region, along with overlays of the two images. Scale bar is 10 µm. (B) Images of fibroblast nuclei on 1-D fibronectin lines or 2-D fibronectin regions fixed and stained for fibrillarin, a nucleolar protein (green). Nuclei were counter-stained for DNA with Hoechst (blue). Scale bar is 5 µm. Plot compares total nucleolar volume per cell on 1-D lines (n = 43 cells from 3 independent experiments) and on 2-D fibronectin regions (n= 38 cells from 3 independent experiments). Data is mean ± SEM ($p < 0.05$ by Student's t-test). (C) Time-lapse images of a NIH 3T3 fibroblast stably expressing GFP Lamin A translating from a 1-D line to 2-D area (left column) and from a 2-D area to the 1-D line (right column). Scale bar is 10 µm. (D) Images**

**of representative fibroblast nuclei on a 1-D line or 2-D area immunostained for lamin A/C. Scale bar is 5 µm. Plot shows lamin texture calculated as pixels in texture/total nuclear pixels x 100 in cells cultured on 1-D lines and 2-D areas. n=34 cells on 1-D line and n=36 cells on 2-D area; *$p$ <0.05 by Student's t-test. See materials and methods for details of the texture calculation.**

These folds gradually disappeared as the nucleus widened during the transition from the 1-D to the 2-D pattern (Figure 4C left panel). The texture in the GFP lamin A images (corresponding to folds, wrinkles, holes, etc.) disappeared from each of the confocal planes imaged during the transition (Figure 5A) while, in the reverse transition of the cell from a 2-D area onto 1-D line; the folds reappeared (Figure 4C, right). Also, immunostaining of lamin A/C revealed consistent folds/wrinkles in the nucleus on 1-D lines. In contrast, these folds were largely absent in nuclei on 2-D areas (Figure 4D). We quantified texture in the nuclear cross-section as the number of pixels in grooves, folds, holes, and wrinkles (excluding the nuclear periphery; see figure 5B and methods for more information). There was a statistically significant reduction in the texture on 2-D areas compared to 1-D lines (Figure 4D). These results show that nuclear widening during migration is accompanied by the dynamic unfolding of the nuclear lamina, consistent with similar observations during nuclear flattening[9] and during stretching of isolated nuclei [3].

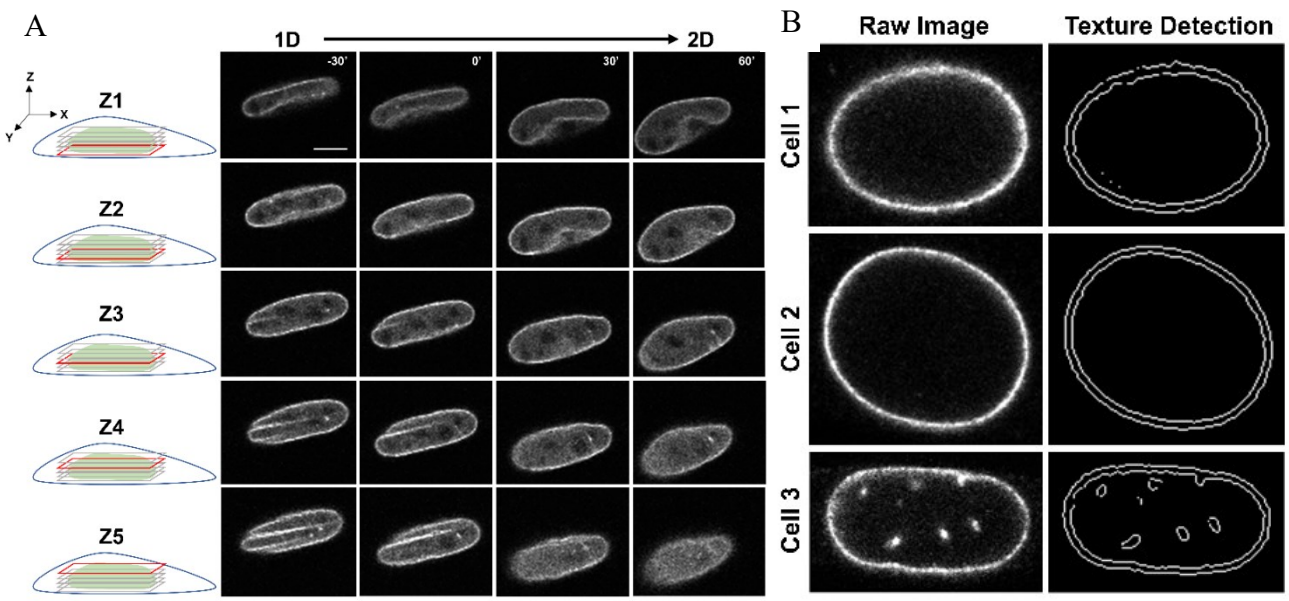


**Figure 5. Dynamics of lamin A/C wrinkles across nuclear height as the cell migrates from 1-D to 2-D region and examples of lamin texture detection. (A) Time-lapse images at different z-planes of the migrating GFP-Lamin A expressing fibroblast in Figure 4C. Scale bar is 10 μm. (B) Representative images of the detection of folds, grooves, and holes (termed texture) in the nuclear lamina. Images of the lamin A/C immunostained nucleus were taken at the equatorial plane of the nucleus, segmented using a custom algorithm in MATLAB and the number of texture pixels in the interior of the nuclear lamina (excluding the nuclear envelope) was quantified and used to calculate a lamin texture percentage.**

### 2.5 Nuclear volume correlates with cell volume

Changes in actomyosin tension alter nuclear volume [27,44]. For example, inhibiting myosin in fibroblasts spread on 2-D surfaces substantially reduced nuclear volume [27], while inhibiting myosin in endothelial cells on 1-D lines increased nuclear volume [50]. Further, nuclear volume scales proportionately with cell volume [38,39,43,51,52]. Considering these previous studies, we reasoned that one potential mechanism for the observed differences in nuclear volume under different culture conditions and during cell widening during migration might be that the actomyosin-tension-dependent cell volume is correspondingly altered under different culture conditions. However, reliable quantification of cell volume in cell shapes that vary widely in the different culture conditions proved to be difficult owing to the thin lamella and lamellipodia that are frequently below the z-resolution of the confocal microscope and the branched three-dimensional morphologies in 3-D culture.

Motivated by the fact that volume measurements of rounded nuclei and rounded cells are far less limited by the difficulties of imaging lamellipodia, we devised an approach to quantify correlations between nuclear and cell volume and the effects of inhibiting actomyosin tension on these properties. Spread cells were treated with three different types of pharmacological drugs, ML-7, a myosin light chain kinase inhibitor, blebbistatin, an inhibitor of non-muscle myosin II (NMMII) activity, and Y-27632, a Rho-kinase inhibitor for 60 minutes which allows efficient inhibition of NMMII in spread cells [53]. Any potential changes to cell volume and nuclear volume were likely to occur over this time period in NIH 3T3 fibroblasts [27]. Thereafter, cells were trypsinized and resuspended in fresh media in the presence of these inhibitors and seeded on glass-bottomed dishes. Next, these cells were fixed at around 10 minutes after cell seeding, which allowed sufficient time for cell adhesion but not spreading (Figure 6A). Cells were round, and

nuclei were correspondingly round at 10 minutes into the spreading process. There was a near absence of thin lamellar structures in these cells (Figure 6A).

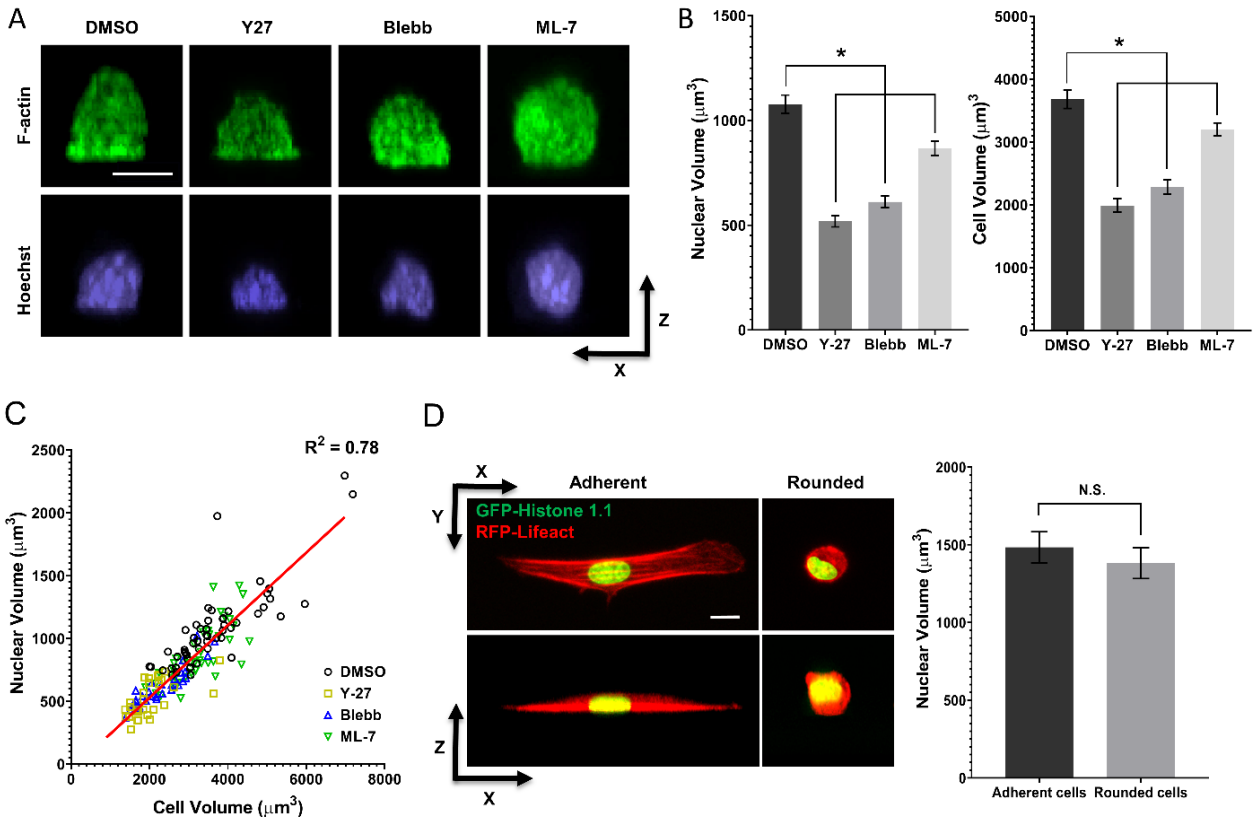


**Figure 6. Nuclear volume scales with cell volume. (A) Representative x-z images of the nucleus (blue, stained for DNA with Hoechst 33342) and the cell (green, stained for F-actin with Alexa Fluor-488phalloidin) treated with 25 µM ML-7, a myosin light chain kinase inhibitor, 50µM blebbistatin, an inhibitor of myosin activity, and 25 µM Y27632, a Rho kinase inhibitor or DMSO control for 1 hour, before trypsinization and subsequent seeding on glass-bottomed dishes for 10 minutes, followed by fixation. Scale bar is 10 µm. (B) Quantification of cell and nuclear volume in the experiments corresponding to figure 6A. Cell numbers quantified for DMSO, Y27, Blebb, and ML-7 were 55, 30, 30, and 45,**

**respectively. Data is from three independent experiments. Data is mean ± SEM; *$p$ <0.05 by Student's t-test. (C) Scatter plot of nuclear volume versus cell volume from the data in figure 6B. The red line was determined by linear regression; $R^2$ = 0.78. (D) Measurements of nuclear volume after cell rounding due to trypsinization. GFP-Histone H1.1 tagged NIH 3T3 fibroblasts were detached from the dish by adding 0.083 % trypsin. Cells were imaged with confocal microscopy until the cell became rounded. Representative images show the change of cell shape (red, RFP-Lifeact) and nucleus (green, GFP-Histone1.1) in x-y and x-z views before (adherent) and after trypsinization (rounded). Scale bar is 10 μm. Plot shows quantification of nuclear volume in adherent and rounded cells. All data are mean ± SEM from 14 different cells. N.S. signifies $p$ > 0.05 by the student's $t$-test.**

Treatment with each of these drugs significantly reduced nuclear volume and also reduced cell volume (Figure 6B). There was a clear correlation between cell and nuclear volume under these treatment conditions (Figure 6C). Somewhat surprisingly, however, trypsinization of cells which has been suggested to cause a decrease in nuclear volume [44], had no corresponding effect on nuclear volume (Figure 6D), which suggests that rapid relaxation of actomyosin tension is not sufficient to alter cell and nuclear volume. These results collectively suggest that nuclear volume changes caused by inhibition of actomyosin tension are correlated with cell volume changes.

### 2.6 Conclusion

Elongated mammalian cells tend to contain elongated nuclei, while circular cells contain rounder nuclei in different cell types [23,50]. Wide cell and nuclear shapes prevent extravasation through tight spaces in the extracellular matrix while narrowing of the nucleus due to local cell constriction allows migratory escape [2]. The coordination between mammalian cells and nuclear shape is driven by the motion of cellular boundaries toward and/or away from the nuclear surface

[23,27]. There have been contrasting reports on the effect of cell shape and mechanics on nuclear volume. Nuclear volume was low in elongated micropatterned primary human umbilical vein endothelial cells [50], while it was unchanged with elongation of human lung microvascular endothelial cells [54]. Nuclear volume was constant during the dynamic process of fibroblast spreading [27] and during the squeezing of wild type and lamin A/C deficient fibroblasts through narrow pores [31] but increased during the spreading of microvascular endothelial cells [54]. Here, we show that a significant nuclear volumetric dilation is caused by the local outward motion of cellular boundaries during fibroblast migration from 1-D to 2-D fibronectin patterns. This dilation is accompanied by the dilation of chromatin and other sub-nuclear structures like splicing speckles and nucleoli and an unfolding of the nuclear lamina. Our observations are consistent with previous observations that nuclear volume scales inversely with the degree of elongation in micropatterned endothelial cells [54].

We found that the volume of the nucleus is proportional to cell volume in cells allowed to adhere for very short times (Figure 6). Furthermore, actomyosin inhibition reduced cell volume and proportionately reduced nuclear volume. In these experiments, we trypsinized cells and allowed them to adhere but not spread on culture dishes. However, we found it difficult to measure changes in cell volume during the migration or in different culture systems owing to errors introduced during the imaging of thin lamellipodia and/or irregular cell structures. Based on several recent studies in other systems which show that nuclear size is primarily determined by cytoplasmic volume [38,40,41,43], and the fact that actomyosin tension is lower in elongated cells compared to more circular cells [54], it is reasonable to speculate that the changes in nuclear volume during cell migration and in different culture conditions are a secondary effect of changes to cell volume caused by differences in actomyosin tension. Cell volume may not change during the

process of spreading or migrating through tight spaces, which may explain why the nuclear volume is unchanged during these processes [27,31]. How cell volume might be altered differentially in these different situations is unclear at present but is likely related to the overall actomyosin tension and the impact of actomyosin activity on mechanical properties [55] of the cell.

We also found systematic differences in nuclear volume in different modes of culture, which are consistent with the corresponding elongated vs. rounder nuclear phenotypes. In these different culture conditions, nuclear volume differences and associated alterations to intranuclear structure [56] could potentially contribute to the systematic differences in gene expression and cell function between 2-D and 3-D cultures [57-61]. Mechanical forces applied to the nuclear surface through magnetic manipulation of beads bound to the cell surface have been shown to stretch chromatin in the nucleus locally and thereby alter gene expression [62]. Migration of cells through constricted spaces stretches chromatin [63], causing nuclear rupture [14,28,64,65] and DNA damage [66]. Dynamic changes to the nuclear size and associated intranuclear structure during cell motility may be an additional mechanism that impacts cell and nuclear functions.

**2.7 Understanding nuclear shape abnormalities in cancer cells**

Human cancers are characterized by changes to the nuclear shape, such that the normally smooth nuclear contour becomes highly irregular. To explore how cancer nuclei may become abnormal in culture, we studied and compared the establishment of nuclear shape in normal cells and cancer cells. In two-dimensional culture, single nonmalignant mammary epithelial MCF-10A cells that are considered to have a near-normal phenotype [67-70] exhibited a typical vertical shape (x-z profile) with the cell being tallest over the nucleus and becoming flatter gradually, farther away from the nucleus (Figure 7, top panel) consistent with previous observations by the Lele laboratory [9,27]. The nucleus resembled a flattened ellipsoid in these cells. While around 90% of

breast cancer MDA-MB-231 cells exhibited a similar x-z profile, in the rest of the MB-231 cells, a cell membrane protrusion was present at the apical surface (hereafter called apical cell protrusion, Figure 7). In all MB-231 cells with apical protrusions, the apical surface of the nucleus was deformed into the apical cell protrusion. The deformed nuclei displayed a negative curvature near the opening to the apical cell protrusion mimicking the negative curvature in the cell protrusion (marked by white arrows in Figure 7). Notably, in the x-y plane, cells with such apical protrusions were well-spread, which gave a "Mexican-hat" type appearance to cells in the x-z plane.

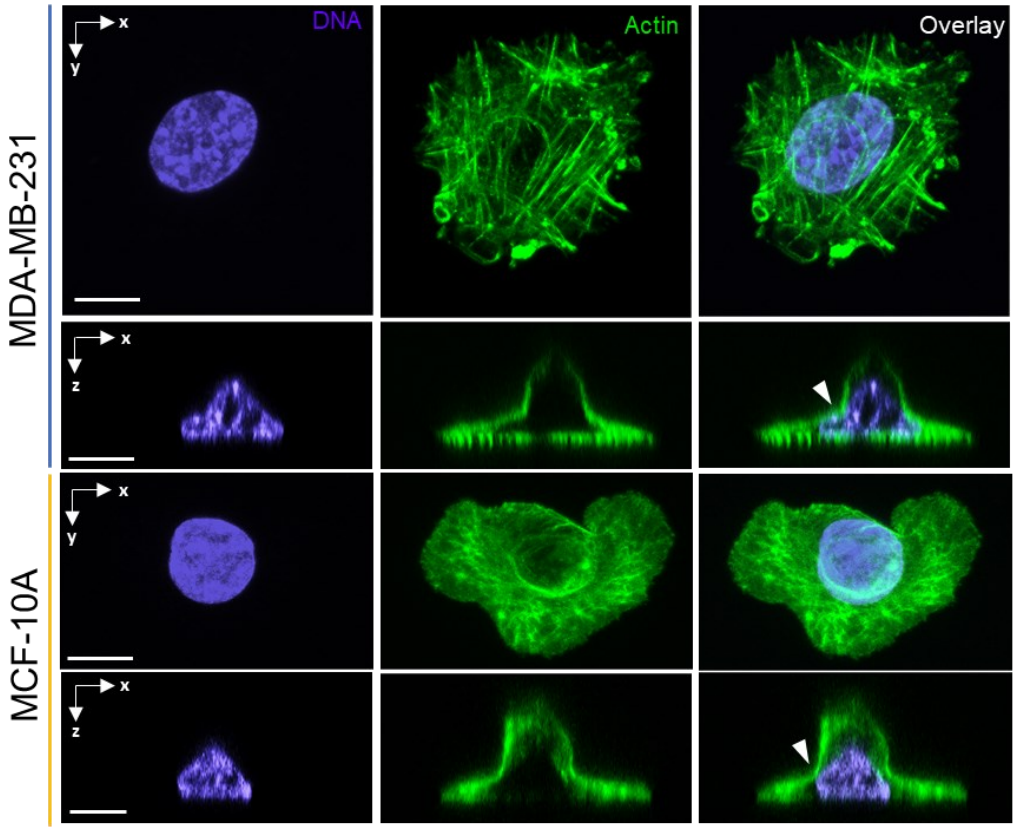


**Figure 7. The presence of apical cell protrusions with associated nuclear deformation in MB-231 cells. Images show representative fluorescent images of x-y and x-z cross-sections of an MCF-10A cell (top) and MB-231 cells (bottom). The MB-231 cell has a 'Mexican hat' type appearance due to the local apical cell protrusion in an otherwise well-spread cell.**

Cell protrusions in the x-y plane of the cell proximal to the nuclear surface cause local nuclear deformations in the direction of protrusions [16,23]. Relaxation of cell protrusions causes relaxation of nuclear deformations. To test if vertical apical protrusions precede vertical nuclear deformation, we imaged the dynamic formation of apical cell protrusions and the vertical shape of the NLS-GFP expressing nucleus using confocal fluorescence microscopy. In these experiments, we treated MB-231 cells with nocodazole to enrich apical cell protrusions. Figure 8 shows the dynamic formation of an apical protrusion upon nocodazole addition at time t = 0 min, and the corresponding x-z nuclear profiles tracked by staining lipid membranes with DiI (a lipophilic tracer used to visualize the cell membrane). The nucleus can be seen to round up vertically with changes to the vertical cellular shape. At around 20 min, a small apical protrusion develops that subsequently becomes large, and a significant portion of the nucleus is drawn into the protrusion. These results demonstrate that the apical protrusions form first, followed by vertically upward deformation of the nucleus.

We also tracked the F-actin network using RFP-Lifeact during the development of the vertical protrusion (Figure 8), and observed similar behavior where the vertical shape of the nucleus roughly mimicked the vertical shape of the cell. Extension of the apical surface of the nucleus extended the apical surface, whereas relaxation caused the apical nuclear surface to relax back. No F-actin stress fibers were visible in these cells on top of the nucleus. Inward movement of the boundaries in the basal plane and their outward movement in the apical plane correlate with changes in the shape of the nucleus.

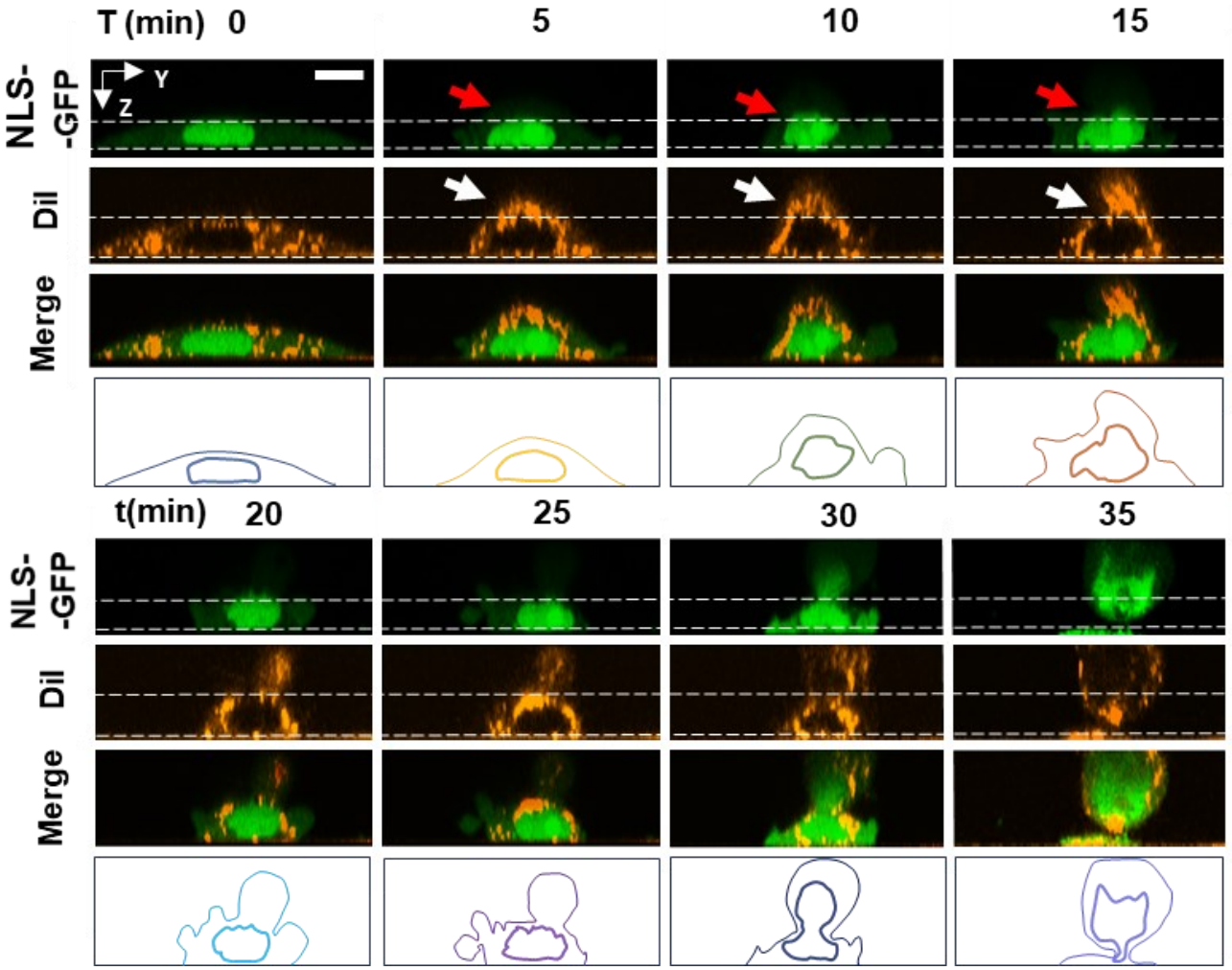


**Figure 8. Reconstructed fluorescent time-lapse images of the vertical cross-section of a live cell expressing NLS-GFP. The sample was treated with lipophilic tracer DiI showing the formation of a vertical protrusion in the cell membrane near the nucleus (white arrows) and the consequent deformation of the nucleus (red arrows) after treatment with 5µM nocodazole at time t = 0 min. For reference, vertical dashed lines indicate the initial position of the nucleus and cell membrane.**

In conclusion, we report the existence of vertically upward protrusions in spread breast cancer cells. Although the mechanism for the generation of apical cell protrusions is not clear, it is possible that NMMII-mediated contraction extrudes the apical cell membrane and associated cortex upward. The protrusions are dynamic and seem to change in orientation along the apical cell surface but are persistent over time scales of hours. We have previously suggested that the motion of boundaries away from or toward the nuclear surface can exert tensile or compressive stresses that pull or push on the nuclear surface (reviewed in [33]). The dynamic behaviors of the apical surface of the nucleus in response to the moving apical cell protrusions appear consistent with this model. How the apical protrusions might generate stress on the nucleus is not presently clear, but the Lele laboratory has previously proposed that it is due to frictional transmission of stress between the cell boundary and the nuclear surface, likely through F-actin filaments [27]. Importantly, we found that the expression of lamins in MB-231 cells greatly reduced apical cell protrusions and nuclear deformation. These results support the conclusion that cell protrusions cause local deformation of the soft cancer nucleus resulting in abnormal cancer shapes.

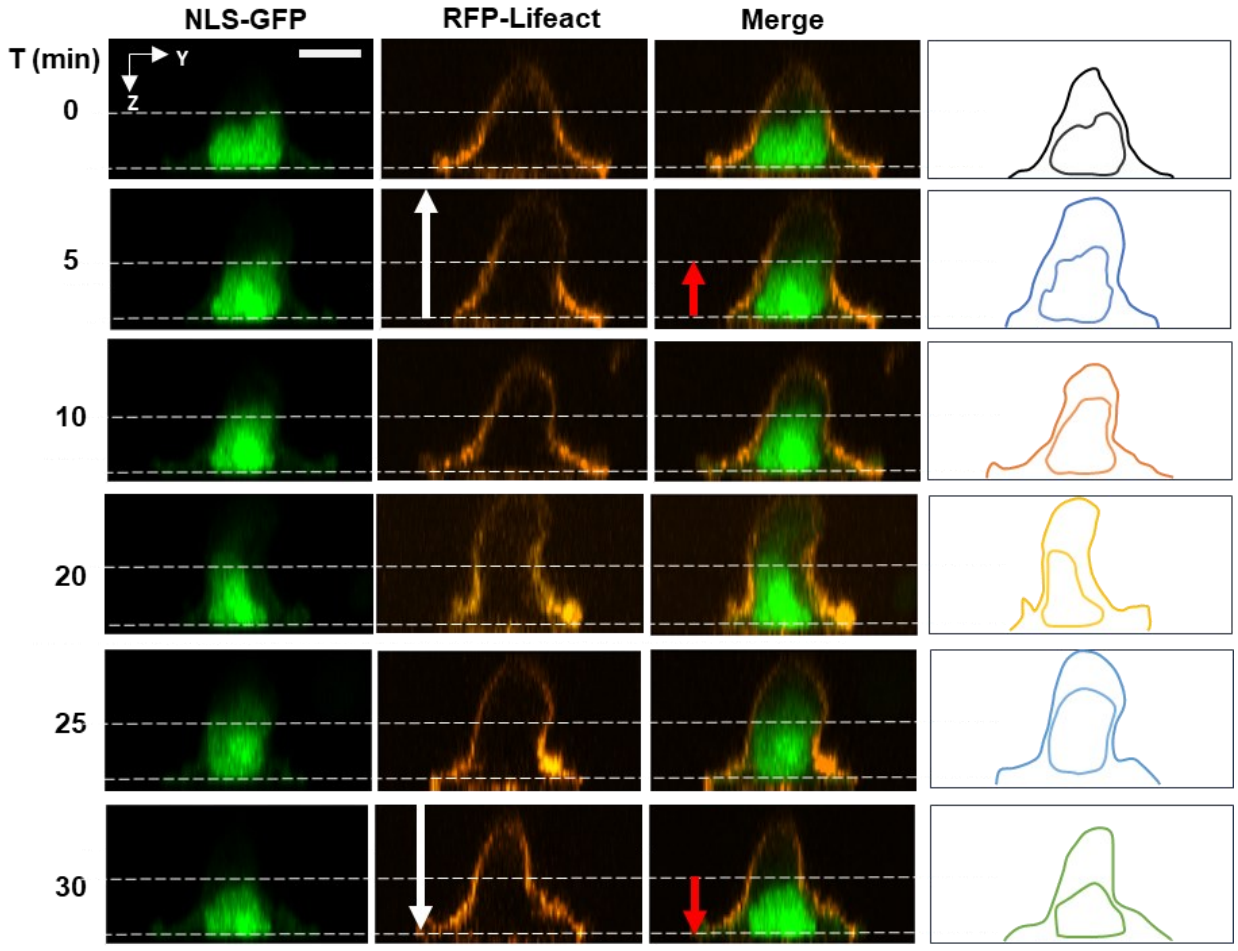


**Figure 9. Reconstructed fluorescent time-lapse images of the vertical cross-section of a living cell expressing NLS-GFP and RFP-LifeAct. Images show the formation and retraction of a vertical cell protrusion near the nucleus (white arrows) and the consequent deformation of the nucleus (red arrows) after treatment with nocodazole at t = 0 min. Vertical dashed lines indicate the initial position of the nucleus for reference.**

## 2.8 Materials and methods

### *2.8.1 Microcontact printing*

Hydrophilic polymer tissue culture dishes (Ibidi, Martinsreid, Germany) were patterned by micro-contact printing as previously described[71,72]. Briefly, a silicon wafer was etched with the surface features using standard photolithography techniques. Then, Sylgard 184 (polydimethylsiloxane elastomer kit, Dow Corning, Midland, MI) was mixed in a 10:1 ratio and cured against the silicon wafer. Rhodamine-conjugated fibronectin (Cytoskeleton, Denver, CO) was diluted to 50 μg/ml, and a 20 μl drop was adsorbed onto the stamp surface for 1 hour. Culture dishes were treated briefly with a handheld corona treatment unit (Model BD-20, Electro-Technic Products Inc., Chicago, IL) prior to contacting them with the rinsed and dried stamps. Non-printed regions of the dish were backfilled with 0.2 μg/ml PLL-g-PEG solution (Surface Solutions, Dübendorf, Switzerland) for 1 hour to prevent inadvertent protein adsorption. Substrates were stored for up to 1 week at 4°C in PBS.

### *2.8.2 Cell culture, transfection, and drug treatments*

Cells were maintained in a humidified incubator at 37°C and 5% $CO_2$. NIH 3T3 fibroblasts (ATCC CRL-1658) were cultured in Dulbecco's Modified Eagle's Medium (DMEM) with 4.5 g/L glucose (Mediatech, Manassas, VA), supplemented with 10% donor bovine serum (DBS, Gibco, Grand Island, NY) and 1% penicillin/streptomycin (Mediatech). For 3-D culture, cells were encapsulated in 3 mg/ml rat-tail collagen I gels (Ibidi) as specified by the manufacturer protocols. Briefly, 5 mg/ml collagen was thawed, diluted, and brought to physiological pH. Cells were suspended in the solution and transferred to a culture dish. Collagen fibers were allowed to polymerize at 37°C for 30 minutes before normal cell culture. Transfections were performed with Lipofectamine 3000 (ThermoFisher Scientific, Waltham, MA) in OptiMEM serum-free media

(ThermoFisher) following the manufacturer's protocols. Dendra2-H3.3-N-14 was a gift from Michael Davidson (Addgene plasmid #57725), and GFP-SRm160 was a gift from Jeffrey Nickerson. NIH 3T3 fibroblasts stably expressing GFP-Lamin A were a kind gift from Kyle Roux. Myosin inhibition was accomplished by treating cells with 25 μM Y-27632 (EMD Millipore, Billerica, MA), 50 μM Blebbistatin (EMD Millipore Billerica, MA), or 25 μM ML-7 (Sigma-Aldrich, St. Louis, MO). MDA-MB-231 cells (ATCC HTB-26) were cultured in a full growth medium consisting of Dulbecco's Modified Eagle Medium (Gibco) supplemented with 10% Donor Bovine Serum (Gibco), 1% Penicillin-Streptomycin (Gibco), 1% Non-Essential Amino Acids (Gibco), and 1% L-glutamine (Gibco). MCF-10A cells were cultured in full growth medium consisting of DMEM/F12 (Gibco) with 5% Donor Horse Serum, 20 ng/mL epidermal growth factor (Corning), 10 μg/mL insulin, 0.5 μg/mL hydrocortisone, 100 ng/mL cholera toxin, and 1% penicillin-streptomycin. Transfections of GFP-Lamin A, GFP-H1.1, or RFP-lifeact (iBidi) were performed with Lipofectamine 3000 (ThermoFisher Scientific) in OptiMEM serum-free media (ThermoFisher) following the manufacturer's suggested protocols. Transduction of Ad-NLS-GFP (a gift from Dr. Daniel Conway, originally from Vector Biosystems INC.) was performed with polybrene at a final concentration of 5 μg/ml in a normal culture medium.

MDA-MB-231 or MCF-10A cells were cultured on glass-bottom dishes (WPI) coated with 5 μg/mL fibronectin overnight at 4°C. After the cells were allowed to grow for >24 hours, the cell medium was replaced with full growth medium containing 5 μM nocodazole (Sigma-Aldrich), 50 μM blebbistatin (EMD Millipore), both 5 μM nocodazole and 50 μM blebbistatin, 100 nM cytochalasin D, or 0.3% dimethyl sulfoxide (DMSO) as a control. The cells were incubated for one hour in 37°C at 5% CO2 concentration, after which the cells were fixed by the following steps: simultaneous fixation and extraction by a solution of 0.5% glutaraldehyde, 0.8% formaldehyde,

and 0.5% Triton X-100 in PBS, fixation for a further 10 minutes by 1% formaldehyde in PBS, incubation for 10 minutes with freshly prepared 1% (w/v) sodium borohydride (NaBH4, Fisher Scientific) in PBS, and blocking with 1% bovine serum albumin (BSA) in PBS for 30 minutes. The cells were rinsed with sterile PBS in between each step, and all steps were performed at room temperature. To stain for microtubules, cells were incubated with 2 µg/mL polyclonal anti-alpha-tubulin from rabbit (Abcam) in 1% BSA for one hour, followed by incubation with an Alexa Fluor 594 goat anti-rabbit secondary antibody at 4 µg/mL for one hour, also in 1% BSA. F-actin and the nucleus were stained simultaneously by room temperature incubation of the cells with phalloidin-Alexa Fluor 488 (Life Technologies) at a dilution of 1:40 and Hoechst 33342 (Life Technologies) at 1:200 dilution in 1% BSA in PBS.

### *2.8.3 Immunostaining*

For immunostaining experiments, cells were fixed in 4% paraformaldehyde at room temperature for 10 minutes, washed with PBS, and pre-treated with permeabilization buffer (PBS containing 0.1% Triton-X and 1% bovine serum albumin) for 15 minutes. The samples were incubated with mouse anti-fibrillarin (ab4566, Abcam) or mouse anti–lamin A (ab8980, Abcam); diluted in permeabilization buffer at 4°C for 1 hour prior to secondary labeling with 488 goat-anti-mouse IgG antibody (ThermoFisher Scientific). The nucleus and F-actin were stained with Hoechst 33342 (Sigma-Aldrich, St. Louis, MO) and Alexa Fluor-488 phalloidin (ThermoFisher Scientific), respectively.

### *2.8.4 Fixed and live-cell imaging*

Imaging was performed on a Nikon A1+ laser scanning confocal microscope (Nikon, Melville, NY) with a 60x/1.4 N.A. oil immersion objective. For live-cell imaging, cells were maintained at 37°C and 5% $CO_2$ in a humidified chamber. A pinhole of 1 Airy disk with our 60 X, 1.4 N.A. objective corresponds to a typical z-directional optical section of ~ 500 nm for a 488 nm laser beam. We chose our step size in the 300-400 nm step size and performed imaging with a pinhole opening at about 1.5-1.8 Airy disks, which ensured overlapping z-stacks while sampling below the Nyquist optical section (~ 400-500 nm) to minimize photobleaching artifacts. Z-stacks for volume measurements were acquired with a 300 nm axial step size for fixed cell imaging and 400 nm axial step size for live-cell imaging; the larger axial step size for live-cell imaging was done to minimize any photobleaching artifacts.

Photoconversion experiments were performed on Dendra2-Histone H3.3 on a Nikon A1+ laser scanning confocal microscope. Cells were maintained at 37°C and 5% $CO_2$ in a humidified chamber. The photoconversion was performed by irradiating a pre-defined spot with a 405 nm laser beam at 5-10 % power, and images were collected in the green and red channels with 488 nm and 594 nm excitation lasers, respectively.

In trypsinization experiments, GFP-histone and RFP-Lifeact labeled NIH3T3 cells were plated on fibronectin-coated glass-bottom dishes overnight. Before trypsinization, cells and nuclei were imaged with a confocal microscope to construct z-stacks for 30 minutes at 5-minute intervals. The cell media was then replaced with 0.083% trypsin. Changes in cell and nuclear cross-sections were recorded every 5min using confocal z-stack imaging until cells completely detached from the dish.

MDA-MB-231 cells were seeded on glass-bottom dishes and transfected with GFP-histone H1.1 and/or RFP-Lifeact to visualize the nucleus and F-actin, respectively. In some experiments, MDA-MB-231 cells were transduced with Ad-NLS-GFP to visualize the nucleus. Invitrogen™ Fast DiI™ (D-7756) lipophilic tracer was used to visualize the cell membrane. The transfected cells were allowed to spread for >24 hours. The confocal images were collected at 1-micron step-size in the z-direction. The Z-stacks were used to reconstruct x-y or x-z cross-sections to visualize the dynamics using Nikon elements software.

### *2.8.5 Image analysis & measurement of nuclear properties*

Fiji software[73] was used for all image processing and measurements. Image stacks (for 3-D measurements, such as volume) or maximum intensity projections (for 2-D measurements, such as cross-sectional area, length, and width) were segmented with an automatic threshold algorithm using the Yen thresholding criterion. Then, measurements were performed on included voxels/pixels using Fiji's built-in tools. Nucleoli were measured in the same fashion from fluorescent images of fibrillarin.

All lamin texture segmentation and analysis were quantified from immunolabeled lamin A images. First, the images were segmented using an Otsu segmentation algorithm. A pixel area size-exclusion filter with empirically determined upper and lower limits was then applied to segmented objects to exclude small imaging artifacts. Second, the features within the nuclear lamina were detected through the application of a Laplacian of Gaussian filter. Third, the algorithm removed the contributions of the nuclear envelope from the quantification of 'texture' pixels within the lamina. The boundary of the nuclear envelope was detected using the Otsu method. A Sobel edge detection algorithm was then applied to the binary image to detect the nuclear periphery. This image was then subtracted from the texture-detected image generated in the second step of the

algorithm to obtain a new image excluding any contributions from the nuclear periphery. Finally, the number of texture pixels was summed to yield a total number of texture pixels within each individual nucleus. A schematic of this method is provided in Figure 5B.

### *2.8.6 Partial trypsinization and fixation*

Cells were partially trypsinized to round the cells in the absence of an agent depolymerizing microtubules. The cell culture medium was removed, and the cells were rinsed once with 37°C PBS. The PBS was removed, and 0.25% trypsin (Corning) at 37°C was added for 30 seconds, at which point 37°C full growth cell medium was added to the dish to inactivate the trypsin. All liquid was then removed from the dish, and the samples were fixed with 4% formaldehyde for 15 minutes. The samples were blocked in 1% BSA and stained with Hoechst 33342 and phalloidin-Alexa Fluor 488, diluted at 1:200 and 1:40, respectively, in PBS with 1% BSA.

# CHAPTER 3

# THE NUCLEUS BYPASSES OBSTACLES BY DEFORMING LIKE A DROP WITH SURFACE TENSION MEDIATED BY LAMIN A/C

## 3.1 Overview

Migrating cells must deform their stiff cell nucleus to move through pores and fibers in tissue. Lamin A/C is known to hinder cell migration by limiting nuclear deformation and passage through confining channels, but its role in nuclear deformation and passage through fibrous environments is less clear. We studied cell and nuclear migration through discrete, closely spaced, slender obstacles which mimic the mechanical properties of collagen fibers. Nuclei bypassed slender obstacles while preserving their overall morphology by deforming around them with deep local invaginations of little resisting force. The obstacles did not impede the nuclear trajectory or cause a rupture of the nuclear envelope. Nuclei likewise deformed around single collagen fibers in cells migrating in 3-D collagen gels. In contrast to its limiting role in nuclear passage through confining channels, lamin A/C facilitated nuclear deformation and passage through fibrous environments; nuclei in lamin-null (*Lmna*$^{-/-}$) cells lost their overall morphology and became entangled on the obstacles. Analogous to surface tension-mediated deformation of a liquid drop, lamin A/C imparts a surface tension on the nucleus that allows nuclear invaginations with little mechanical resistance, preventing nuclear entanglement and allowing nuclear passage through fibrous environments.

## 3.2 Introduction

Cells migrate through interstitial spaces of fibrous tissue during key physiological processes like wound healing and cancer cell invasion. During this process, the cells have to deform the nucleus to fit through interstitial gaps that are typically smaller than the nuclear size [2,14,74]. Deformability of the nucleus has been shown to limit the passage of cells through micropores in the 3-D fibrous extracellular matrix [2,14,75,76]. As such, there is much interest in understanding how the cell can deform the nucleus to fit through interstitial gaps despite its high mechanical stiffness [33,77-79].

Nuclear lamins are known to be the key contributors to the mechanical stiffness of the nucleus [3,7,13,20,80-84]. Lamin A/C, and not lamin B1, limits the passage of the nucleus through confining pores in 3D collagen gels or microfabricated microchannels [85,86]. Furthermore, the depletion of lamin A/C but not lamin B1 significantly softens the nucleus [8]. These studies collectively suggest that the mechanical stiffness conferred onto the nucleus by lamin A/C impedes nuclear deformation and hence cell passage through narrow micropores or channels.

While the role of lamin A/C in limiting nuclear deformation and passage through confining channels has been studied extensively in pores and microchannels with a smooth contiguous surface, cells such as fibroblasts and cancer cells encounter slender extracellular matrix fibers as they migrate through interstitial tissue [87]. Here we examined the role of lamin A/C in cell migration through discrete, closely spaced obstacles designed such that their stiffness was similar to the stiffness of single collagen fibers. Unlike in micropores, where the presence of lamin A/C impedes translocation of nuclei, our results show a facilitating role for lamin A/C in the nuclear passage in between slender obstacles. Specifically, wild-type nuclei containing lamin A/C can bypass the slender obstacles while preserving their overall oval shape despite deep local indentations caused

by the obstacles. Nuclei lacking lamin A/C, in contrast, become extremely deformed and entangled around obstacles, thus impeding nuclear motion. Our results support a model in which the nucleus deforms like a drop with surface tension conferred by lamin A/C.

### 3.3 Results

We cultured fibroblasts on an array of fibronectin-coated, flexible, vertical PDMS micropost barriers, which were continuous with the underlying PDMS surface (schematic in Figure 10A). The diameter of the microposts (~1 micron, Figure 10B) and Young's modulus were chosen such that their flexural rigidity was similar to that of single collagen fiber bundles (see methods). The microposts were arranged in circular patterns (Figure 10B) such that the distance between adjacent pairs of microposts in the pattern was smaller than typical nuclear diameters with a height similar to typical nuclear heights (~5 microns) in cultured cells (Figure 10B and Figure 11). Cells cultured on these fibronectin-coated substrates adhered to the bottom surface and internalized the microposts such that the microposts protruded above the apical cell surface (SEM image in Figure 10C, yellow arrowheads).

We performed time-lapse confocal fluorescence imaging of fibroblasts stably expressing GFP-BAF (Barrier-to-Auto-Integration Factor) on the micropost substrates. To calculate the force due to cellular or nuclear contact, the microposts were coated with rhodamine-fibronectin (r-FN), and their deflection was tracked by imaging their top and bottom positions. GFP-BAF was imaged as a marker of the nuclear envelope and of envelope rupture [64,88]. Despite the fact that the nucleus was wider than the gap in between the micropost obstacles, the nucleus was able to move unimpeded past the obstacles because contact with each new obstacle created a transient deep, local invagination in the nuclear surface (Figure 10D). These invaginations continually formed and disappeared as the nucleus encountered microposts during its forward motion.

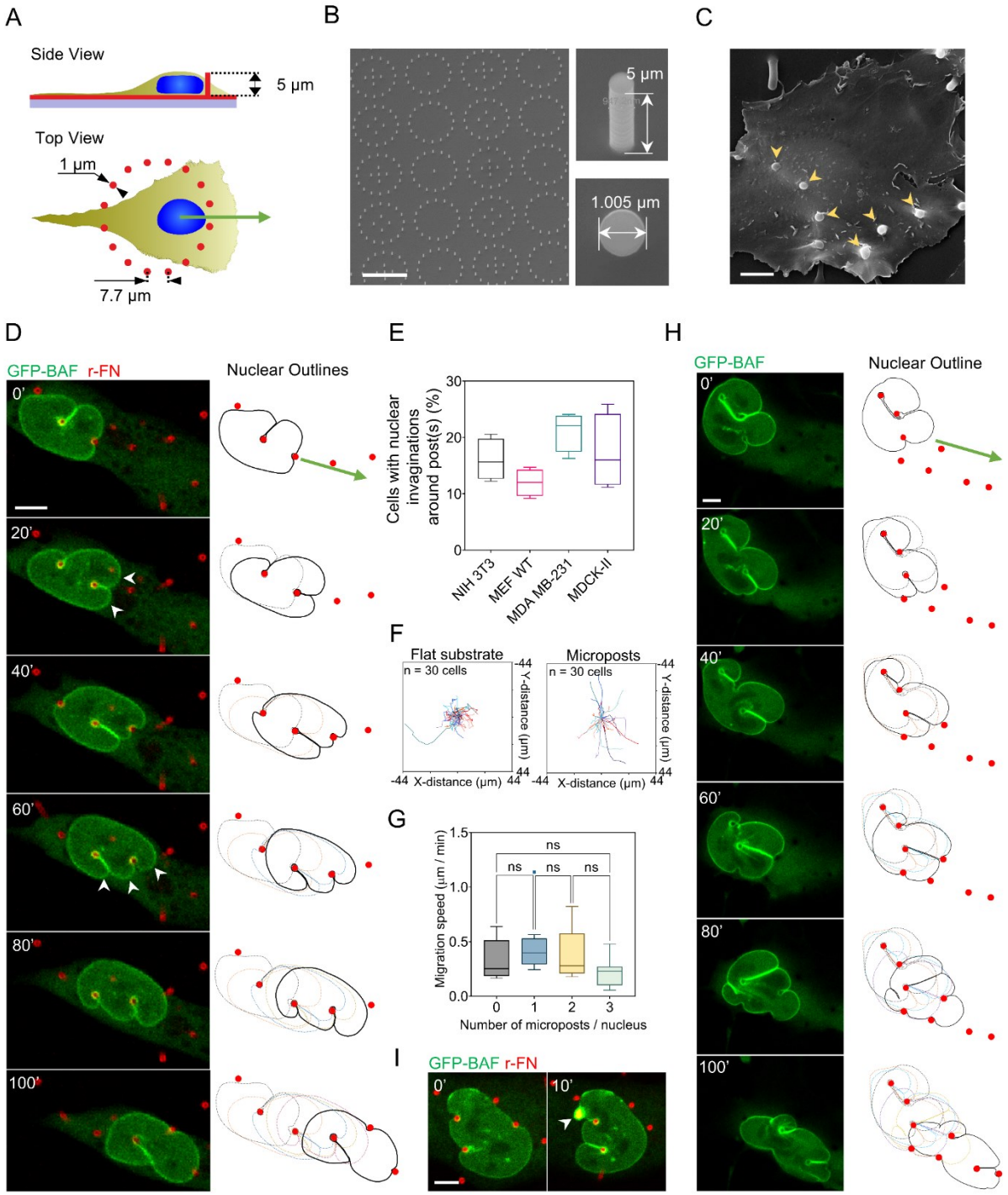


**Figure 10. Nuclear invaginations around microposts permit unhindered forward motion of the nucleus. (A) Schematic illustrates micropost geometry relative to cell shape. (B) SEM image shows the circular pattern of fabricated microposts (left, scale bar is 20 μm) and**

**micropost geometry (right). (C) SEM of an MDCK-II cell on microposts, yellow arrowheads indicate internalized microposts (Scale bar is 5 µm). (D) Time-lapse confocal images of an NIH 3T3 fibroblast stably expressing GFP-BAF deforming around 5 µm tall rhodamine-fibronectin coated PDMS microposts (red) and forming transient deep, local invaginations in the nuclear surface (Scale bar is 5 µm). Nuclear outlines relative to the position of microposts are shown on the right. (E) Plot shows the percentage of cells with nuclei that formed deep invaginations around the microposts in different cell types, including fibroblasts (NIH 3T3 and MEF), epithelial cells (MDCK-II), and breast cancer cells (MDA-MB-231); n = 50 cells per condition from 3 independent experiments. (F) Nuclear trajectories of NIH 3T3 fibroblasts migrating on a flat substrate (left) and microposts (right); n = 30 cells imaged for 2 hours for each condition from 3 independent experiments. (G) Bar graph shows the mean nuclear speed in cells migrating against a varying number of microposts. Error bars represent SEM. (ns p>0.05; Brown-Forsythe and Welch ANOVA test). (H) Time-lapse confocal images of an NIH 3T3 fibroblast stably expressing GFP-BAF deforming around 11 µm tall Si microposts (red), forming deep invaginations in the x-y plane, separated by lobes of nearly constant curvature (Scale bar is 5 µm). Nuclear outlines relative to the position of microposts are shown on the right. (I) Nuclear envelope rupture in fibroblasts caused by micropost indentation. White arrowhead points to the local enrichment of GFP-BAF indicative of rupture (Scale bar is 5 µm).**

Notably, despite the continual formation and disappearance of the deep invaginations from different directions, the overall oval nuclear shape was preserved (outlined in Figure 10D). In many cases, the moving, deforming nuclei slid over the top of the microposts (Figure 12, white arrowheads) without collapsing them (Figure 12) (which gave the appearance that the microposts

were passing completely through the nucleus in the lower x-y planes). Even in these cases, the overall oval shape of the nucleus was maintained. Notably, the lobes on either side of the invaginations had near-constant curvature (Figure 10D, white arrowheads). This suggests that the lobes are pressurized with the tension in the curved lamina balancing the pressure difference across the nuclear envelope (by Law of Laplace).

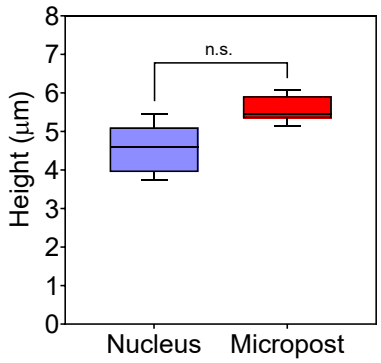


**Figure 11. Comparison of nuclear height measured in nuclei deformed around individual microposts with the height of microposts measured from reconstructed z-stacks; n ≥ 20 nuclei and n ≥ 20 microposts from at least three independent experiments. (ns p > 0.05, Student's *t*-test).**

Because nuclear deformation is a dynamic phenomenon, only 20-30% of cells that were fixed at a given instant were observed to contain nuclei with deep local invaginations which surrounded the microposts; such invaginations were observed consistently across mesenchymal, epithelial, and cancer cell types (Figure 10E). A comparison of cellular trajectories on flat PDMS substrates compared to micropost substrates confirmed that cellular migration was unimpeded on micropost substrates (Figure 10F). Nuclear speeds across microposts were 0.34±0.03 $\mu m.min^{-1}$ and were insensitive to the number of microposts (Figure 10G). Speed insensitivity to the number

of microposts provides a further indication that invaginations around microposts permit unhindered forward motion of the nucleus.

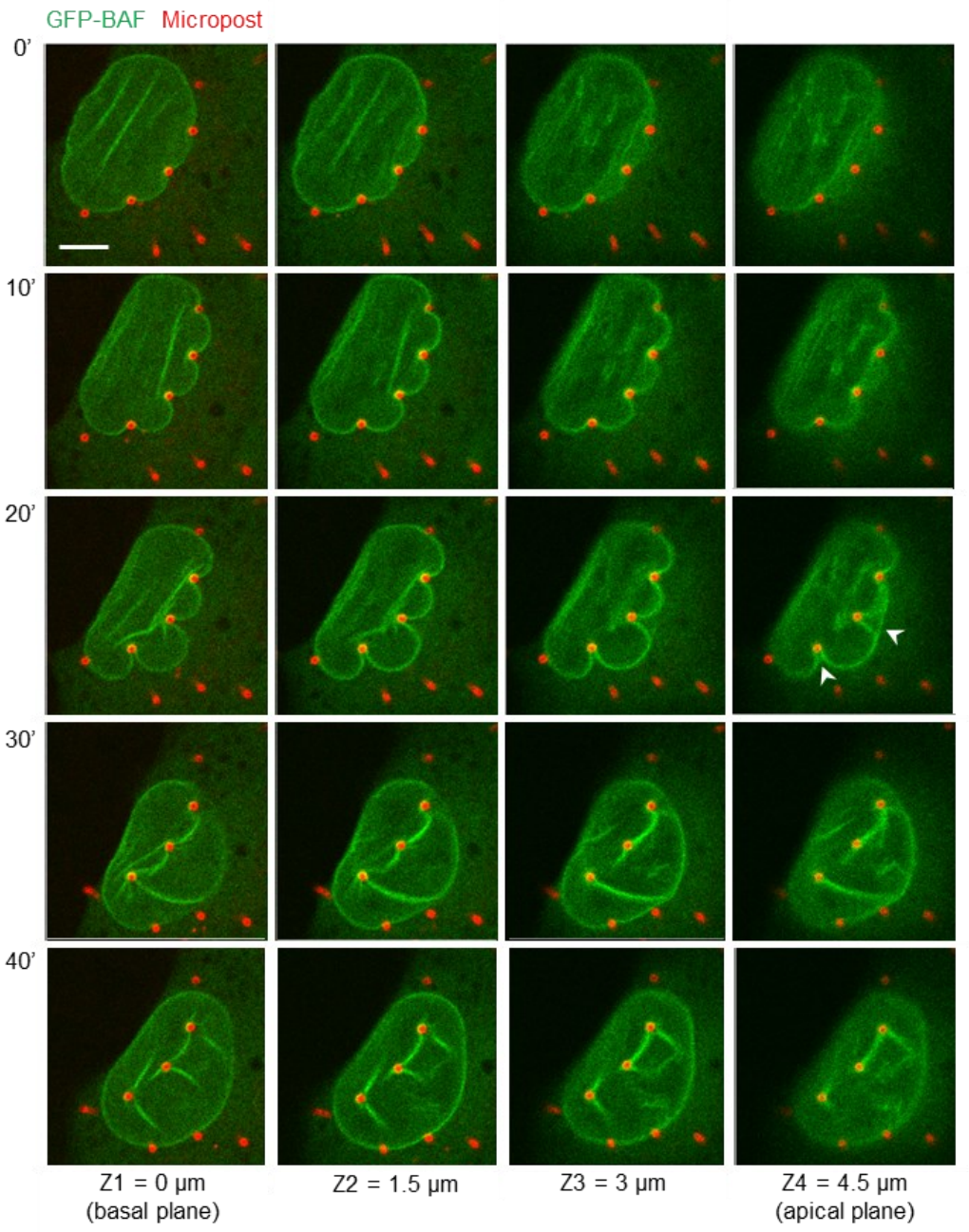


**Figure 12. Time-lapse confocal images of an NIH 3T3 fibroblast stably expressing GFP-BAF deforming around 5 µm tall rhodamine-fibronectin stained PDMS microposts (red) sliding**

**over the top of the microposts (white arrowheads), without collapsing the vertical microposts, (Scale bar is 5 µm).**

To determine whether nuclear motion through the micropost array required deflection of microposts and/or moving over the top of the microposts, we repeated these experiments with silicon microposts that were taller but more rigid (11 microns in height) (Figure 10H). The nucleus similarly formed deep invaginations in the x-y plane, separated by lobes of nearly constant curvature; these invaginations allowed the nucleus to move unimpeded in between the silicon microposts. Despite the consistent formation of deep nuclear invaginations on the 5-micron tall PDMS microposts and 11-micron tall silicon microposts, rupture of the nuclear envelope, as indicated by local BAF accumulation, was rare (~5% of cases, Figure 10I). In contrast, we have previously shown that rapid elastic deformations of the nucleus, even if small, typically cause envelope rupture [89], and rupture is more frequent when the nucleus deforms during migration through confining channels [14,65]. In the few instances that rupture did occur, the rupture did not typically occur along the invagination (Figure 13). These results with PDMS as well as silicon microposts show that the principal behaviors observed on the microposts (deep nuclear invaginations and unimpeded motion of the nucleus) did not require microposts to be elastically compliant.

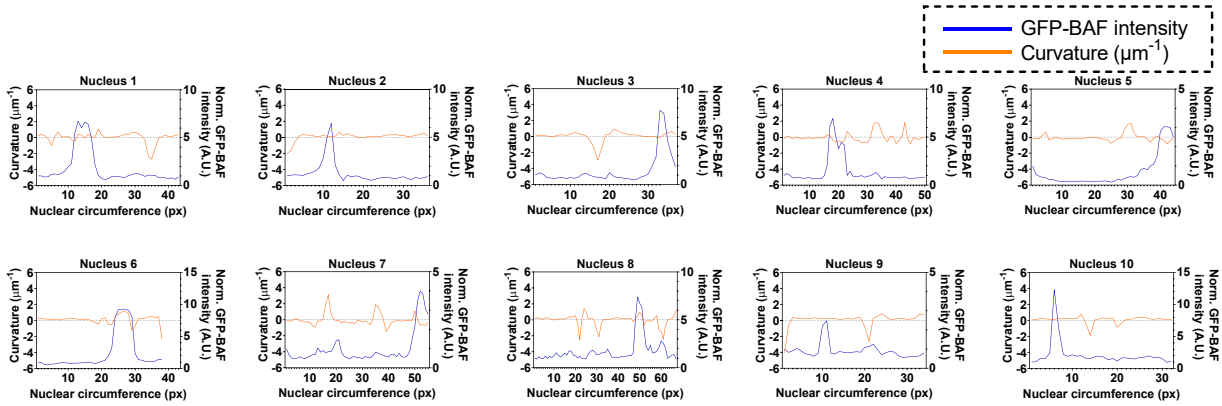


**Figure 13. Plots of nuclear envelope curvature (orange curve) and GFP-BAF intensity (blue curve) along the circumference of nuclei (n = 10 cells) that deformed and underwent nuclear envelope rupture around microposts.**

All microposts that were internalized by cells were surrounded by the plasma membrane throughout their vertical length (Figure 14A). Importantly, the plasma membrane continued to surround microposts even when these microposts were present inside nuclear invaginations. Furthermore, internalized microposts were surrounded by F-actin inside nuclear invaginations (Figure 14B). The microposts did not appear to affect the assembly of F-actin networks into basal stress fibers which formed around them (Figure 14C). Both outer and inner nuclear membranes surrounded the microposts (Figure 14D). The nuclear lamina, visualized by GFP-lamin A expression, behaved similarly to the GFP-BAF labeled nuclear surface around the microposts (Figure 14E), with deep invaginations around the microposts (Figure 14E, yellow arrowheads). These results show that the microposts are not exposed to cellular or nuclear contents and that the invaginations are able to form even in the stiff nuclear lamina.

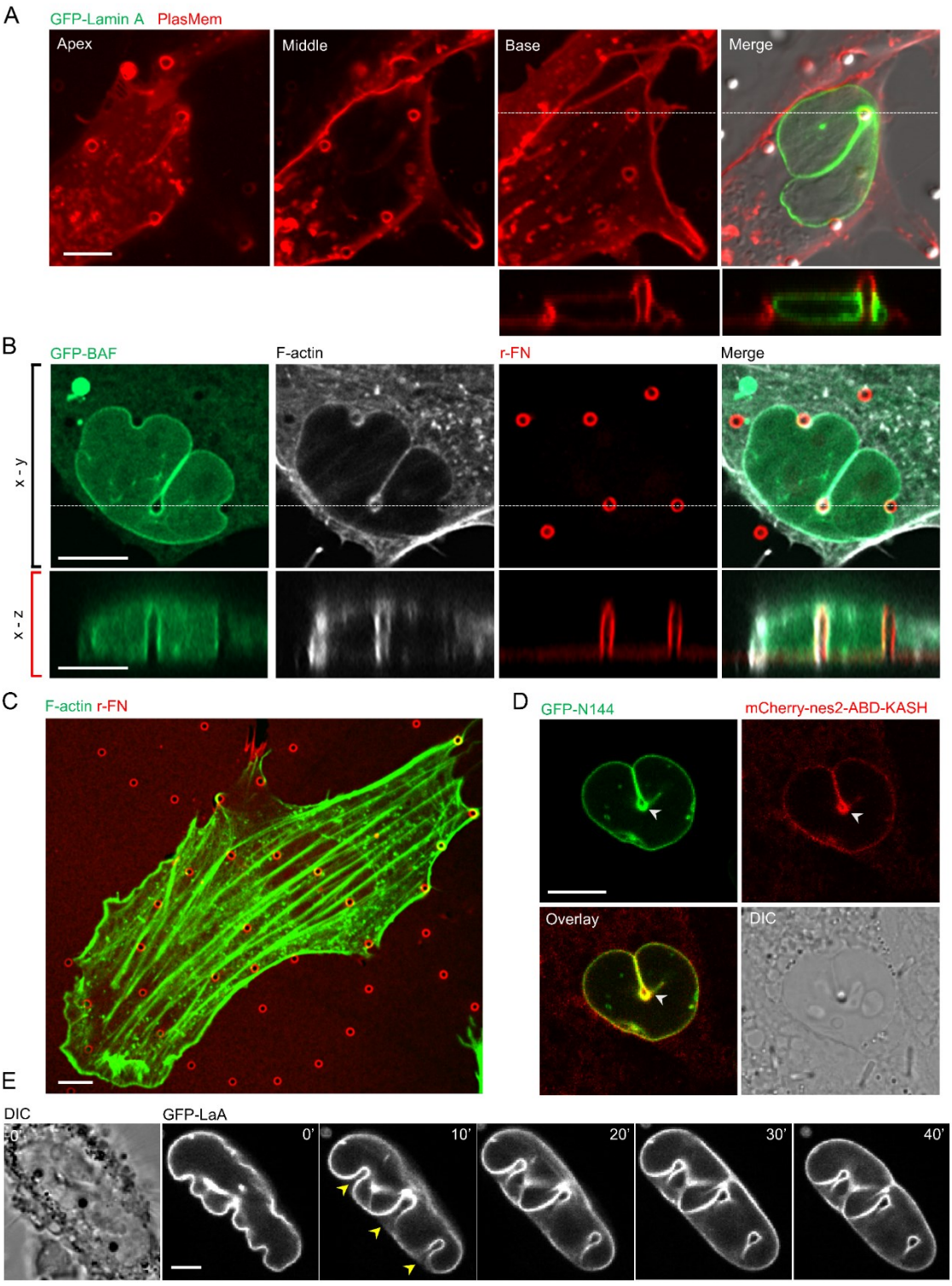


**Figure 14. Microposts in nuclear invaginations are not exposed to cellular or nuclear contents. (A) Confocal images of a fibroblast cultured on microposts, with plasma membrane**

**labeled with PlasMem bright red, and expressing GFP-lamin A (green). The apical, middle and basal planes are shown along with the corresponding x-z view situated along the white-dashed line (Scale bar is 5 µm). (B) Confocal images of F-actin stained with phalloidin (white) and GFP-BAF (green) expressing fibroblast with nucleus deformed around the microposts coated with Rhodamine-fibronectin (red); corresponding x-z views are also shown. (Scale bar is 5 µm). (C) Confocal image of F-actin stress fibers (green) in the basal plane of a fibroblast cultured on rhodamine-fibronectin-coated microposts (red) (Scale bar is 5 µm). (D) Images of an MCF-10A cell stably expressing GFP-N144 (green) and mCherry-nes2-KASH (red) cultured on microposts. White arrowheads point to the ring of the inner and outer nuclear membrane proteins around a single micropost present in a nuclear invagination (Scale bar is 5 µm). (E) Time-lapse image sequence showing the development of nuclear invaginations (yellow arrowheads) in a GFP-lamin A expressing fibroblast. (Scale bar is 5 µm).**

As the nucleus is generally considered to be mechanically stiff [3,8,13,21,90], deep invaginations would be expected to result in a large opposing force that would impede nuclear motion. We, therefore, set out to calculate the magnitude of forces that cause nuclear invagination by measuring the deflection of the microposts with known mechanical stiffness. To quantify micropost deflection in the direction normal to the invaginating nuclear surface, we measured the deflection vector at the top of the micropost and how it was modified following contact with the nuclear surface (Figure 15A, brown and red arrows). The differential deflection vector was calculated by vectorial subtraction of the deflection vector at a given time point from the deflection vector before nuclear contact (blue arrows in Figure 15B). The component of the differential deflection vector along the direction of the invagination yielded the force exerted by the micropost on the nucleus (Figure

15A). The average force was ~2 nN for an indentation depth of 4-6 microns (Figure 15A-3E), which is significantly smaller than the corresponding forces measured by AFM (10-15 nN [91-93]). Furthermore, the force appeared to correlate with the invagination depth only up to an initial penetration of ~3 microns, after which it became insensitive to the invagination depth (Figure 15E).

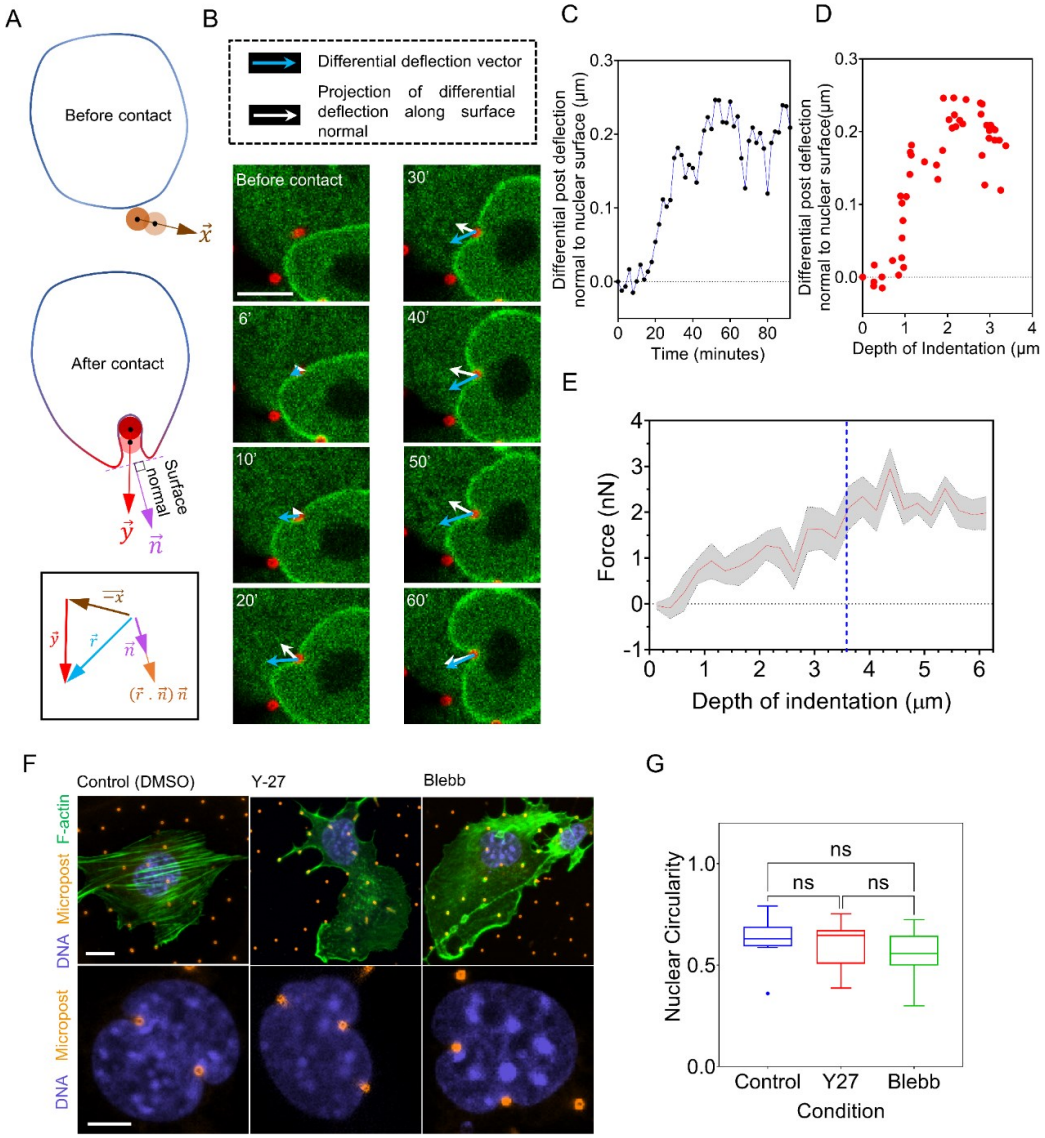


**Figure 15. Measurement of forces associated with nuclear invagination and myosin-insensitivity of nuclear invaginations. (A) Schematic shows the calculation of a differential**

**deflection vector ($\vec{r}$) as the vectorial change in deflection of the micropost after nuclear contact, and subsequent projection onto the nuclear surface normal. (B) A representative example of the calculated differential deflection vector (blue) and the corresponding normal component (white arrows) in a nuclear invagination (Scale bar is 5 µm). (C) Plot of the magnitude of the component of the differential vector along the surface normal against time for the example in (B). Time t = 0 refers to the time-point before the first nucleus-micropost contact. (D) Plot of the differential vector along the surface normal corresponding to 3C against the depth of indentation. (E) Plot shows the magnitude of force for mean values pooled from n = 10 cells from at least three independent experiments. Grey area represents SEM. The vertical dashed line (blue) indicates a plateau in the force. (F) Images show representative examples of fibroblasts on microposts (orange) treated with DMSO (control), Y-27632 (25 µM), and Blebbistatin (50 µM) for 12 hours before fixation, followed by staining with Hoechst H33342 (blue, DNA) and Phalloidin (green, F-actin) (Scale is 10 µm in the top panel; Scale bar is 5 µm in bottom panel). (G) Plot of nuclear circularity of control and treated cells in (F), (ns p>0.05; Brown-Forsythe and Welch ANOVA test).**

The low magnitude of resisting force to invagination may explain why the invaginations do not hinder the forward motion of the nucleus. Consistent with the low force, the nuclei were able to deform around the posts like the control even upon treatment with Y-27632, a Rho kinase inhibitor, or Blebbistatin, a myosin inhibitor, both of which inhibit actomyosin contractility (Figure 15F and 15G). Moreover, the plateau in the force-invagination length curve (Figure 15E, dashed blue line) is more consistent with the behavior of an invaginating liquid drop with a surface tension rather than an invaginating elastic solid. The resisting force of a solid is expected to increase with increasing indentation depth, whereas the resisting force of a liquid with constant surface tension

is expected to plateau once the invagination is fully developed to the point where two sides of the invagination become parallel. We tested this intuition by indenting the nucleus with the ~ 1-micron tip of a Tungsten microneedle. Rapid deformation of the nucleus in ~15 s with the microneedle produced shapes that resembled kidney-bean-like morphologies (Figure 16A, top panel). This response is in contrast to the slower deformations around the microposts over tens of minutes during migration, which produced invaginations closely wrapped around the nucleus (Figure 16B). These differences in shape can be explained by a mechanical resistance to a strain of the nuclear interior on the shorter time scale but an overall nuclear pressure balanced by surface tension on the longer time scale. This explanation is consistent with the notion that any mechanical energy stored in the strained nuclear interior dissipates on the time scale of migration such that only the surface tension and the resistance of the nucleus to volume change (i.e., nuclear pressure) govern nuclear deformation in response to external forces on this time scale [33,94].

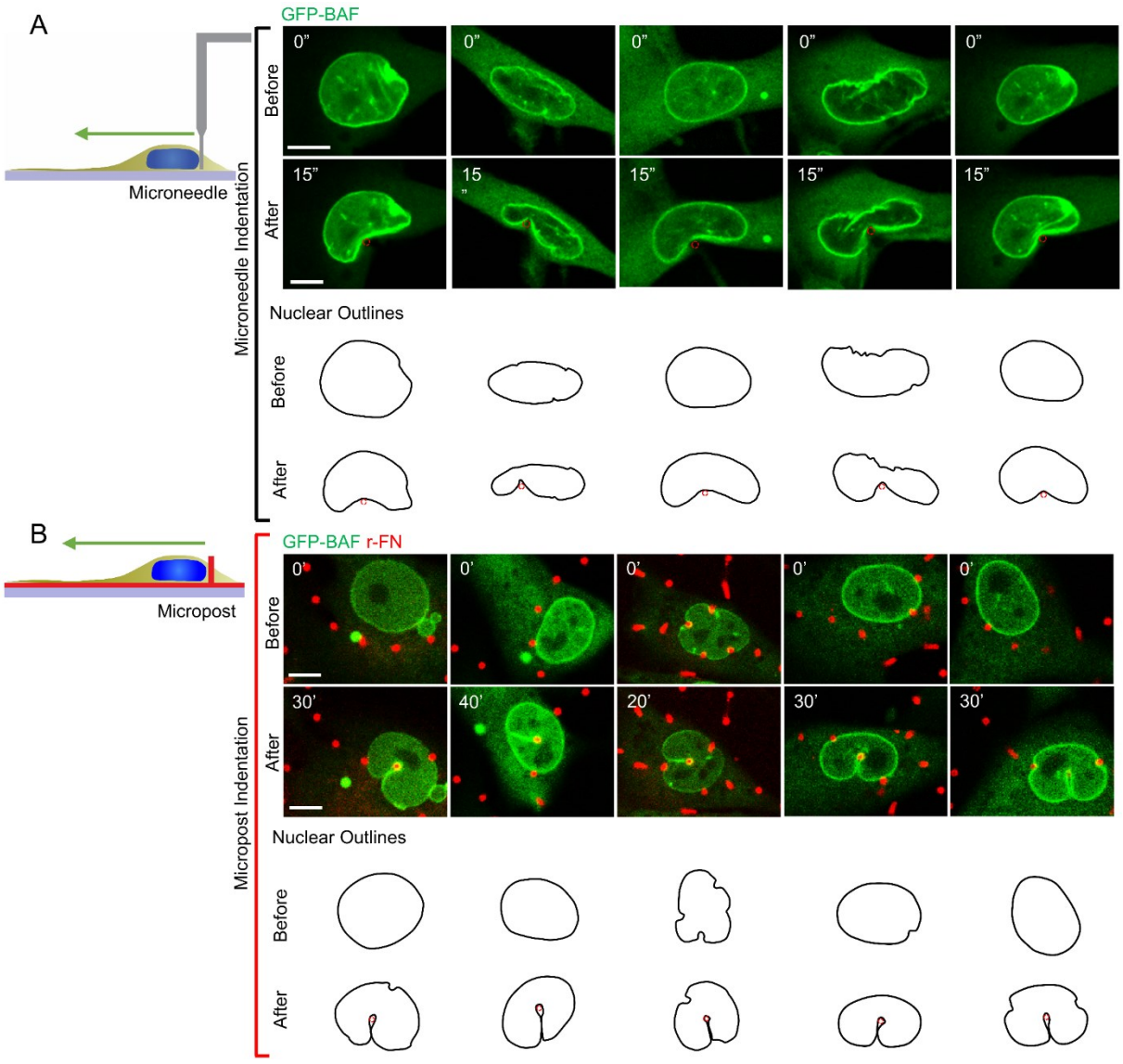


**Figure 16. Comparison of nuclear deformation at slow and fast time scales. (A) Images of nuclei of GFP-BAF expressing fibroblasts deformed with a 1-micron diameter Tungsten microneedle at fast time scales (~15 seconds). (B) shows nuclei deformed around microposts in the same cell type over tens of minutes. The nuclear outlines are rotated to highlight the qualitative difference between the nuclear deformation at short (seconds) and long (minutes) time scales (Scale bar is 5 µm).**

We explored how these findings relate to three-dimensional cell migration through fibrous environments by examining nuclear deformation in 3-D collagen gels. In these experiments, we observed many instances where a single collagen fiber (~0.4 μm in diameter) caused an invagination in the cell nucleus (Figure 17A), much like the microposts (Figure 17B). Invaginations were present throughout the thickness of the nucleus (compare Figure 17C and 17D). These invaginations allowed the nucleus to bypass the fiber without getting entangled during cell migration (compare Figure 17E and 17F). Much like nuclear bypassing of microposts, these results show that local invaginations facilitate nuclear motion around slender obstacles in a 3-D fibrous microenvironment.

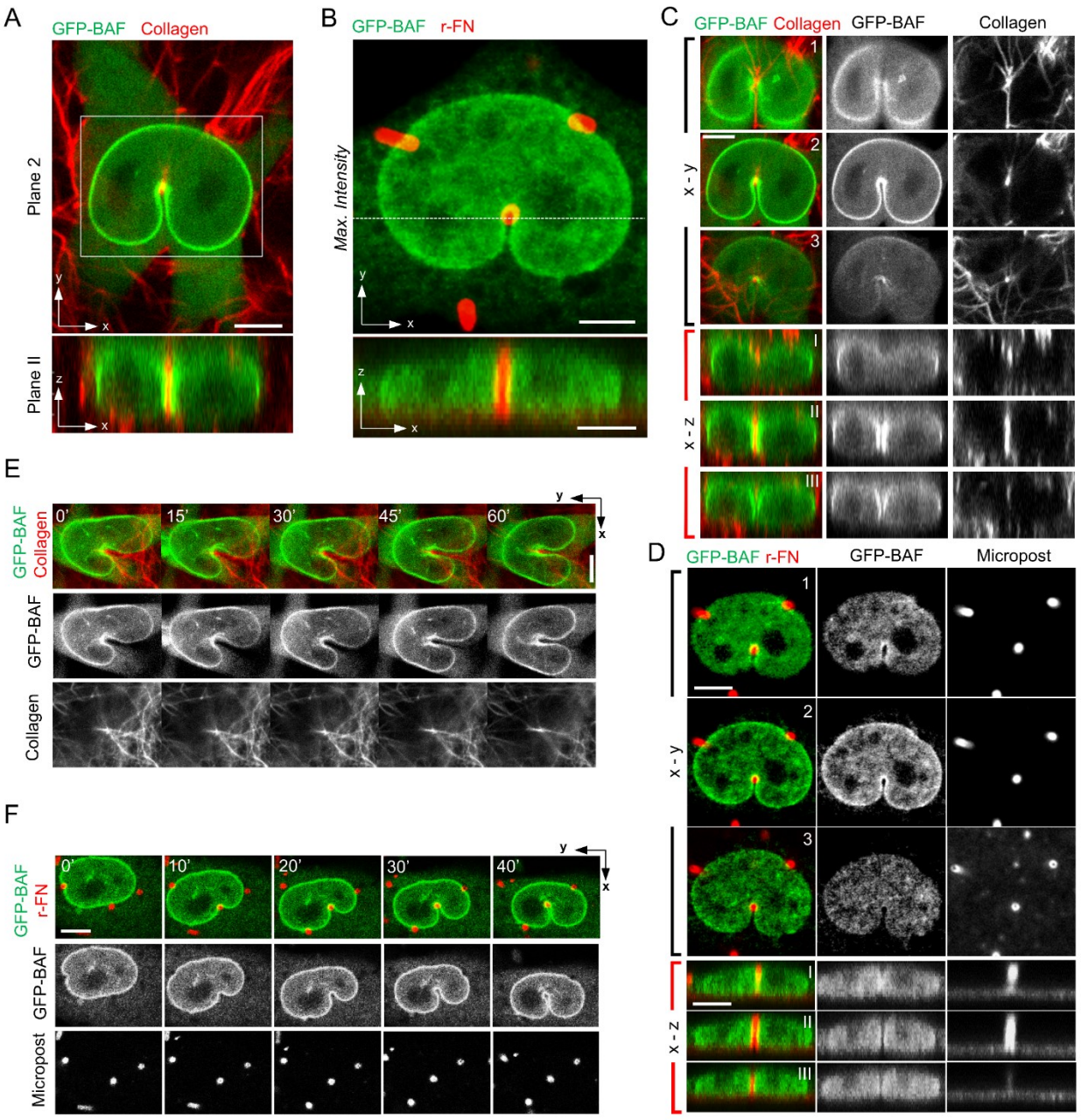


**Figure 17. Nuclear invaginations around single collagen fibers during 3D migration. (A) Representative images of a fibroblast (expressing GFP-BAF, green) cultured in 0.5 mg/mL 3-D collagen gel (collagen fibers labeled with NHS ester dye in red). Top (X-Y Plane 2 of example in 5C) and bottom (X-Z Plane II of example in 5C) panels show the horizontal and vertical cross-section views (Scale bar is 5 µm). (B) (Top) Maximum intensity projection of**

**a fibroblast stably expressing GFP-BAF (green) deformed against microposts (red). (Bottom) X-Z reconstruction of confocal z-stacks shows nuclear envelope (green) and microposts (red) in the axial direction (Scale bar is 10 μm). (C) Different cross-sectional views for the nuclear region within the white box in figure 17A are shown in the middle column. X-Y Planes 1-3 show the horizontal cross-section planes focused on the top, middle, and bottom of the nucleus, respectively. X-Z Planes I-III are the vertical cross-section planes located behind, at, and in front of the vertical collagen fiber (Scale bar is 5 μm). (D) Different cross-sectional views of the nucleus are shown in figure 17B. X-Y planes 1-3 correspond to the focal plane of the top, middle, and bottom of the nucleus, respectively (Scale bar is 5 μm). X-Z Planes I-III are the vertical cross-section planes located behind, at, and in front of the vertical micropost (Scale bar is 5 μm). (E) and (F) show time-lapse images of GFP-BAF expressing nuclei deforming around a vertical collagen fiber (E) (Scale bar is 5 μm) or a micropost (F) during cell migration (Scale bar is 10 μm).**

As our results suggest that the surface tension and nuclear pressure govern nuclear deformation during encounters with micropost obstacles, we explored the extent to which the nuclear lamina confers these properties on the nucleus. It is possible that the intermediate filament family protein lamin A/C is responsible for surface tension because lamin A/C is a key determinant of the mechanical properties of the nucleus. [3,7,13,20,80-84] We examined the shapes of nuclei as they deformed around microposts in migrating mouse embryonic fibroblasts lacking the *Lmna* gene that encodes for lamin A/C (*Lmna*$^{-/-}$ mouse MEFs). In contrast to nuclei in wild type (WT) MEFs, which retained their overall elliptical shape in the x-y plane despite many invaginations wrapped around microposts (Figure 18A), nuclei in *Lmna*$^{-/-}$ MEFs lost their overall oval shape while deforming around microposts. Instead, the nuclei had wispy finger-like extensions between

microposts that did not wrap around the microposts (marked with white arrows in Figure 18A, see also Figure 19). These behaviors are consistent with diminished surface tension and a corresponding lack of nuclear pressure in *Lmna*$^{-/-}$ MEFs. The extreme nuclear deformation was reflected in a sharply lower nuclear circularity in *Lmna*$^{-/-}$ cells compared to WT cells cultured on microposts (Figure 18B). Live cell imaging revealed that the *Lmna*$^{-/-}$ nuclei became entangled around the microposts in a way that prevented their movement past them (Figure 18C, second panel). This was in stark contrast to WT nuclei which bypassed the microposts by forming deep local invaginations as before while preserving overall nuclear shape (Figure 18C, first panel). The behavior of the WT nucleus could be rescued in *Lmna*$^{-/-}$ cells by expressing WT GFP-lamin A/C in them (Figure 18C, third panel). Together, the results suggest that lamin A/C supports a surface tension that balances the nuclear pressure. This surface tension permits the formation of local invaginations without entangling the nucleus, allowing forward nuclear motion while preserving its overall shape.

*Lmna*$^{-/-}$ cells expressing GFP – Lamin A S22A/S392A, a non-phosphorylatable lamin A/C mutant, could initially deform with deep invaginations while preserving the oval nuclear shape around the microposts, similar to the wild-type and unlike the *Lmna*$^{-/-}$ nuclei (we confirmed that the mutant lamin A localizes primarily to the lamina consistent with previous reports [95]). This suggests that unlike *Lmna*$^{-/-}$ nuclei, Lamin A S22A/S392A expressing nuclei can build up a nuclear pressure and support a surface tension. However, the nuclei were ultimately unable to bypass the microposts, getting entangled in them, like the *Lmna*$^{-/-}$ cells (Figure 18C, last panel). These entanglements tended to coincide with frequent rupture events (Figure 18C, white arrowhead). Rupture coincided with an apparent transient loss of pressure, as evident from regions of near-zero and negative curvatures (yellow arrows in Figure 18C) and caused a loss of the overall oval nuclear

shape. These results suggest that nuclear entanglements can also be caused by transient loss of pressure and corresponding loss of surface tension caused by nuclear envelope ruptures.

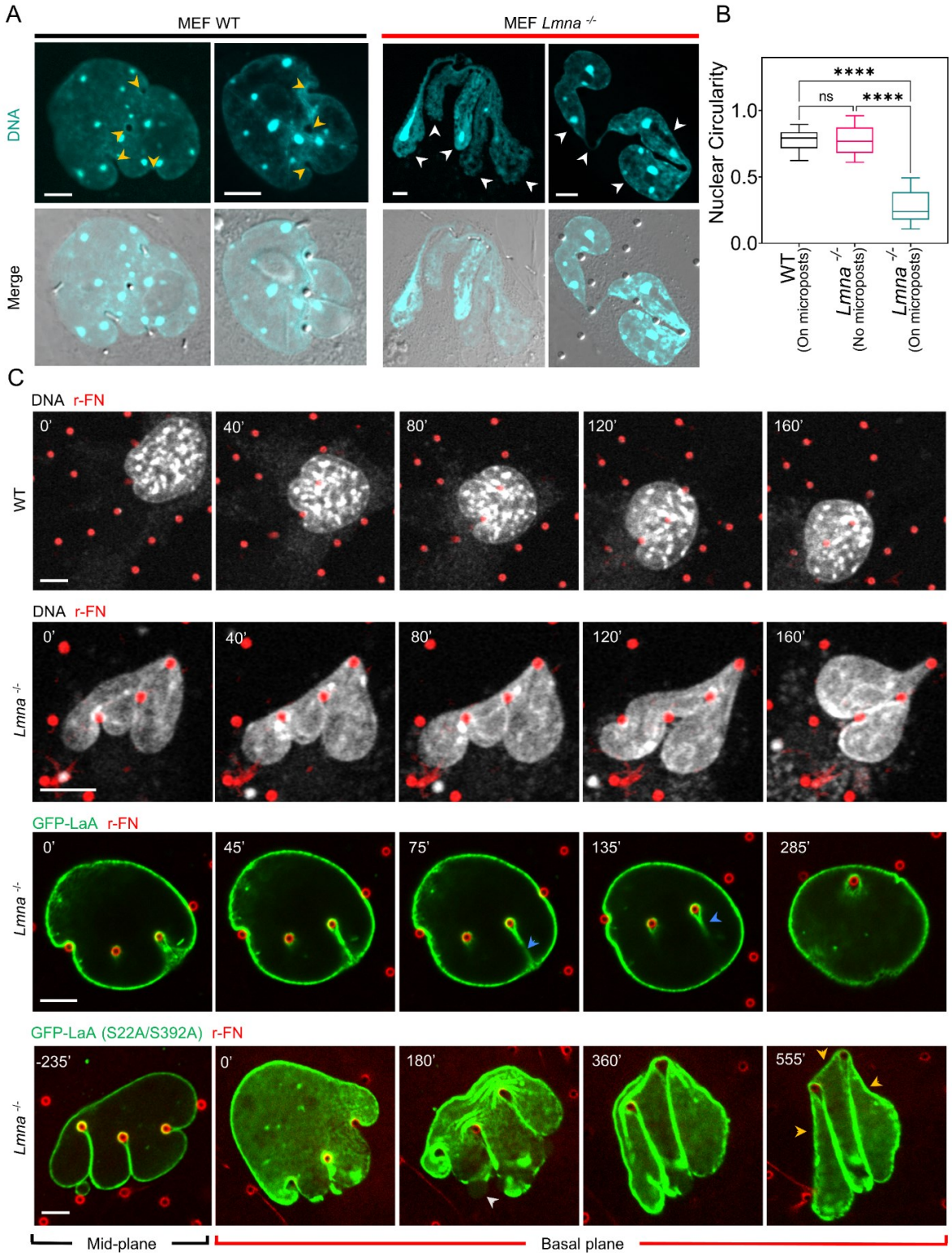


**Figure 18. Lamin A/C preserves overall nuclear shape during nuclear invagination around**

**microposts. (A) Images of fixed Hoechst 33342 stained MEF WT and MEF *Lmna*$^{-/-}$ nuclei deformed around microposts. Yellow arrowheads point to the micropost locations, and white arrowheads indicate wispy finger-like nuclear extensions around the microposts (Scale bar is 5 µm). (B) Comparison of circularity of MEF WT nuclei and MEF *Lmna*$^{-/-}$ nuclei, deformed around microposts, or on surfaces devoid of microposts; (n = 31 nuclei for WT, n = 30 nuclei *Lmna*$^{-/-}$ on flat surface, and n = 32 nuclei for *Lmna*$^{-/-}$ on microposts from at least three experiments per condition; ns: $p > 0.05$ and ****: $p < 0.0001$; Kruskal-Wallis test). (C) Top two panels: time-lapse sequences of a MEF WT nucleus and an MEF *Lmna*$^{-/-}$ nucleus stained with NucSpot Live 650 (a live-nuclear imaging dye) (white) during nuclear invagination around rhodamine-labeled microposts (red). Scale bar is 5 µm. Third panel: time-lapse sequence of an MEF *Lmna*$^{-/-}$ nucleus expressing WT GFP-Lamin A (green) deforming against a rhodamine-fibronectin labeled micropost (red). Scale bar is 5 µm. Bottom panel: time-lapse sequence of an MEF *Lmna*$^{-/-}$ nucleus expressing GFP-Lamin A (S22A/S392A mutant) (green) deforming against a rhodamine-fibronectin labeled micropost (red). White arrowhead points to a site of blebbing followed by nuclear envelope rupture, and yellow arrows point to regions of near-zero and negative curvatures (Scale bar is 5 µm).**

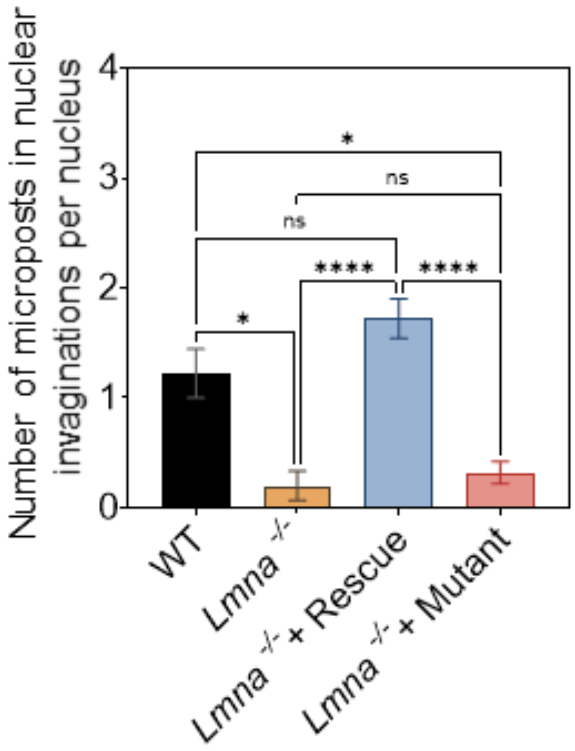


**Figure 19. Box plot shows the number of microposts in nuclear invaginations by the nucleus per cell in MEF WT (n = 12 cells), MEF *Lmna* $^{-/-}$ (n = 18 cells), MEF *Lmna* $^{-/-}$ + GFP-Lamin A (rescue) (n = 22 cells) and MEF *Lmna* $^{-/-}$ + GFP-Lamin A (S22A/S392A) mutant (n = 25 cells) from three experiments for each condition. (* p < 0.05; Mann-Whitney test).**

### 3.4 Conclusion

We observed that the nucleus is able to bypass the microposts by permitting deep local invaginations while maintaining the overall oval nuclear shape; this permitted unhindered forward motion of the nucleus through the micropost array. The regions of near-constant curvature in the lobes on either side of the invaginations suggest a surface tension in the nuclear surface which balances intranuclear pressure. This surface tension and pressure are mediated largely by lamin A/C because *Lmna*$^{-/-}$ nuclei deform with long extensions suggestive of a lack of resistance to areal expansion and get entangled on the microposts. *Lmna*$^{-/-}$ nuclei thus are never unable to build a pressure owing to a lack of a surface structure that supports a tension to resist the pressure. In contrast to *Lmna*$^{-/-}$ nuclei, Lamin A S22A/S392A expressing nuclei are able to initially support a pressure, but eventually lose the pressure due to rupture, resulting in similar entanglements around the microposts as *Lmna*$^{-/-}$ nuclei.

The motion of the nucleus through the micropost array is reminiscent of the behavior of a liquid drop encountering slender obstacles. This liquid-drop like behavior is demonstrated more directly in Figure 20, top panel, which shows an oil drop with higher surface tension deforming with a narrow, local invagination around the object such that apposing surfaces come together in the wake of the object while the overall oval shape of the drop is preserved. In contrast, the indentation of the oil drop with a lower surface tension causes a more extreme shape distortion from the starting oval shape (Figure 20, bottom panel). In an analogous manner, lamin A/C appears to create a nuclear surface tension that allows bypassing of the nucleus around slender objects by permitting deep invaginations while maintaining the original overall nuclear shape. Removal of

lamin A/C appears to reduce the surface tension, as evident from the distortion of the overall nuclear shape and nuclear entanglement around the microposts.

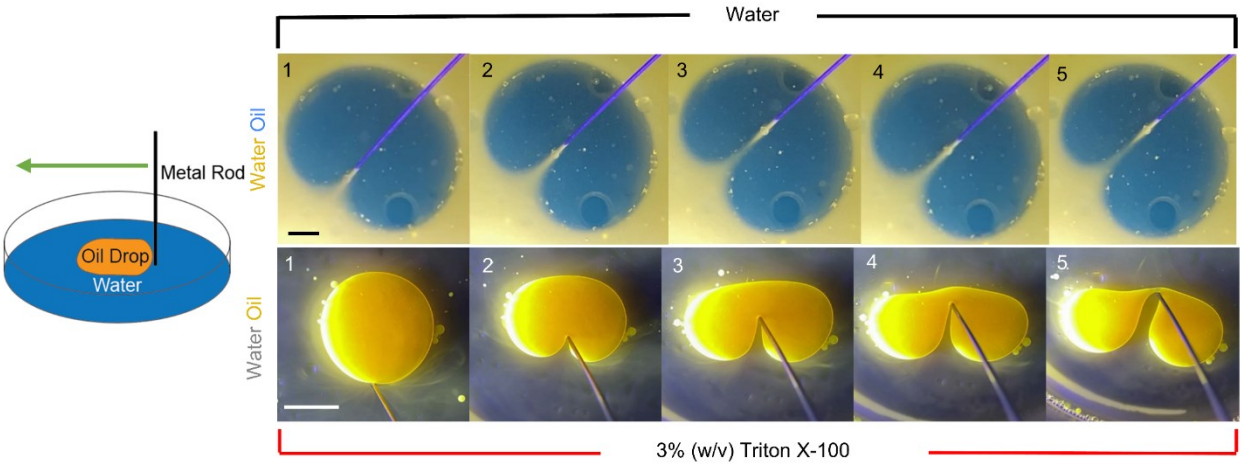


**Figure 20. Deformation of an oil drop with a metal wire. (Top) An oil drop (blue) in water (yellow) indented with a metal wire (diameter is 0.5 mm). (Bottom) An oil drop (yellow) in 3% (w/v) Triton X-100 in water indented with the same metal wire (Scale bar is 5 mm).**

Unlike an oil drop in water, where the surface tension arises from intermolecular attraction within each phase, surface tension in the nucleus arises due to resistance of the nuclear lamina to areal expansion. The source of tension in the lamina is likely the increase in nuclear pressure upon nuclear flattening in spread cells [33,94] as well as the compression of the nucleus against the microposts. Lamin A/C is required to sustain this tension. These results are consistent with our previous finding that lamin A/C limits the flattening of nuclei in spreading cells due to resistance to its areal expansion [27].

It is well known that on short time scales, nuclei can behave visco-elastically [3,13,20,21,96-101]. These measurements are typically on the time scale of several seconds, while our observations are on the order of minutes to hours. Thus, it is difficult to extrapolate the short-term measurements

to the long-timescale behavior. Also, we have previously shown that on the time scale of cell migration, nuclear deformations that occur during migration are not elastic and are primarily limited by the resistance of the lamina to areal expansion and the nuclear volume to compression ([23,27], and reviewed in [33,94]). That is, on longer time scales, deformed nuclear shapes in cells are not restored following the removal of cellular forces because of any elastic energy stored in the nuclear shape. However, a pressurized nucleus will tend to maintain an oval shape due to its surface tension, much like a liquid drop.

Our finding of lower forces for more significant deformations of the nuclear surface as compared to AFM measurements taken on a shorter time-scale (seconds), the lack of correlation between force and invagination length at deeper invaginations, the liquid-like behavior of the nucleus where the shape of the lobes between the microposts is determined primarily by the nuclear pressure and surface tension, and the qualitative differences between nuclear shapes indented with a probe in several seconds and nuclear shapes that invaginate over several minutes around microposts in migrating cells, are all also consistent with the notion that any elastic energy stored in the deformed nuclear shape dissipates on the much longer time scale of cell migration [23].

The three-dimensional extracellular matrix through which cells migrate offers distinct types of barriers to cell migration, including pores and slender fibers. Lamin A/C hinders migration through narrow pores in 3D gels [2,14,75,76] and confining microfabricated channels [2,83,86]. This is because the tensed lamina resists the areal expansion required for the nucleus to pass through narrow pores and channels [33,65]. However, in the context of fibrous environments, our results point to a new mechanism in which nuclear surface tension imparted by lamin A/C facilitates cell migration around slender obstacles by preventing entanglement of the nucleus.

## 3.5 Materials and methods

### *3.5.1 Micropost design and fabrication*

The height of the microposts was selected such that the micropost height is similar to the nuclear height. [102] The micropost patterns were designed in AutoCAD 2018. Circles of diameter 1 μm were placed on corners of an equilateral hexadecagon (side length = 7.71 μm). The side length of the hexadecagon was selected such that the area enclosed by the hexadecagon equaled the average cell spreading area (~1200 $\mu m^2$ for NIH 3T3 fibroblasts). The center-to-center distance between the micropost was selected such that the minimum edge-to-edge distance between any two adjacent microposts (6.6 μm) was less than the average diameter of the nucleus (~10 μm for NIH 3T3 fibroblasts). This hexadecagon pattern was arrayed onto an area of 1 cm by 1 cm. A P-type silicon wafer of diameter 100 mm was coated with a 1-micron AZ1512 photoresist. The above AutoCAD design was patterned on a chrome-coated glass mask using a Heidelberg MLA-150 DWL 66 laser writer. The glass mask and wafer were then mounted and exposed on an MA6 contact aligner and then developed using a 4:1 AZ-300MIF solution. Wafer was etched on Oxford DRIE, and the photoresist was removed using $O_2$ plasma. Post fabrication, the wafer was coated with (tridecafluoro-1, 1, 2, 2-tetrahydrooctyl)-1-trichlorosilane (T2492, UCT Inc., Bristol, PA, USA) (~50 nm thick using Chemical Vapor Deposition) to ensure low adhesion of PDMS on the wafer and hence promote easy peeling.

A negative mold was prepared from a patterned master silicon wafer using PDMS (Sylgard 184, Dow Corning, Midland, MI, USA) mixed at the base to cross-linking agent ratio of 10:1 (w/w) and cured at 60°C for 2 hours. The negative was peeled from the wafer and cut into blocks. These blocks contained the patterned area. A block was then covered with an evenly spread layer of uncured PDMS (mixed at the base to cross-linking agent ratio of 10:1 (w/w)) and pressed against

a No.1.5 glass-bottom dish (FD35-100, WPI Inc., Sarasota County, FL, USA). The dish with the negative mold was cured at 60°C for 2 hours to form the micropost topology on the glass surface.

### *3.5.2 Flexural rigidity*

Flexural rigidity of collagen fibers or PDMS microposts was calculated as $EI$ where $E$ is Young's modulus, $I = \frac{\pi r^4}{4}$ is the second moment of inertia for a cylindrical geometry, and $r$ is the radius of the cylinder. $E$ for collagen fibrils is reported to be in the range of 100 MPa to 360 MPa [103]. For average fiber diameters of 0.41 ± 0.09 μm in our collagen gels, $EI = 1.37 \times 10^{-16}\ \mathrm{Nm^2}$ to $4.94 \times 10^{-16}\ \mathrm{Nm^2}$ for collagen fibers which is roughly comparable to $EI = 1.11 \times 10^{-16}\ \mathrm{Nm^2}$ for PDMS microposts (PDMS mixed at 10:1 base to cross-linker ratio and cured at 60°C for 2 hours) of 1 micron in diameter. Young's modulus of PDMS was measured experimentally. Samples were prepared as per ASTM D412-C standards. PDMS was mixed at a 10:1 base-to-cross-linking agent ratio and cured at 60°C for 2 hours. Ten samples were tensile tested on an Instron 6800 series universal testing system, and stress-strain curves were acquired and analyzed to determine Young's modulus of PDMS. The Young's modulus was measured to be 2.27±0.04 MPa.

### *3.5.3 Stable cell lines and plasmids*

To construct the mCherry-ABD-KASH2-IRES-GFPx3-N144 pBabe puro plasmid, GFPx3-N144 was amplified from GFPx3-N144 pcDNA3.1 [104] using primers (5') TGTGGTGGTACGTAGGAATTCGGTTTAAACGCCACCATGGTGAGCAAG (3') and (5') ACACACATTCCACAGGGTCGACTTAAGGGGATTC (3') and inserted into a SnaBI, and SalI cut pBabe puro plasmid. An IRES amplified from pMSCV-IRES-mCherry (a gift from Dario Vignali, Addgene plasmid # 52114) using primers (5') TGTGGTGGTACGTAGGAATTCGAATTC GCGGGATCAATTCCG (3') and (5')

CTTGCTCACCATGGTGGCGTTTAAACTTATCGTGTTTTTC (3') and inserted on the N terminus of GFPx3-N144 pBabe puro. mCherry-ABD-KASH2 pBabe puro was cloned by fusing the actin-binding domain (aa 1-286) to the KASH domain (6825-6884) of human Nesprin 2 (NP_055995.4). This was amplified using primers (5') TCCGGACTCAGATCTCGAGGCGCATCTAGTCCTGAGCTT (3') and (5') TAACTGACACACATTCCACAGGGTCGACCTATGTGGGGGGTGGCCCATTG (3') and inserted into XhoI, and SalI cut mCherry-NLS pBabe puro plasmid. mCherry-ABD-KASH2 pBabe puro was then amplified with primers (5') GATCCCAGTGTGGTGGTACGTAGCCACCATGGTGAGCAAGGGCGAGGAGG (3') and (5') GGGCGGAATTGATCCCGCGAATTCCTATGTGGGGGGTGGCCCATTG (3') and inserted into SnaBI, and EcoRI cut IRES-GFPx3-N144 pBabe puro to create mCherry-ABD-KASH2-IRES-GFPx3-N144 pBabe puro. Human lamin A, in frame with GFP, was subcloned into pBabe.puro cut with EcoRI and PmeI using a forward primer TGTGGTGGTACGTAGGAATTCGCCACCATGGTGAGCAAG and a reverse primer CGACTCAGCGGTTTAAACCTACATGATGCTGCAGTT. NIH 3T3 cells stably expressing GFP-BAF WT were created as described previously. [104] MCF10A breast epithelial cells stably co-expressing GFP-N144 [104] and mCherry-KASH-ABD-Nes2 and NIH 3T3 cells stably expressing GFP-Lamin A or GFP-53BP1 were generated by retroviral transduction as described. [64] A-type lamin–deficient (*Lmna*$^{-/-}$) MEFs and WT MEFs were generously provided by Yixian Zheng (Carnegie Institution for Science, Washington, DC, USA) and were derived from *Lmna*-knockout mice [105] using methods described previously. [106] GFP-Lamin-A S22A/S392A (a generous gift of the Goldman lab) was described previously. [95] Lipofectamine 3000 (L3000001, Invitrogen,

Carlsbad, CA, USA) was used for transient transfections as per the manufacturer's recommended protocol.

### *3.5.4 Cell culture and drug treatments*

All cells were maintained in a humidified incubator at 37°C and 5% $CO_2$. NIH 3T3 fibroblasts (CRL-1658, ATCC, Manassas, VI, USA) were cultured in Dulbecco's Modified Eagle's Medium with 4.5 $g.L^{-1}$ glucose (10-013-CV, Corning, Corning, NY), supplemented with 10% v/v donor bovine serum (16030074, Gibco, Waltham, MA, USA) and 1% v/v penicillin/streptomycin (30-002-CI, Corning, Corning, NY, USA). MCF10A human breast epithelial cells (CRL-10317, ATCC, Manassas, VI, USA) were maintained in DMEM/F12 medium (11039-021, Invitrogen, Carlsbad, CA, USA) supplemented with 20 $ng.ml^{-1}$ epidermal growth factor (AF-100-122, Peprotech, Rocky Hill, NJ, USA), 0.5 $mg.ml^{-1}$ hydrocortisone (50-23-7, Sigma-Aldrich, St. Louis, MO, USA), 100 $ng.ml^{-1}$ cholera toxin (9012-63-9, Sigma-Aldrich, St. Louis, MO, USA), 100 $mg.ml^{-1}$ insulin (11070-73-8, Sigma-Aldrich, St. Louis, MO, USA), 1% v/v penicillin-streptomycin (30-002-CI, Corning, Corning, NY, USA), and 5% v/v horse serum (16050-122, Invitrogen, Carlsbad, CA, USA). MDA-MB-231 (HTB-26, ATCC, Manassas, VI, USA) were cultured in Leibovitz's L-15 Medium (10-045-CV, Corning, Corning, NY, USA), supplemented with 10% v/v donor bovine serum (16030074, Gibco, Waltham, MA, USA) and 1% v/v penicillin/streptomycin (30-002-CI, Corning, Corning, NY, USA). MDCK (NBL-2) (CCL-3, ATCC, Manassas, VI, USA) cells were cultured in DMEM with 4.5 $g.l^{-1}$ glucose (10-013-CV, Corning, Corning, NY), supplemented with 10% v/v donor bovine serum (16030074, Gibco, Waltham, MA, USA) and 1% v/v penicillin/streptomycin (30-002-CI, Corning, Corning, NY, USA). MEF WT and MEF *Lmna*$^{-/-}$ cells were cultured in DMEM with 4.5 $g.l^{-1}$ glucose (10-013-CV, Corning, Corning, NY), supplemented with 15% v/v donor bovine serum (16030074, Gibco,

Waltham, MA, USA) and 1% v/v penicillin/streptomycin (30-002-CI, Corning, Corning, NY, USA).

For actomyosin inhibition experiments, cells were seeded on rhodamine-conjugated fibronectin (FNR01, Cytoskeleton Inc., Denver, CO, USA) coated microposts, followed by a replacement of media containing DMSO (control) (BP231-4, Fisher Scientific, Hampton, NH, USA) or 25 μM Y-27632 (Y0503, Sigma-Aldrich, St. Louis, MO, USA) or 50 μM Blebbistatin (B0560, Sigma-Aldrich, St. Louis, MO, USA) within 2 hours after seeding cells. Samples were incubated in the treatment media for 12 hours, fixed with 4% paraformaldehyde (J61899, Alfa Aesar, Haverhill, MA, USA) at room temperature for 15 minutes, and washed thrice with 1X PBS (21-040-CM, Corning, Corning, NY, USA).

### *3.5.5 Fluorescent labeling*

The micropost pattern was coated with rhodamine-conjugated fibronectin (FNR01, Cytoskeleton Inc., Denver, CO, USA) at a concentration of 5 $\mu g.ml^{-1}$ to promote cell adhesion while fluorescently- labeling the microposts. For imaging F-actin, plasma membrane, or nuclei in some experiments, cells were fixed in 4% paraformaldehyde (J61899, Alfa Aesar, Haverhill, MA, USA) at room temperature for 15 minutes and washed thrice with 1X PBS (21-040-CM, Corning, Corning, NY, USA). Hoechst (875756-97-1, Sigma-Aldrich, St. Louis, MO, USA) was used to stain DNA, and Alexa Fluor-488 phalloidin (A12379, ThermoFisher Scientific, Waltham, MA, USA) was used to stain F-actin in fixed samples. NucSpot Live 650 (40082, Biotium, San Francisco, CA, USA) was used to stain DNA in live cells. PlasMem Bright Red (P505, Dojindo Molecular Technologies, Inc., Rockville, MD, USA) was used to stain the plasma membrane. All reagents were used at the concentration recommended by the manufacturer.

### *3.5.6 Microscopy*

Imaging was performed on a Nikon Ti2 eclipse laser scanning A1 confocal microscope (Nikon, Melville, NY, USA) with DU4 detector using Nikon CFI Plan Apo Lambda 60X/1.4 NA oil immersion objective lens (MRD01605, Nikon, Melville, NY, USA). Immersion oil Type 37 (16237, Cargille Labs, Cedar Grove, NJ, USA) was used at 37°C (*R.I.* = 1.5238 for $\lambda$ = 486.1 nm). Alternatively, imaging was performed on an Olympus FV3000 (Olympus Scientific Solutions Americas Corp., Waltham, MA, USA) using Super Apochromat 60x silicone oil immersion lens (UPLSAPO60XS2, Olympus Scientific Solutions Americas Corp., Waltham, MA, USA) or on a Zeiss LSM 900 (Carl Zeiss Jena GmbH, Jena, Germany) with Airyscan 2 using W Plan-Apochromat 20x/1.0 objective (421452-9681-000, Carl Zeiss Jena GmbH, Jena, Germany) or C Plan-Apochromat 63x/1.4 Oil objective (421782-9900-000, Carl Zeiss Jena GmbH, Jena, Germany). For 3D confocal imaging of fixed samples, a pinhole opening of 1 Airy disk was selected and a z-step size of 100 nm or 250 nm to ensure overlapping z-stacks while sampling at less than half of the depth of focus (which corresponds to an optical section of ~500 nm for 488 nm light) to satisfy Nyquist criterion and minimize photobleaching artifacts [107]. Live time-lapse cell imaging was performed in a heated and humidified chamber (Tokia Hit USA Inc., Montgomery, PA, USA), and cells were maintained at 37°C and 5% $CO_2$. For live-cell time-lapse 3D confocal imaging, a pinhole opening of 1.2 Airy disks (which corresponds to an optical section of ~600 nm for 488 nm light) and a z-step size of 1 micron was used to minimize phototoxicity and photobleaching of fluorescent probes.

For SEM imaging, PDMS microposts were fabricated on a 2 cm by 2 cm piece of a silicon wafer. Capsules containing PDMS micropost were then dehydrated in a graded ethanol series 25%-100%, at 10-min intervals for each 5% increment, followed by two exchanges of anhydrous

ethanol. The dehydrated micropost was loaded into a critical point dryer, Tousimis Autosamdri-815 (Rockville, MD, USA), with $CO_2$ as the transition fluid and in stasis mode overnight. The critical-point-dried PDMS microposts were mounted on carbon adhesive tabs on aluminum specimen mounts and rendered conductive with Au/Pd using a DeskV Sputter Coater (Denton Vacuum, Moorestown, NJ, USA). The microposts were imaged using a Hitachi SU5000 Schottky field emission SEM (Hitachi High-Technologies, Schaumburg, IL, USA) operated at 5kV.

### *3.5.7 Collagen Gels*

Gels were designed for low collagen fiber density (0.5 $\mu g.ml^{-1}$) to increase the probability of constricted migration and large fiber diameters (0.409 ± 0.093 μm) to increase aggregate fiber stiffness. Rat tail type-1 collagen solution of concentration 0.5 $\mu g.ml^{-1}$ in a complete cell culture medium was neutralized to *pH* = 7.0 with 1N NaOH and pipetted to glass-bottom microplates (MatTek Corporation, Ashland, MA, USA). The collagen solution was allowed to polymerize at 4 °C overnight and then at 37 °C for 30 min to finish the polymerization. The polymerized collagen gel was then labeled with 50 $\mu g.ml^{-1}$ Alexa Fluor 594-conjugated-NHS ester dye (A20004, Thermo Fisher, Waltham, MA, USA) in *pH* = 8.7 NaHCO3 buffer for 1 h at 37 °C, followed by 3 rounds of 1X PBS wash before seeding the cells. NIH 3T3s expressing GFP-BAF were then seeded onto the labeled collagen gel in a complete cell culture medium and incubated at 37° C overnight before imaging. GM6001 (364206-1MG, Sigma-Aldrich, St. Louis, MO, USA), a broad-spectrum matrix metalloproteinase inhibitor, was added to the cell culture medium at a concentration of 10-20 μM to inhibit matrix metallopeptidase activity and minimize collagen fiber degradation. Static or time-lapse confocal images were taken with a Zeiss LSM800 confocal microscope, equipped with an environmental control chamber and a 40X water-immersion lens (*N.A.* = 1.1).

### *3.5.8 Microneedle indentation*

Nuclei of cells adherent on a glass-bottom dish were deformed using a Tungsten microneedle (MN005S, MicroProbes, Gaithersburg, MD, USA) with a 1-micron tip diameter, bent such that the tip approached nearly perpendicular to the base of the dish. The microneedle was attached to an Injectman 4 micromanipulator (5192000027, Eppendorf, Enfield, CT, USA) to control nuclear deformation.

### *3.5.9 Oil drop experiments*

Canola oil was mixed with highlighter ink (in trace amounts) and suspended in water or water with 3% (w/v) Triton X-100 Detergent Solution (85111, ThermoFisher Scientific, Waltham, MA, USA). The oil drop was then visualized in blacklight as it was deformed by a thin steel wire 0.5 mm in diameter.

### *3.5.10 Nuclear or micropost height measurements*

X-z projections were reconstructed using NIS-Elements AR 5.02.01, and the maximum intensity projection was applied to the reconstructed images. Intensity profiles along the object's axial direction (in the z-direction) were exported to Origin PRO (OriginLab Corporation, Northampton, MA, USA). A Gaussian non-linear fit based on the Levenberg-Marquardt algorithm was applied to the intensity values, and the top and bottom edges of the nucleus or the micro were determined with the full width at half maximum method (FWHM) [108] function in Origin. The distance between the top and bottom edge of the nucleus or the micropost was reported as the corresponding height.

### *3.5.11 Deflection measurements*

We measured how the deflection vector (the vector joining the centroids of the bottom of the micropost with the top of the micropost) of the micropost was modified after contact with the

nuclear surface (Figure 15A, brown and red arrows). Z-planes corresponding to the top and bottom of the fluorescently labeled microposts were acquired. The deflection of a micropost was calculated with an automated program written in MATLAB 2019a (MathWorks, Natick, MA, USA). Centroid-detection-based particle-tracking routines described earlier [109] were employed to detect and quantify the micropost-coordinates. Briefly, a bandpass filter and a brightness threshold were applied to the raw images to isolate the micropost from the background. The centroid position of each micropost was calculated by fitting 2-D Gaussians to the pixel-intensities around the object of interest, where the peak position of the Gaussian fit was reported as the centroid. Vectorial subtraction between the centroid of the bottom of the micropost and the top of the micropost was reported as a deflection vector. Differential deflection vector was calculated by vectorial subtraction of the micropost deflection vector just before nuclear contact from the micropost deflection vector at a given time point (blue arrows in Figure 15B). For representing the deflection vector on images, arrows were scaled ten times the actual vector. The differential force component normal to the nuclear surface (Figure 15A, orange arrow) is the force associated with the local indentation of the nuclear surface due to the micropost. To calculate the differential deflection vector component, a line was drawn to join the two protruding nuclear surfaces around the micropost. This line was then rotated 90° to get the direction normal to the nuclear pocket around the micropost (see Figure 15A, magenta arrow). The differential deflection vector component along the direction normal to the nuclear surface in subsequent time frames was calculated and reported as the differential micropost deflection normal to the nuclear surface (Figure 15B, white arrows). The magnitude of force was calculated under the assumption of a uniformly distributed force across the length of the micropost, which is reasonable given that the nuclear contact with the micropost is relatively uniform throughout the micropost height (see Figure 11). The uniformly

distributed load was calculated as $w = \frac{8EI}{l^4}\delta$ where $\delta$ is the measured deflection of the top of the micropost relative to micropost bottom, $E = 2.27 \pm 0.04$ MPa is Young's modulus of PDMS mixed at the base to cross-linking agent ratio of 10:1 (w/w) and cured at 60°C for 2 hours, $I = \frac{\pi r^4}{4}$ is the area moment of inertia of the circular cross-section of the micropost of radius $r$, and $l$ is the length of the micropost. The force associated with a contact by the nucleus was determined by multiplying the uniformly distributed load force per unit length by the length of the microposts (5 μm) and reported as the total force in Figure 15E.

### *3.5.12 Nuclear speeds*

For automated analysis of nuclear speeds, a custom program was written in MATLAB 2019a. First, a threshold was applied to the time-lapse images of nuclei stably expressing GFP-BAF. Then, the nuclei boundaries were traced using MATLAB protocols to filter the image using a feature size-based bandpass filter, binarize (black/white) the image, fill interior gaps, and perform edge-detection. Area and perimeter filters were employed to identify nuclei and differentiate them from noise. Finally, the coordinates of each nuclear centroid were calculated as the mean of X and Y coordinates of the identified nuclear boundary. The centroid displacement against time was fitted with a straight line, and the average of the slopes was reported as the average nuclear speed (Figure 10G).

### *3.5.13 Circularity and curvature measurements*

The Auto-threshold function in ImageJ was used to determine the nuclear boundaries from images of nuclei fluorescently labeled with Hoechst or GFP-BAF. After thresholding, the Fill Holes function was used to fill holes inside the nuclear bounds and binarize the image. The values of perimeter and area were acquired with the Measure function in ImageJ. Circularity was

calculated using the formula, $C = \frac{4\pi A}{P^2}$ where, $C$ is the calculated circularity, $A$ is the measured area, and $P$ is the measured perimeter. Curvature was measured using the Kappa Curvature analysis plug-in in FIJI. To measure the total surface area of the nucleus, first, confocal z-stacks of Hoechst-stained nuclei were acquired using a z-step size of 250 nm.

### *3.5.14 Statistical analysis*

GraphPad Prism 9.0 was used for statistical analysis and graphical representations of data. On box plots, the central mark indicates the median, bottom and top edges of the box indicate the 25th and 75th percentiles, respectively, and whiskers extend to the most extreme data point. Statistical tests included Student's t-test, Brown-Forsythe and Welch analysis of variance (ANOVA) test, Kruskal-Wallis test and Mann-Whitney test. Differences between values were considered statistically significant when $p < 0.05$ and non-significant (ns) for $p > 0.05$. The sample size (n) for each statistical analysis is indicated in individual figure legend and the sample sizes used were sufficient to perform statistical analyses. All cell-culture experiments were performed independently at least thrice.

# CHAPTER 4

# REPAIR OF NUCLEAR RUPTURES REQUIRES BARRIER-TO-AUTOINTEGRATION FACTOR [*]

## 4.1 Overview

Cell nuclei rupture following exposure to mechanical force and/or upon weakening of nuclear integrity, but nuclear ruptures are repairable. Barrier-to-autointegration factor (BAF), a small DNA-binding protein, rapidly localizes to nuclear ruptures; however, its role at these rupture sites is unknown. Here, we show BAF rapidly and transiently localizes to the sites of nuclear rupture. BAF subsequently recruits transmembrane LEM-domain proteins, causing their accumulation at rupture sites. Loss of BAF impairs recruitment of LEM-domain proteins and nuclear envelope membranes to nuclear rupture sites and prevents nuclear envelope barrier function restoration. These results reveal a new role for BAF in response to and repair of nuclear ruptures.

## 4.2 Introduction

The nuclear envelope (NE) is a specialized extension of the endoplasmic reticulum (ER) that exists during interphase to surround and separate the nucleus from the cytoplasm. Ruptures in the interphase NE can occur during cell migration through confined spaces [14], and such rupture has been implicated in promoting invasive cancer cell migration through the exposure of the DNA to cytoplasmic exonucleases [15]. Mechanisms exist to functionally repair the NE subsequent to

nuclear rupture, which minimizes the negative consequences of disrupting this critical subcellular barrier [14,65,110]. But the mechanisms of how the envelope repairs itself are not understood. The DNA-binding protein barrier-to-autointegration factor (*BANF1*, BAF) is a small 89 amino acid (aa) protein that forms obligate dimers, each subunit of which binds dsDNA, allowing BAF to 'bridge' two strands of dsDNA [32]. BAF dimers bind to a single LEM-domain [111-113] (Lap2, Emerin, Man1), structural motifs found on several proteins, including many in the INM. BAF has also been reported to interact with various other proteins, including A-type lamins [114-116], various transcriptional regulators [115-118], and histones [116]. Localizing to the nucleus, the cytoplasm, and the NE, BAF binds to viral dsDNA in the cytosol with both pro-and anti-viral effects [119-123]. BAF has also been shown to function in post-mitotic nuclear reassembly, in part by recruitment of NE membranes to the reforming nucleus [124,125]. NE membrane recruitment is likely via LEM-domain interactions and via dsDNA-binding and compaction to cross-bridge chromosomes, enabling the formation of a single nucleus [126]. BAF has been shown to also localize to sites of nuclear ruptures [14]; however, the mechanisms and/or functions of this localization remain unclear. Here we hypothesized that non-phosphorylated cytosolic BAF transiently localizes to nuclear ruptures in a dsDNA-binding-dependent manner. Once localized to rupture sites, we hypothesized that BAF is required to recruit INM LEM-domain proteins and membranes to sites of nuclear rupture and to repair the compromised NE to restore the nucleo-cytoplasmic barrier functionally.

### 4.3 Dynamics of GFP-BAF recruitment at the point of envelope rupture

To assess the behavior of GFP-BAF during nuclear rupture, we challenged the GFP-BAF and mCherry-NLS expressing cells to navigate the confinement channel in the microfluidic device shown in Figure 21 and described in section 4.6.14 [31].

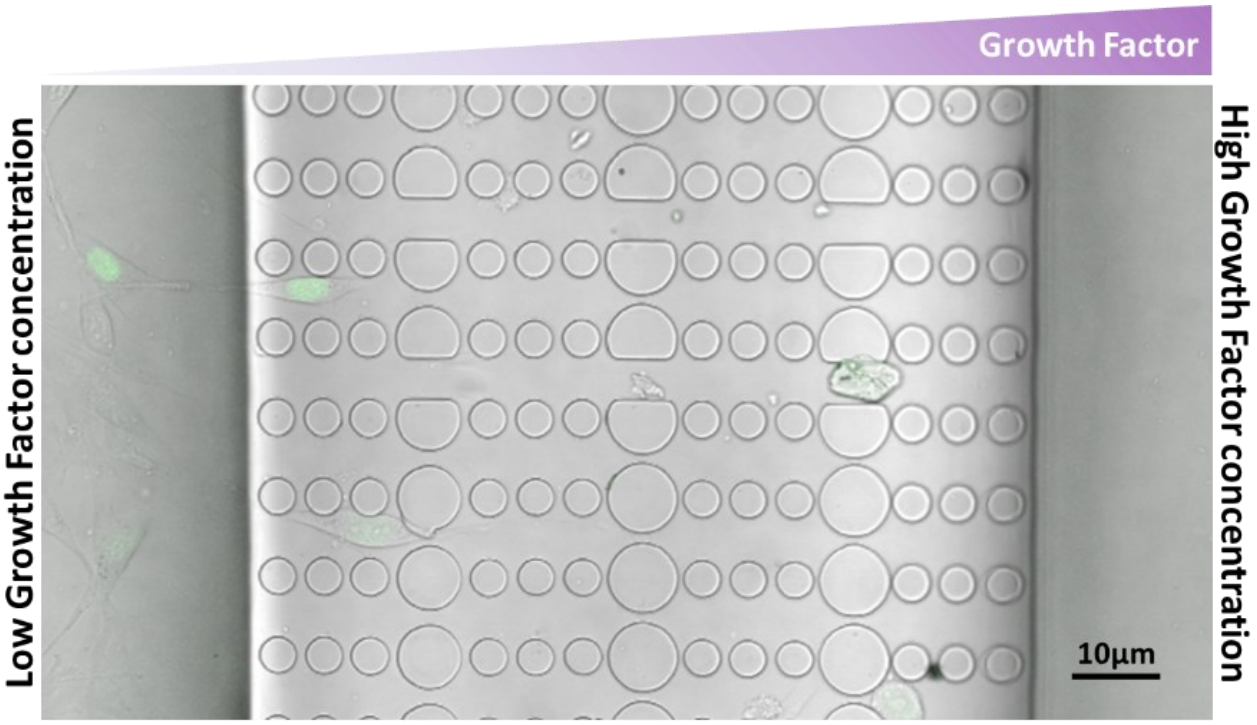


**Figure 21. Images show fibroblasts expressing GFP-NLS migrating in the confinement channel of the microfluidic device. A gradient of Platelet-Derived Growth Factor-AA (PDFG-AA) is established from right to left to achieve directed cell migration.**

mCherry tagged nuclear localization sequence (NLS) is imported into the nucleus. Upon the loss of nuclear envelope integrity, NLS freely diffuses into the cytoplasm. This construct was used as a reporter of envelope rupture. The nuclear rupture was evident in the diffusion of mCherry-NLS from the nucleus to the cytosol (Figure 22, right panel) as the nucleus was squeezed into an hourglass shape. We detected enrichment of the GFP-BAF almost immediately (localization time was in seconds) at the ruptured pole of the nucleus (Figure 22, left panel). Tracking the ruptured nucleus over longer times revealed a reimport of NLS into the nucleus along with the redistribution of GFP-BAF into the cytoplasm (Figure 22, red and black curves, respectively), suggesting transient localization of BAF at the site of NE rupture.

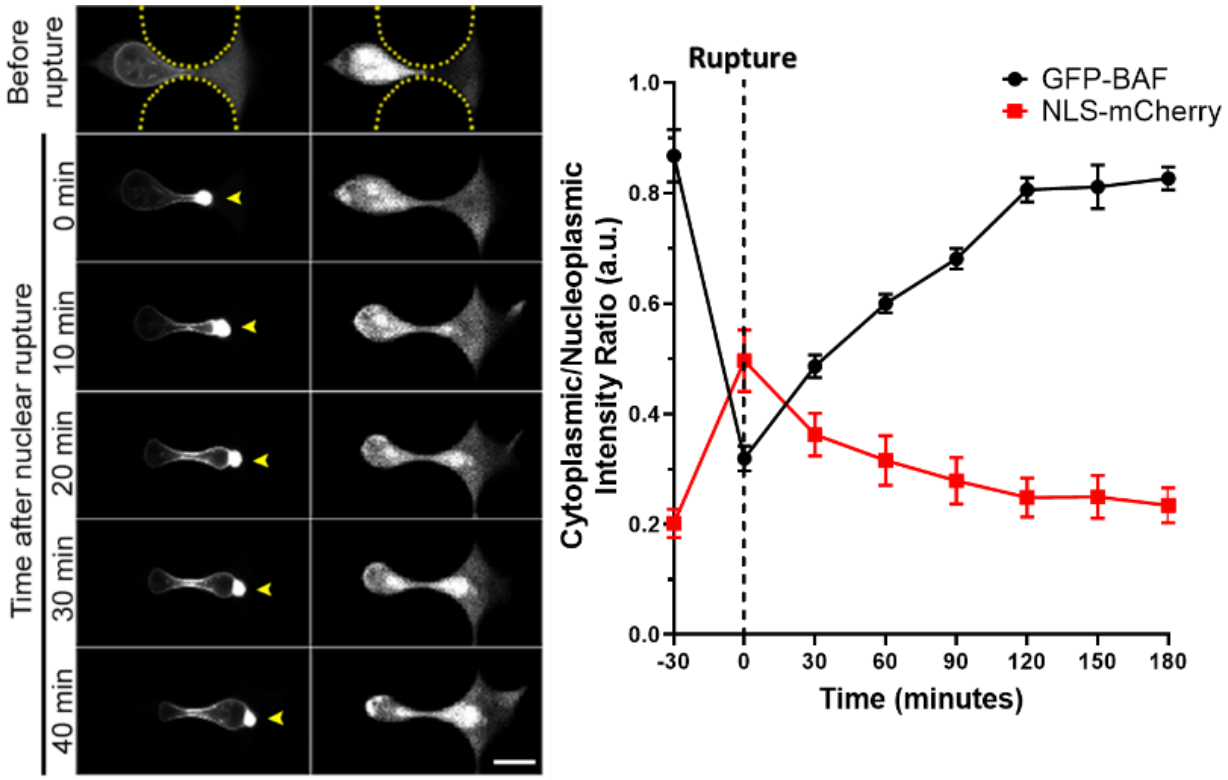


**Figure 22. (Left) Sequential time-lapse images of a representative NIH3T3 cell co-expressing**

**GFP-BAF and mCherry-NLS undergoing nuclear rupture during confined migration through a channel (height, 5 µm, width 3 µm) in the microfluidic device. Sites of nuclear rupture are indicated by BAF accumulation (yellow arrowheads). Scale, 10 µm. (Right) Plot shows the ratio of cytoplasmic to nucleoplasmic intensity (mean values ± SEM, n = 10 cells) of GFP-BAF and mCherry-NLS, before, at, and after nuclear envelope rupture with a time resolution of 30 minutes.**

### 4.4 Effect of BAF- knockdown on nuclear rupture repair

In an effort to understand whether BAF plays a role in nuclear rupture repair, we knocked down BAF through transfection with small interfering RNA (siRNA) against BAF in NIH 3T3 fibroblasts stably expressing GFP-NLS. The GFP-NLS intensity in BAF-depleted nuclei that ruptured during migration in the confining channels did not recover to pre-rupture levels (red curve in Figure 23), unlike control cells transfected with Scrambled RNA (siSCRAM). This observation shows that the envelope did not repair itself in BAF-depleted cells, confirming our hypothesis that BAF is required for NE repair after rupture.

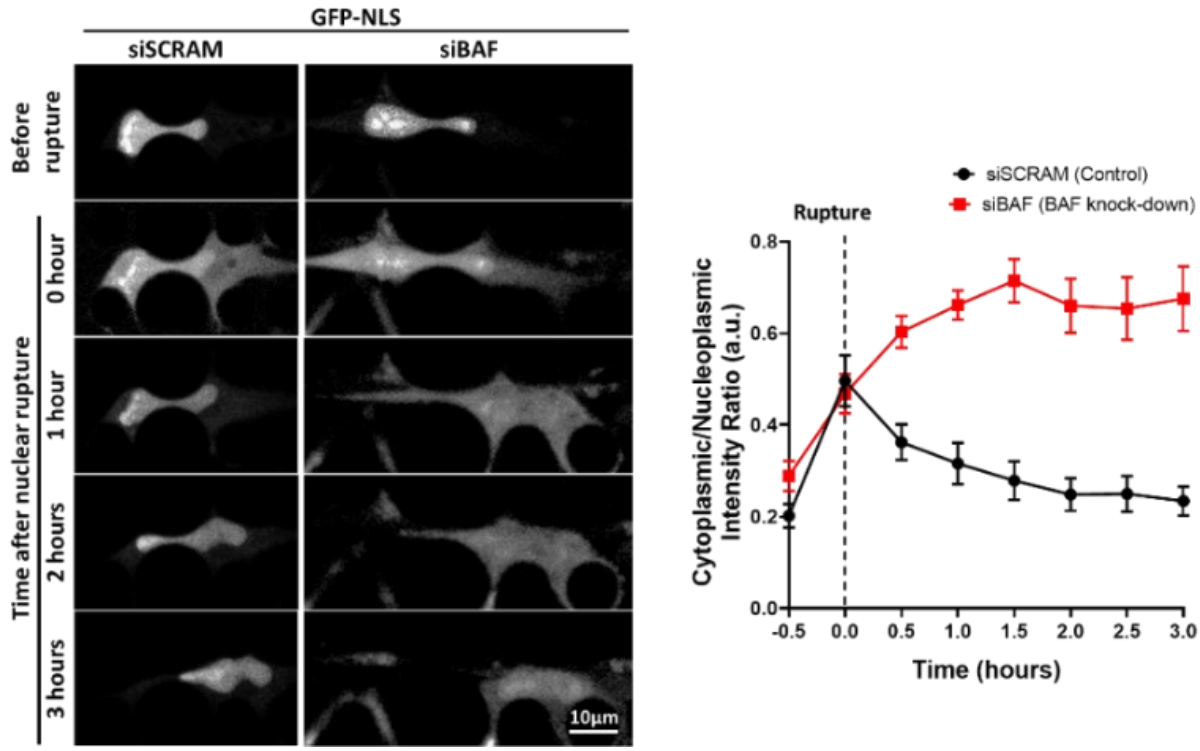


**Figure 23. (Left) Representative time-lapse images of control (siSCRAM) and BAF KD (siBAF) NIH3T3 cells expressing GFP-NLS stably, and undergoing nuclear rupture during confined migration through a channel (height, 5 µm, width 3 µm) in the microfluidic device. Scale ,10 µm. (Right) Quantification of cytoplasmic/nucleoplasmic ratios of GFP-NLS from NIH3T3 cells transfected with either siSCRAM (control) or siBAF siRNAs prior to rupture during confined migration in channels (height, 5 µm, width 3 µm). The graph represents mean values ± SEM (n = 10 cells for each condition; **p<0.0001 from siControl by mixed-effects model).**

To explore how BAF may participate in NE repair, in collaboration with the Roux lab, we focused on the inner nuclear membrane (INM) constituent- LEM domain proteins (Lap2, Emerin, Man1). It is known that BAF proteins are required to recruit at least some LEM domain proteins

to the newly forming NE following mitosis [124]. Therefore, we hypothesized that BAF might recruit transmembrane LEM-domain proteins during the repair of NE rupture during interphase and participate in membrane recruitment to repair the NE. In control cells, the stably expressed GFP-tagged LEM-domain proteins, except for Lap2β, all were substantially enriched at the rupture sites within a couple of minutes following rupture induced by laser irradiation (Figure 24). Upon BAF depletion, the GFP-LEM-domain proteins failed to accumulate at the rupture sites (Figure 24).

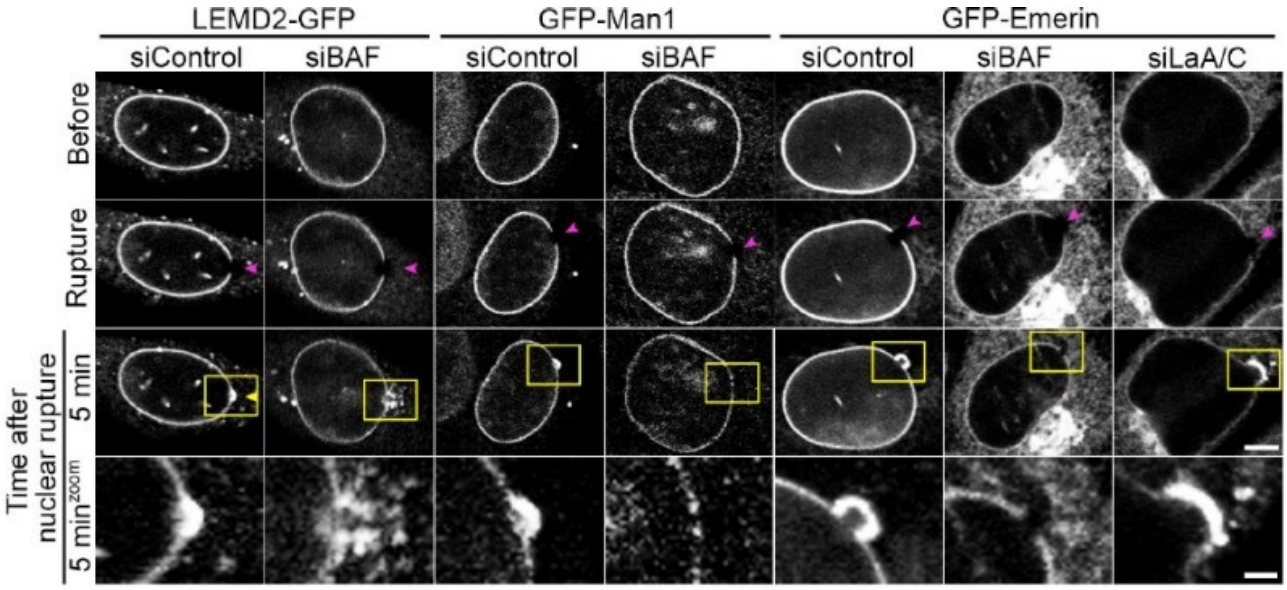


**Figure 24. NIH3T3 cells expressing GFP-tagged LEM-domain proteins LEMD2, Man1, or Emerin were transfected with either siBAF, siControl, or siLaA/C (for GFP-Emerin expressing cells) for 72 hours prior to laser-induced nuclear rupture (purple arrowhead). Accumulation, or the lack thereof, of each LEM domain protein at rupture sites (yellow arrowhead), is monitored over 5 min.**

Collectively these studies support a model in which BAF is required to repair the NE after nuclear rupture via the recruitment of transmembrane LEM proteins and their associated membranes to sites of nuclear rupture (Figure 25). It is increasingly clear that nuclear rupture may

be a mechanism of disease, at least for cancer and laminopathies, and given BAF's role in repairing those ruptures, it seems likely that regulation of BAF may provide a potential mechanism for interference in those disease processes.

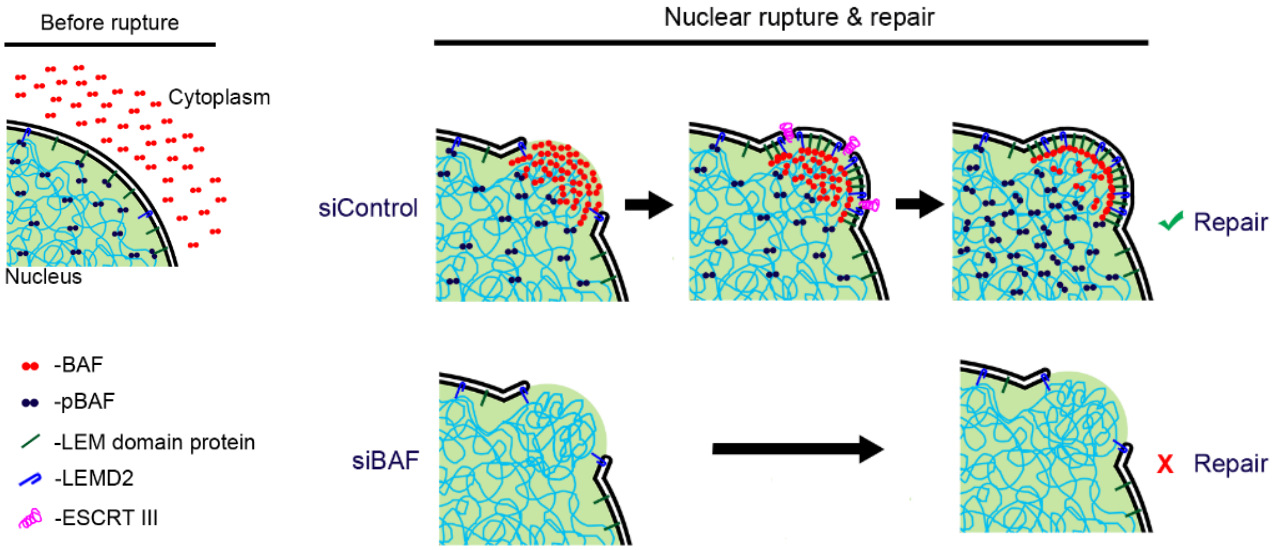


**Figure 25. A model for NE rupture repair. In control cells (siControl), cytosolic BAF is recruited to the nuclear rupture via DNA binding, followed by the subsequent mobilization of LEM-domain proteins, ESCRT-III, and membranes to the rupture. Loss of BAF (siBAF) results in failure to functionally recruit ESCRT-III, LEM-domain proteins, and membranes resulting in a failure to repair the NE rupture.**

## 4.5 Materials and methods

### *4.5.1 Cell culture*

NIH3T3 and HEK293T Phoenix cell lines were cultured in Dulbecco's modified Eagle medium with 4.5 g/L glucose, L-glutamine, and sodium pyruvate (DMEM; Corning). BJ-5ta cell lines were cultured in DMEM supplemented with a 4:1 ratio of Medium 199 (Sigma-Aldrich) and 0.01mg/mL hygromycin B. MCF10A cell lines were cultured in Mammary Epithelium Basal

Medium (MEBM, Lonza) supplemented with MEGM® SingleQuots® with the following modification: Gentamicin sulfate-Amphotericin (GA-1000) was omitted from media, and cholera toxin (Sigma-Aldrich) was added at a final concentration of 100 ng/ml. All media was supplemented with 10% (v/v) fetal bovine serum (FBS; Hyclone) at 37°C with 5% $CO_2$ in a humidified incubator.

### *4.5.2 Construction of stable cell lines*

NIH3T3 cell lines stably expressing fluorescent proteins were generated using retroviral transduction. For this, HEK293T Phoenix cells were seeded in 2 mL DMEM in a 6-well plate at 90% confluence and incubated overnight to allow for cell attachment. 1µg of pBabe-puro or -neo plasmid DNA encoding the protein of interest was transfected into the attached Phoenix cells using Lipofectamine 3000 (ThermoFisher) following the manufacturer's instructions. After overnight incubation, cells were transferred to 32°C for 24 hr. The culture media was collected and filtered through a 0.45µm filter and added to NIH3T3 cells (target cells), along with polybrene (2.5 µg/mL; Santa Cruz Biotechnology), and incubated at 37°C for 24 hr. Cells were trypsinized, collected through centrifuging at 250xg for 5 min, and incubated in fresh DMEM containing puromycin (0.5 µg/mL; Thermofisher) or G418 sulfate (30µg/mL; Santa Cruz Biotechnologies) for selection of viral integration for 2-3 days for pBabe-puro plasmids and 5-7 days for pBabe-neo plasmids. The expression of fluorescent proteins in cell lines was verified using immunofluorescence and immunoblot analysis.

### *4.5.3 siRNA transfection*

All siRNA transfections were performed using RNAiMAX (ThermoFisher) according to the manufacturer's instructions. Cells were trypsinized and seeded into 2 mL DMEM in 6 well plates at 70% confluency and incubated overnight to allow cells to adhere to the bottom of the

well. ON-TARGETplus SMARTpool siRNAs (Dharmacon) against mouse BAF (NM_011793.3), mouse LaA/C (NM_001002011.3), Human BAF (NM_003860.3), Human LEMD2 (NM_181336.4), Human Emerin (NM_000117.2), Human Ankle2 (NM_015114.3), and Human Chmp7 (NM_152272.4) were used for gene knockdowns, including a non-targeting (NT) control (Table S2). 30 pmol siRNA (1.5 µL of a 20 µM solution in RNAse free $H_2O$) were dissolved in 150 µL of 1x OptiMEM. 9 µL of RNAiMAX was diluted in 150 µL of 1x OptiMEM. Both solutions were combined, mixed by pipetting, and incubated for 5 min. The combined solution was then added to the attached cells and incubated for 72-96 hr. For 72 hr incubations, cells were split after 48 hr and transferred to 35 mm glass-plated fluorodishes (World Precision Instruments) and a 6-well plate in parallel for an additional 24 hr. For 96 hr incubations, cells were split after 72 hr and added to fluorodishes and a 6-well plate for an additional 24 hr. Combinatorial siRNA pools (siLEMD2, siEmerin, siAnkle2) were transfected twice during the 96 hr incubation to ensure efficient knockdown. Cells in fluorodishes were used for live-cell imaging, while cells in the 6-well plate were used to collect lysates for immunoblot to verify siRNA knockdown efficiency. For cell indentation experiments, cells were incubated with calcein-AM (Invitrogen, 2µg/ml) prior to experimentation.

### *4.5.4 Microfluidic design for confined migration*

We replicated the microfluidic device previously developed by Lammerding and coworkers [31] (Figure 21). A two-dimensional pattern prepared in AutoCAD 2018 was etched in a photoresist-coated Si wafer using two-layered SU-8 photolithography. The photoresist-coated wafer was fabricated by first spin-coating a 5 µm thick layer of SU-8 2010 photoresist on a Si wafer; then baked at 60°C for 10 minutes and exposed to UV light for etching through a photomask corresponding to the two-dimensional pattern. This pattern consisted of circles and semicircles of

varying diameters spaced at 2, 3, and 5 μm. After etching, another design was used to create 250 μm tall features in the photoresist for creating reservoirs at the end of the channels. To cast the device from the master wafer, polydimethylsiloxane (PDMS, Dow Corning Sylgard) was polymerized on it at a 10:1 (w/w) elastomer base to curing agent mix ratio by baking at 65°C for 2 hours. The PDMS was peeled from the wafer, and for each device, holes were punched on both sides across the channel using a biopsy punch of a diameter 5 mm for the media reservoir and a diameter 1 mm for cell-seeding. The device was treated with plasma for 2 minutes in a 400W plasma cleaner (PlasmaEtch PE-25), placed immediately in contact with a plasma-treated glass-bottomed dish, and pressed gently to ensure contact and bonding. The resulting device was baked for 15 minutes at 90°C to improve PDMS adhesion to glass, then sterilized using 200 proof ethanol, rinsed using de-ionized water, and dried using compressed nitrogen. After that, the device was incubated with 200 μg/ml fibronectin for 2 hours at 37°C. After the incubation, the device was rinsed with PBS and loaded with complete cell culture media before loading cells. 20,000 cells were seeded at 5000 cells/μl for each device. Subsequently, the device was placed inside a tissue culture incubator for a period of 12 hours to allow cell attachment. The media in the reservoir was replaced with serum-deprived media for NIH3T3 (97% DMEM, 2% DBS, 1% Pen-Strep) on the cell-seeded side of the channel, and complete cell culture media supplemented with Human PDGF-BB Recombinant protein (200 ng/ml) on the other side before mounting the device on the microscope. A stable chemotactic gradient of platelet-derived growth factor (PDGF-AA) was established between the channels to promote cell migration. The reservoirs were covered with sterilized glass coverslips to prevent evaporation and contamination.

### *4.5.5 Laser-induced nuclear rupture and live-cell imaging*

Live cells expressing fluorescently-tagged proteins of interest were seeded on 35 mm glass-bottomed fluorodishes in DMEM and allowed to attach overnight. The following day, the media was removed and replaced with pre-warmed phenol red-free DMEM with HEPES and FBS for imaging (Gibco). For fluorescent NE labeling, media was removed, and adherent cells were incubated with ER tracker red in 1xDPBS/modified media (Hyclone) at a final concentration of 0.5 μM for 30 min at 37°C and rinsed once with 1x DPBS/modified media prior to the addition of phenol-red free DMEM. Cells were imaged on an Olympus FV1000 confocal microscope and FV10-ASW v4.1 software, with a temperature-controlled chamber set at 37°C and 60x/NA 1.42 PlanApo N oil immersion objective (3x zoom). The 488nm and 543nm scanning lasers were used for GFP and mCherry imaging.

Laser-induced rupturing was carried out with a 405 nm excitation laser (6 sec for NIH3T3 cells; 8 sec for BJ-5ta cells) at 100% power (tornado scan mode), while utilizing the SIM-scan feature for simultaneously imaging and laser rupturing. GFP-BAF photobleaching was performed using the main scanner and 488nm laser at 100% power for 10 sec or until no noticeable signal was observed in either the cytoplasmic or nucleoplasmic compartments. LEMD2-GFP photobleaching was performed using the main scanner and 488nm laser at 100% power for 20 sec unless otherwise indicated, at which point no detectable signal was observed in the ER or NE. For testing for resealing of nuclear ruptures, GFP-NLS was photobleached using the main scanner and 488nm laser at 100% power for 40 sec. GFP-NLS measurements were performed in ImageJ v1.52i by measuring the mean intensity of a region of interest (ROI) over time. All images were processed in Adobe Photoshop CS6 for cropping and brightness/contrast adjustment when applicable.

### *4.5.6 Statistical analysis*

For the post-nuclear rupture GFP-BAF dynamics experiments and the NLS-reporter dynamics experiments, quantifications are reported as the mean plus or minus the standard error in the mean (SEM) (error bars). A mixed-effects model was used to analyze the relationship between groups performed in R and *nlme*, where time was considered a fixed and random effect while the treatment group was considered a fixed event. The interaction between time and treatment group was also considered. Significance was determined if $p<0.05$, and if significance was determined, a pairwise comparison using *lsmeans* was performed between groups using Tukey-adjusted p-values. For the cell indentation measurement experiments, quantifications are reported as the mean plus or minus the SEM (error bars). Unpaired student's t-tests were performed in R to compare each treatment to the control, with $p < 0.05$ used as the cutoff for significance.

# CHAPTER 5

# A METHOD FOR DIRECT IMAGING OF X-Z CROSS-SECTIONS OF FLUORESCENT SAMPLES [*]

## 5.1 Overview

The x-z cross-sectional profiles of fluorescent objects can be distorted in confocal microscopy, in large part due to a mismatch between the refractive index of the immersion medium of typical high numerical aperture objectives and the refractive index of the medium in which the sample is present. Here, we introduce a method to mount fluorescent samples parallel to the optical axis. This mounting allows direct imaging of what would normally be an x-z cross-section of the object in the x-y plane of the microscope. With this approach, the x-y cross-sections of fluorescent beads were seen to have significantly lower shape-distortions as compared to x-z cross-sections reconstructed from confocal z-stacks. We further tested the method for imaging nuclear and cellular heights in cultured cells and found that they are significantly flatter than previously reported. This approach allows improved imaging of the x-z cross-section of fluorescent samples.

## 5.2 Introduction

Confocal fluorescence microscopy has been the technique of choice to visualize x-z or axial cross-sectional views (i.e., images in a plane parallel to the optical plane) of microscopic fluorescent objects, using image slices acquired in the focal plane. However, reconstructed x-z cross-sectional profiles of fluorescent objects, which are the size of several microns, can be distorted in confocal microscopy [127,128]. These distortions are caused largely by the mismatch



[*] Reproduced from "Katiyar, A., Antani, J., McKee, B., Gupta, R., Lele, P. and Lele, T. (2021), A method for direct imaging of x–z cross-sections of fluorescent samples. Journal of Microscopy, 281: 224-230. https://doi.org/10.1111/jmi.12965" with permission from John Wiley & Sons, Inc.

between the refractive indices of the medium in which the sample is present and the oil present on typical oil-immersion objectives. The mismatch causes differences between axial travel of the objective relative to the sample and travel of the focal plane in the sample itself, resulting in distortion of the x-z shapes. Also, refractive-index mismatch causes the axial resolution to worsen and peak intensity to decrease with travel into the sample.

Methods to correct for the mismatch have been proposed, including the use of water-objective lenses and the calculation of correction factors [108,127,129]. Other recent approaches include the use of prisms to deflect light in such a way that the x-z cross-section can be directly imaged [93,130]. Here we developed an approach to image x-z shapes of fluorescent objects, which does not require scaling with correction factors or extra devices like prisms in the light path. We designed an imaging chamber in which samples could be mounted along a plane perpendicular to the focal plane, effectively making what would normally be a measurement in the x-z plane into a measurement in the x-y plane. Imaging of the x-y cross-sections of spherical polystyrene beads immersed in a mounting medium with an oil-immersion objective revealed a substantial reduction in distortion. We further tested the chamber for imaging cells and nuclei.

**5.3 Results**

A schematic of our mounting approach is shown in Figure 26. A 3D-printed chamber was designed to hold two glass slides perpendicular to the focal plane. The microscope objective was focused near the bottom edge of the glass slide, and the region was scanned to image fluorescent objects. In this setup, the glass slide is held parallel to the optical axis of the microscope, allowing us to image the cross-section orthogonal to the glass slide in the x-y plane (this cross-section would normally be the x-z cross-section reconstructed from confocal z-stacks).

We first reconstructed x-z cross-sections of fluorescent beads of known diameters from confocal z-stacks. We compared these x-z cross-sections to single confocal fluorescent images of x-y cross-sections of fluorescent beads in the orthogonal imaging chamber. All images were acquired on a laser scanning confocal microscope (see methods) using a Nikon CFI Plan Apo Lambda 60X/1.4 NA oil immersion objective lens. Beads were mounted on the glass slides in mounting media with a refractive index of 1.45, while the refractive index of oil was around 1.52. Consistent with previous reports [131], the x-z shapes of 10-15 µm fluorescent beads reconstructed from confocal z-stack imaging resembled a tear-drop shape (Figures 27A and 27C). The average change in the height of the bead was ~ 53 % for the 10 µm beads and ~ 45 % for the 15 µm beads (Figures 27B and 27D). This distortion was measured for confocal z-stacks acquired at a step-size of ~250 nm which is below the Nyquist criterion. Substantially lowering the step size to 50 nm did not decrease the distortion in the beads (Figure 28).

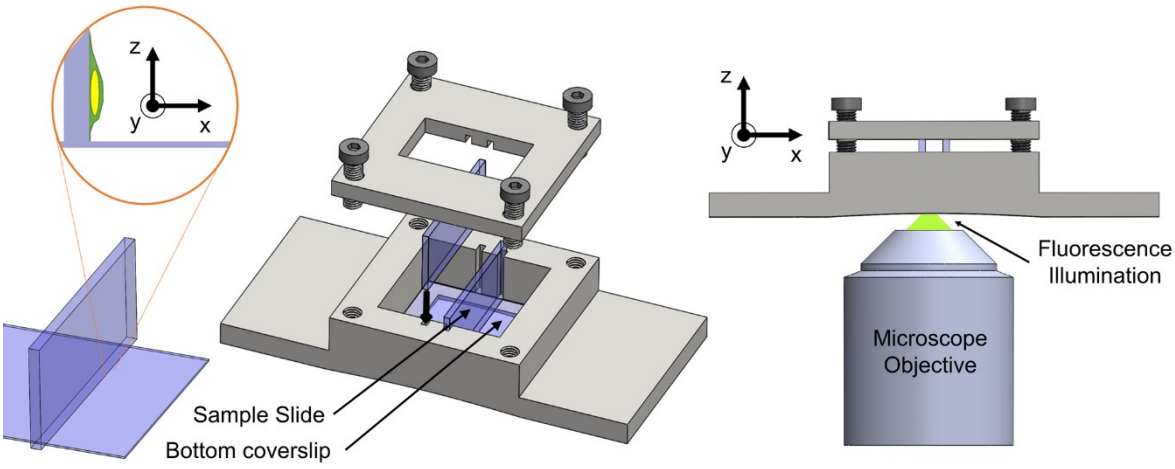


**Figure 26. Schematic of the orthogonal imaging chamber. The 3D-printed chamber holds slides in an orientation perpendicular to the focal plane. Tunnel slides are slotted vertically in the grooves along the walls of the chamber. A lid is tightened to push the tunnel slides against the bottom coverslip with threaded screws. A window is provided in the lid to enable**

**transmitted light microscopy. A photo of the imaging chamber (total length = 75 mm) is included.**

In contrast, images of the beads acquired with the orthogonal imaging chamber were not distorted by their circular shapes (Figures 27A and 27C, right). The measured heights were statistically indistinguishable from the diameter specified by the manufacturer (Figures 27B and 27D). Similar distortion-free imaging was achieved with much smaller beads of ~200 nm (Figure 29). These data demonstrate the utility of the orthogonal imaging chamber for reducing distortions in images of shapes captured orthogonal to the mounting surface.

We next evaluated the orthogonal imaging chamber for imaging non-spherical fluorescent structures. The cell nucleus is an example of such a structure as it generally looks circular in the x-y plane but is flattened considerably in the x-z plane such that its three-dimensional shape resembles an ellipsoid [9,27]. We imaged DNA stained with Hoechst H33342 in nuclei of three different cell types - NIH 3T3 fibroblasts, MCF10A mammary epithelial cells, and C2C12 myoblasts, by reconstructing x-z cross-sections on a conventional setup, and by direct imaging of x-y cross-sections in the orthogonal imaging chamber. X-y images of nuclei acquired with the imaging chamber were much flatter than x-z images of nuclei reconstructed from confocal image stacks **(**Figure 30A, 30B, and Table 1). The percentage error in mean nuclear heights was in the range of ~35% to ~62% (Table 1). These results reveal a substantial error in the vertical height of the nucleus measured from confocal z-sectioning and reconstruction of the x-z shape. As heights of spread cells in culture are very similar to nuclear heights, these results also suggest that cells are much flatter than suggested by confocal reconstructions.

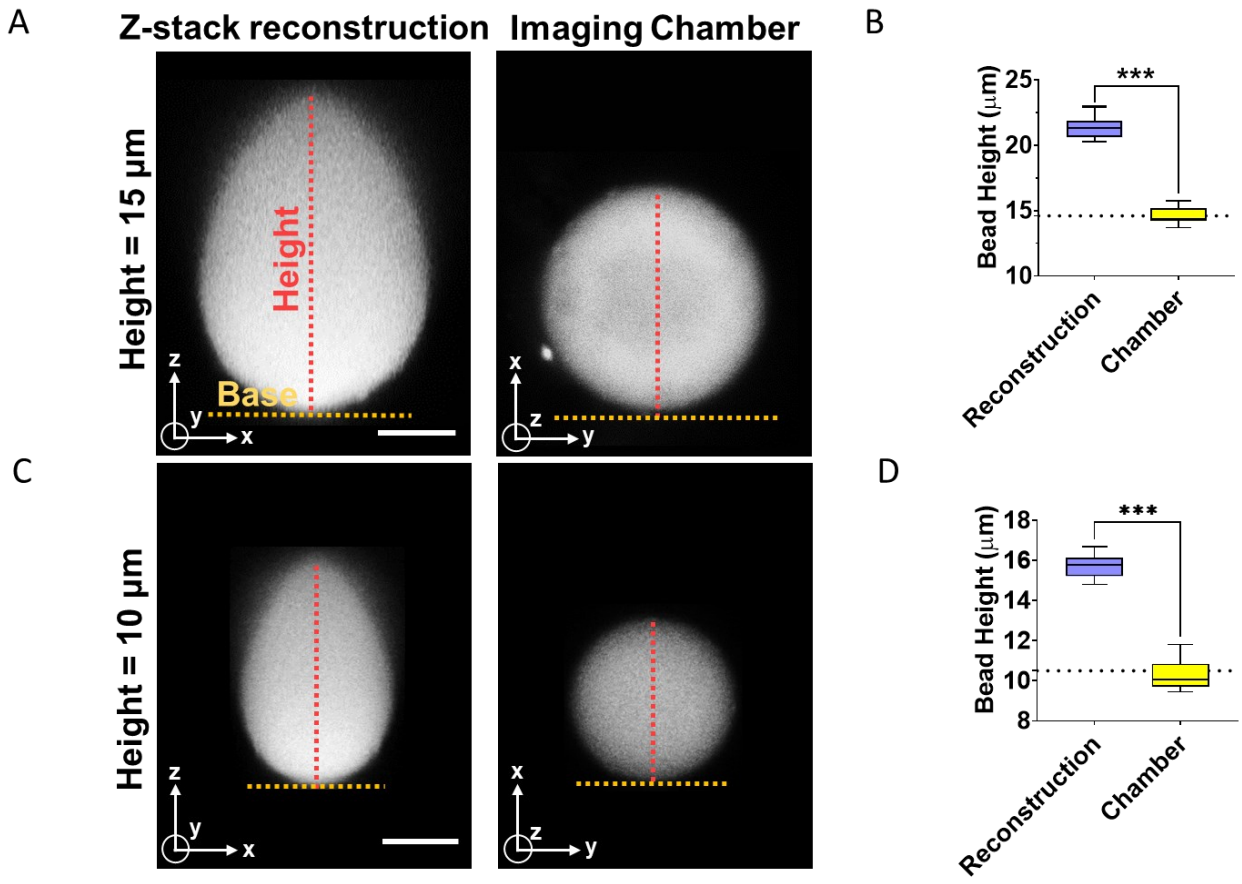


**Figure 27. Comparison of x-z shapes reconstructed from confocal sectioning and corresponding x-y shapes acquired in the orthogonal imaging chamber. (A) Image of x-z cross-section of the fluorescent bead (diameter = 15 µm) reconstructed from confocal z-stacks and acquired with the imaging chamber. Scale bar is 5 µm. (B) The graph shows a quantitative comparison of the diameter of beads (d = 15 µm) corresponding to the two imaging methods in (A). The dotted line represents the manufacturer's specification for the mean diameter of the bead. The experiments were performed in triplicates, and 20 beads were quantified (*** $p < 0.05$; Student's *t*-test). (C) Image shows an x-z cross-section of the fluorescent bead (diameter = 10 µm) reconstructed from confocal z-stacks and a single x-y image acquired with the orthogonal imaging chamber. Scale bar is 5 µm. (D) Graph shows**

**a comparison of the diameter of beads (d = 10 µm) corresponding to the two imaging methods in (C). Dotted line represents the manufacturer's specification for the mean diameter of the bead. The experiments were performed in triplicates, and 20 beads were quantified (*** p < 0.05; Student's *t*-test).**

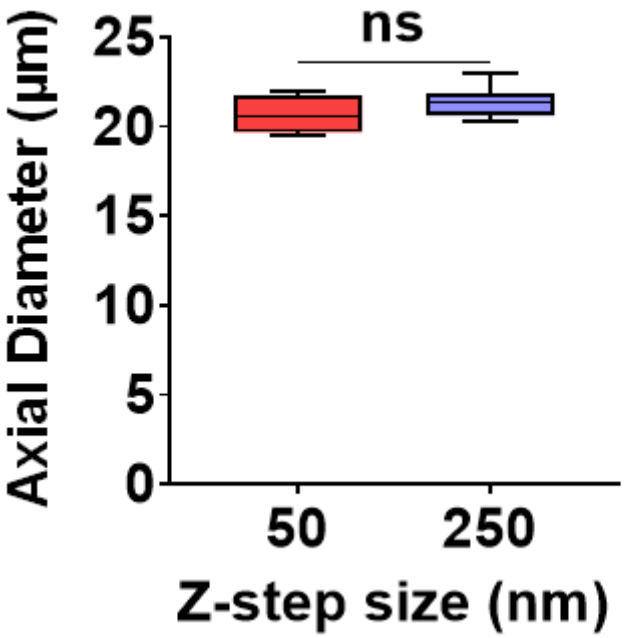


**Figure 28. Graph shows a comparison between the height of the bead (d = 15 µm) from reconstructed z-stacks of 50 nm and 250 nm step size. The experiments were performed in triplicates, and 20 beads were quantified for each condition (ns p > 0.05; Student's *t*-test).**

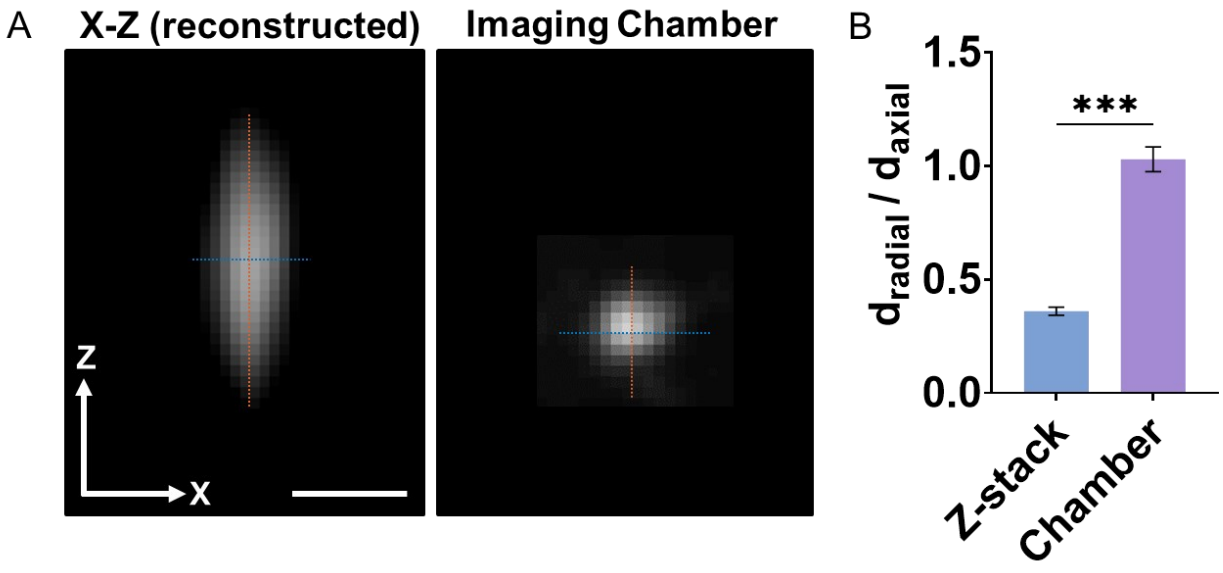


**Figure 29. Comparison of images of sub-resolution objects. (A) A representative image of a 200 nm bead reconstructed from confocal Z-stacks and a bead imaged in the imaging chamber is shown. Scale bar is 1 µm. (B) Graph shows the ratio of radial to axial diameter from reconstructed z-stacks or images from the axial imaging chamber. The experiments were performed in triplicates, and at least 10 beads were quantified (*** $p < 0.05$; Student's *t*-test).**

We next evaluated the imaging chamber for imaging non-spherical fluorescent structures. The nucleus of cells is an example of such a structure as it generally looks circular in the x-y plane but is flattened considerably in the x-z plane such that its three-dimensional shape resembles an ellipsoid [9,27]. We imaged DNA stained with Hoechst in nuclei of three different cell types - NIH 3T3 fibroblasts, MCF10A mammary epithelial cells, and C2C12 myoblasts, both with conventional confocal microscopy to reconstruct axial cross-sections and in the imaging chamber to directly perform axial imaging. Axial images of nuclei acquired with the imaging chamber were much flatter than axial shapes reconstructed from confocal image stacks (Figure 30A, 23B, and

Table 1). The percentage error in mean axial nuclear diameters measured by confocal microscopy relative to those measured with direct axial imaging in the imaging chamber was in the range of ~35% to ~62% in these cell types (Table 1). These results reveal a substantial error in axial height of the nucleus measured from confocal fluorescence microscopy.

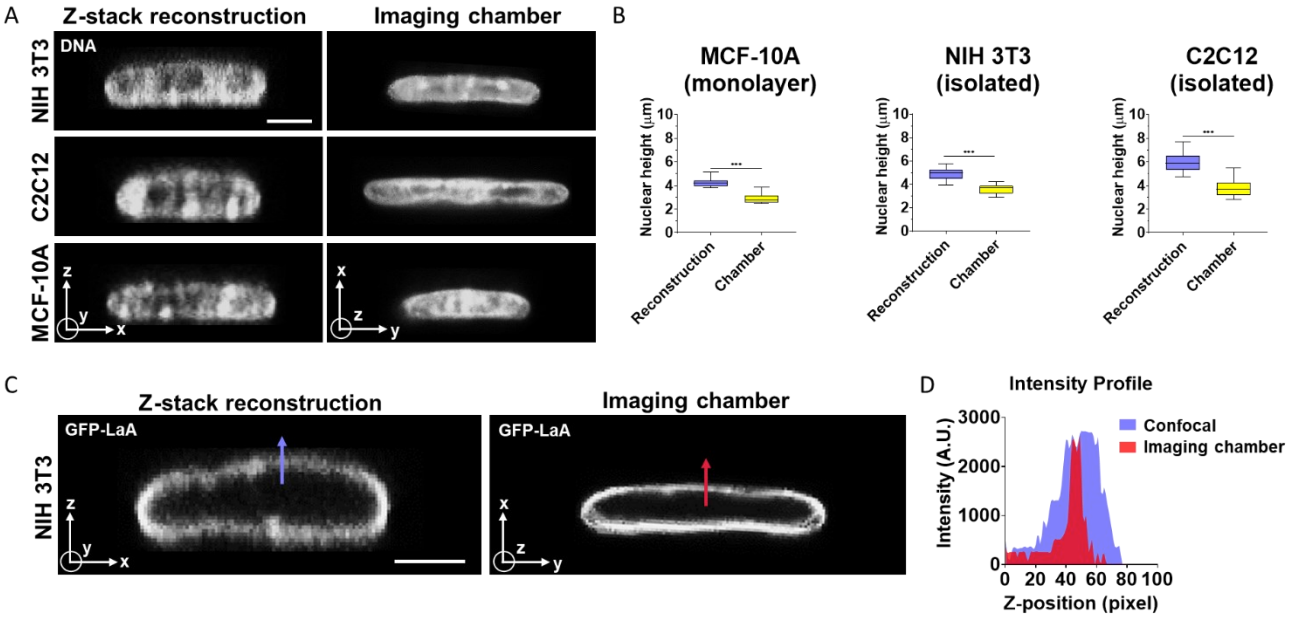


**Figure 30. Differences in nuclear heights were measured in x-z reconstructed images and x-y images acquired in the orthogonal imaging chamber. (A) Hoechst (H33342) stained x-z images of the nucleus in three different cell types reconstructed from confocal z-stacks and x-y images acquired in orthogonal imaging chamber. Scale bar is 5 μm. (B) Graphs show a quantitative comparison of nuclear heights for NIH 3T3 fibroblasts (left, isolated cells), C2C12 myoblasts (center, isolated cells), and MCF-10A (right, monolayer) for the two imaging conditions in (A). Images were acquired per cell type from at least 15 cells from three independent experiments (*** $p < 0.05$; Student's *t*-test). (C) x-z image of a GFP-lamin A expressing NIH 3T3 fibroblast nucleus reconstructed from z-stack confocal stacks (left)**

**and x-y image of a different nucleus imaged in the orthogonal imaging chamber (right). Scale bar is 5 μm. Blue and red arrows mark the length along which the intensity profile was measured (D).**

The nucleus is a core-shell structure, with the nuclear lamina (shell) enclosing DNA (core). We compared axial shapes of the GFP lamin A-labeled lamina in NIH 3T3 fibroblasts acquired by confocal fluorescence microscopy and direct axial imaging. The fluorescence of GFP-lamin A was diffuse in a direction perpendicular to the nuclear periphery in reconstructed x-z confocal images, while it was more localized and less diffuse in images acquired in the imaging chamber (Figure 30C and 30D).

**Table 1. Comparisons of nuclear height measured from confocal reconstruction and in the orthogonal imaging chamber. Nuclear heights were measured in three different cell types by reconstructing the x-z cross-section from confocal z-stacks of Hoechst-stained nuclei or x-y confocal images acquired in the orthogonal imaging chamber. Data is Mean ± SEM measured from n = 15 cells from three independent experiments.**

| **Height of Nucleus** | | | |
|---|---|---|---|
| **Cell type** | **Confocal stacks** | **Imaging chamber** | **% Error‡** |
| **NIH 3T3 fibroblasts** | 4.88 ± 0.11 μm | 3.61 ± 0.10 μm | ~ 35% |
| **C2C12 myoblasts** | 6.03 ± 0.19 μm | 3.73 ± 0.17 μm | ~ 62% |
| **MCF-10A** | 4.24 ± 0.09 μm | 2.83 ± 0.08 μm | ~ 50% |

**‡Percentage error was calculated using the formula $\frac{d_z - d_{ic}}{d_z} * 100$, where $d_z$ = mean height of the nucleus measured from confocal z-stacks and $d_{ic}$ = mean height of the nucleus measured by direct x-y imaging in the imaging chamber.**

As another example of non-spherical and non-symmetrical structures, we imaged the axial shape of the cell and the nucleus. In this experiment, we allowed cells to spread on the glass coverslips and then fixed cells at different times after seeding. This allowed us to capture the F-actin distribution in cells of different axial shapes and chromatin distribution in nuclei. Cells progressively flattened over 60 minutes of spreading, with the nucleus changing shape from rounder morphologies to flat morphologies (Figure 31). The blue arrows in Figure 31 reveal finer features in the nuclear shape and F-actin distribution. For example, F-actin tended to be enriched in local spots near the apical membrane early in the process of spreading and tended to be spatially inhomogeneous. Upon complete spreading, however, F-actin distribution tended to be less inhomogeneous and present in relatively uniform, thin structures at the apex and the base. Spatial variations in local curvature of the apical F-actin structure were also evident in the axial images of cells (marked by white arrowheads in F-actin images at 45' and 60' in Figure 31).

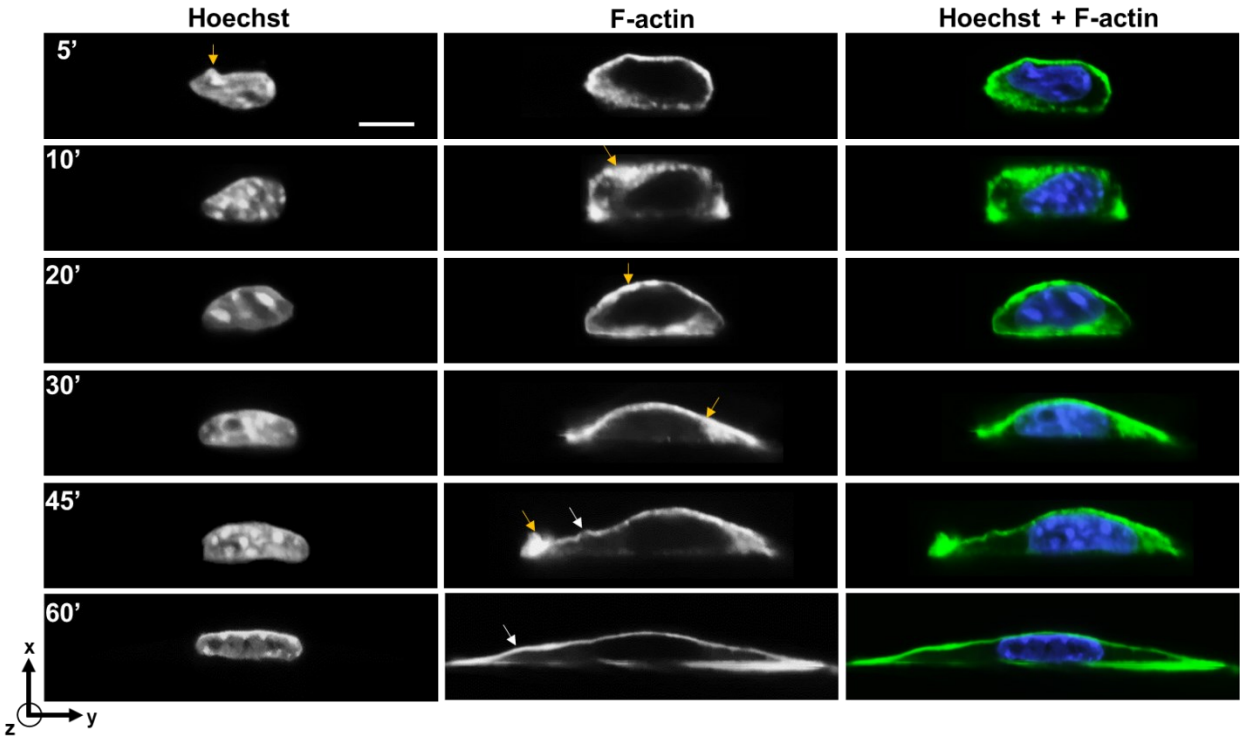


**Figure 31. X-y imaging of cells fixed at different time points after seeding onto a glass coverslip in the orthogonal imaging chamber. Chromatin was stained with Hoechst (H33342), and F-actin was stained with phalloidin. Yellow arrows mark local spots of F-actin enrichment and local nuclear irregularity in the image at 5'. White arrowheads mark spatial variations in the curvature of apical F-actin. Scale bar is 5 µm.**

### 5.4 Conclusion

Three-dimensional confocal microscopy is the technique of choice to visualize x-z cross-sections of particles and cellular structures, but these cross-sections are subject to considerable distortions owing largely to the phenomenon of refractive-index mismatch. Here we developed an approach for mounting samples side-ways such that what is normally the x-z cross-section for imaging conventional samples is directly imaged in the x-y plane in the orthogonal imaging

chamber. The chamber allows imaging of planes perpendicular to the glass slide with a resolution similar to that achieved in XY imaging. Additionally, the reconstruction needed to visualize x-z cross-sections is not required here, as only one image is required of the x-y plane. As such, our approach will have better time resolution than approaches that involve the reconstruction of confocal z-stacks.

Quantitative measurements of cell and nuclear heights have been performed from x-z cross-sections reconstructed from confocal microscopy of x-y planes captured at different z-positions [9,22,23,27,54,130,132-141]. Such measurements have allowed mechanistic studies of cell spreading and nuclear flattening. Our estimates of error in nuclear heights show that confocal reconstructions significantly overestimate these parameters. Such errors can confound interpretation, particularly where treatments or perturbations to cells cause subtle differences in nuclear heights or cellular heights.

One limitation of our approach is that cells can only be imaged close to the edge of the glass slide because of the low working distance of typical 60X or 100X objectives. Nonetheless, for an imaging depth of 70-100 μm with reference to the top surface of the coverslip and an imaging width of 15 mm for our glass slides, the area over which imaging can be performed is 1 – 1.5 $mm^2$, which enables imaging of a substantially large number of micron-sized objects. Further, the area of imaging may also be increased by using objectives that have high working distances. The vertical mounting of cells could potentially impact their shapes due to gravity. However, we have shown that gravity does not affect the shape of cells as they adhere and spread on a surface [27]. This was done by allowing cells to adhere for a short time on a surface, and then inverting it such that gravity acted against the cells. We found no difference in the degree of cell flattening

even against gravity. This is consistent with the fact that gravitational forces on cells are very small compared to forces associated with molecular motors that drive cell spreading [142].

Another limitation is the use of tunnel slides which limits the exchange of media. This can be overcome by replacing tunnel slides with single glass slides and perfusing the chamber with liquid media to allow live-cell imaging. Fluorescence intensity drops with distance from the coverslip [143]. This could make it difficult to visualize dimmer samples in the orthogonal imaging chamber. While the point spread function becomes more diffuse laterally with depth [127], the gross shape of the object remains unchanged. Finally, the imaging chamber does not solve the problem of 3-D rendering of objects; any 3-D reconstructions will appear elongated in the z-direction.

The imaging chamber is compatible with both upright and inverted microscopes and can be coupled with micromanipulation devices for studying force-deformation relationships of soft particles or cells. Also, it may prove valuable in studying dynamic events in cells in the orthogonal direction, such as apical assembly and disassembly of F-actin structures and microtubules during the process of cell migration. For example, a similar orthogonal mounting approach as ours has been previously used by [141] to study cell migration. The improved resolution and time resolution offered by our approach should be especially useful in this regard.

## 5.5 Materials and methods

### *5.5.1 Orthogonal Imaging Chamber*

A 35 × 75 × 11.75mm (W×L×H) chamber was designed to hold two tunnel slides in an orientation perpendicular to the focal plane, as shown in Figure 26 and Figure 32. A 22mm × 22mm × 0.17 mm coverslip (Fisher Scientific, Cat. No. 12-542-B) was adhered to the bottom of the imaging chamber with RTV-108 glue (Momentive RTV Silicone Sealant) to protect the microscope objective from brushing against the edges of the vertical slides. Microscope glass

slides (VWR, Cat. No. 26004-422) and coverslips were cut (25mm x 11 mm and 22mm x 11 mm, respectively) to enable imaging with a long working distance condenser (Ti-C CLWD, Nikon Instrument Inc.). Two such slides were then inserted in the slotted grooves (8.75 x 1.3 mm with a depth of 1.75 mm) along the walls of the chamber. Once positioned, the vertical slides were pressed against the bottom coverslip by tightening the lid of the imaging chamber (35x35x3 mm) with four threaded screws (Figure 26). An imaging window was provided within the lid to enable simultaneous transmitted light and fluorescence microscopy. All the designs were developed with CAD software (SolidWorks, 3D Assault Systems) and 3D-printed (VeroWhite resin material, 3D printer: Stratasys Objet Eden 260V).

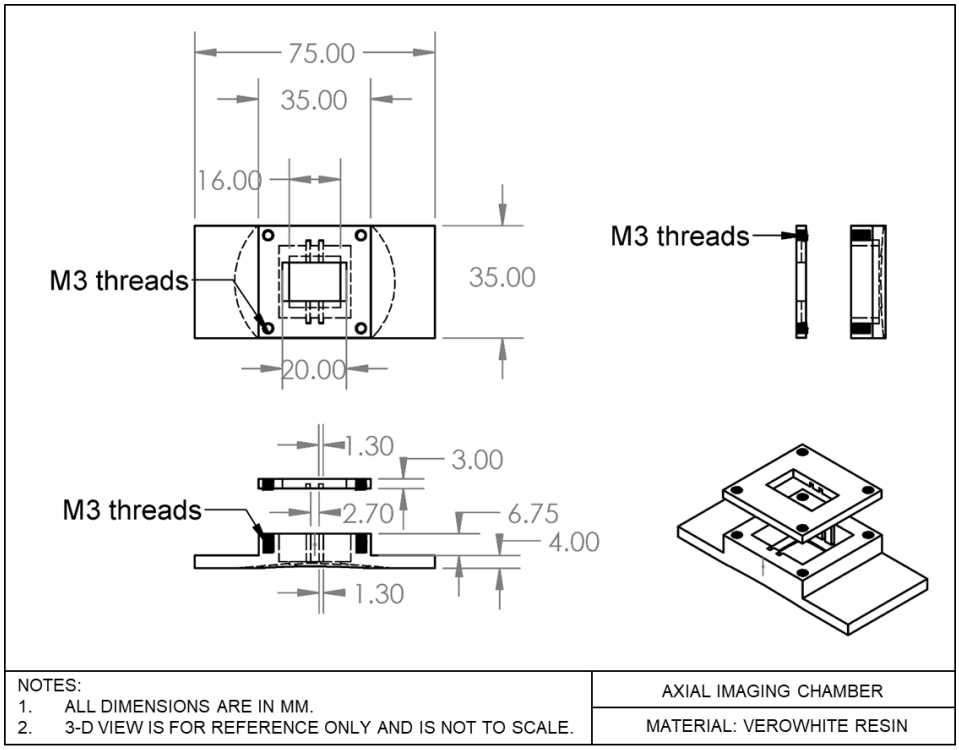


**Figure 32. Engineering drawing of the orthogonal imaging chamber.**

### *5.5.2 Cell culture*

Cells were maintained in a humidified incubator at 37°C and 5% CO2. NIH 3T3 fibroblasts stably expressing GFP-Lamin A, a kind gift from Kyle Roux, were cultured in Dulbecco's Modified Eagle's Medium (DMEM, 10313-021) with 4.5 g/L glucose (Corning, 25-037-CI), supplemented with 10% v/v donor bovine serum (DBS, Gibco, 16030074) and 1% v/v penicillin/streptomycin (Pen-Strep, Corning, 30-002-CI). C2C12 myoblasts (ATCC CRL-1772) were cultured in Dulbecco's Modified Eagle's Medium (DMEM, 10313-021) with 4.5 g/L glucose (Corning, 25-037-CI), supplemented with 10% v/v donor bovine serum (DBS, Gibco, 16030074) and 1% v/v penicillin/streptomycin (Pen-Strep, Corning, 30-002-CI). MCF10A human breast epithelial cells (ATCC CRL-10317) were maintained in DMEM/F12 medium (Invitrogen, 11039-021) supplemented with 20 ng/ml epidermal growth factor (EGF, Peprotech, AF-100-122), 0.5 mg/ml hydrocortisone (Sigma, 50-23-7), 100 ng/ml cholera toxin (Sigma, 9012-63-9), 100 mg/ml insulin (Sigma, 11070-73-8), 1% v/v penicillin-streptomycin mix (Pen-Strep, Corning, 30-002-CI), and 5% v/v horse serum (Invitrogen, 16050-122). Fixed and stained samples were mounted in a glycerol-based mounting medium (Cat #: H-1000, Vectashield, Vector Labs) with a refractive index of 1.45.

### *5.5.3 Immunostaining*

Cells were fixed in 4% paraformaldehyde (Alfa Aesar, J61899) at room temperature for 15 minutes and washed thrice with 1X PBS (Corning, 21-040-CM). Hoechst (H33342, Sigma-Aldrich, 875756-97-1) was used to stain DNA. Alexa Fluor-488 phalloidin (ThermoFisher Scientific, A12379) was used to stain actin filaments (f-actin).

### *5.5.4 Microscopy*

Imaging was performed on a Nikon A1 confocal unit complemented with a 4-channel 15 mW laser light source and mounted on a Nikon Ti2 eclipse microscope (Nikon, Melville, NY). The objective lens was a Nikon CFI Plan Apo Lambda 60X/1.4 NA oil immersion objective lens (MRD01605). We chose a pinhole opening of 1.2 Airy disks and a z-step size of 250 nm to ensure overlapping z-stacks while sampling at less than half of the depth of focus (which corresponds to ~ 600 nm for 488 nm light) to satisfy the Nyquist criterion and minimize photobleaching artifacts [144-148]. Immersion oil Type 37 (Cargille Labs, Cat #: 16237) was used at 37°C (R.I. = 1.52 for $\lambda$ = 486.1 nm). The microspheres were separated from the immersion oil by a glass coverslip (No. 1.5, R.I. = 1.52).

For confocal reconstruction, images were captured of 100 x-y planes at different z-positions separated by either 100 nm or 250 nm for each 15 μm microsphere. For the 10 μm microsphere, 50 x-y planes were imaged at z-positions separated by 250 nm. We first found a reference focal plane with an approximately maximal cross-sectional area when imaging in the orthogonal chamber. Next, we captured 5 images at x-y planes separated by 0.5 μm at z-positions above and below the reference focal plane. The focal plane with the maximum area was selected as the true cross-section of the object and was quantified.

### *5.5.5 Polystyrene beads*

We imaged commercially available fluorescent polystyrene microspheres of diameter 14.6 ± 0.146 μm from Molecular Probes, (F8837, $\lambda$ absorption = 365 nm / $\lambda$ emission = 415 nm) and of diameter 10.5 ± 0.152 μm from Corpuscular Inc. (Cat #: 141255-05, $\lambda$ absorption = 480 nm / $\lambda$ emission = 510 nm). Microspheres were mounted in a mounting medium (Cat #: H-1000, Vectashield, Vector Labs) with a refractive index of 1.45.

### *5.5.6 Quantitative analysis of images*

Cross-sections of microspheres were reconstructed using NIS-Elements AR 5.02.01, and the maximum intensity projection was applied to the reconstructed images. Intensity profiles along the direction perpendicular to the mounting surface were exported to Origin PRO (OriginLab Corporation). A Gaussian non-linear fit based on the Levenberg Marquardt algorithm was applied to the intensity values, and the top and bottom edges of the objects were determined with the full width at half maximum method (FWHM) [108] function in Origin. The distance between the top and bottom edge was reported as the diameter. A similar analysis was performed on images of nuclei to quantify their heights.

# CHAPTER 6

# CONCLUSIONS AND FUTURE WORK

## 6.1 Summary of findings

Cell migration in tissues occurs through gaps present in slender extracellular matrix fibers. How the cell deforms the nucleus mechanically, which allows it to bypass these fibers during migration, is not understood. In this dissertation, we provided the first evidence that Lamin A/C facilitates nuclear bypassing of obstacles during migration. We proposed a new model in which the nuclear lamina imparts a surface tension balanced by nuclear pressure. The resulting drop-like properties on the nucleus allow it to preserve its geometry even as deep invaginations form on its surface due to fiber obstacles, facilitating cell migration and passage through fibers by imparting a surface tension on the nucleus that prevents nuclear entanglement around fibers. We also showed that proximal cell protrusions drive the unfolding of the nuclear lamina as a migrating cell widens in shape. Finally, we reported that the barrier-to-autointegration factor (BAF) localizes early to the sites of nuclear envelope rupture during cell migration through confining channels and mediates repair of the nuclear envelope. Below we detail future studies that could be performed to solidify our findings further and improve our understanding of nuclear mechanics in migrating cells.

## 6.2 Outlook

Our results showed that the nuclear lamina confers a tension on the nucleus, allowing it to maintain its shape despite local invaginations on its surface. The tension in the lamina originates from the resistance of the lamina to stretch. One of the features of the model by Lele, Dickinson, and coworkers is that the lamina is too stiff to stretch on cellular force scales and that its total area remains constant. A further test of the model is to quantify the area of the lamina as it deforms

around the posts. However, total surface area measurements are susceptible to error because folds and bends in the nuclear lamina are frequently below the axial resolution of high-magnification objectives. One possible solution is to photobleach GFP-lamin expressing nuclei at regularly spaced spots along the nuclear circumference. As the nucleus encounters microposts, the length between the bleached spots is predicted to stay constant as the nucleus deforms around the microposts. Alternatively, the length could increase, which would then suggest that the nuclear lamina stretches during the invagination process.

If the nucleus does behave like a liquid drop with intranuclear pressure balanced by tension in the nuclear lamina, it could deform around the microposts at constant tension, or the tension could increase in case the pressure inside the drop increases. The nuclear lamina could support an increase in its tension without measurable changes in its area by analogy to a stiff spring that could sustain large forces without significant changes in its length. Measurement of the tension in the nuclear lamina could provide valuable insight into the mechanics of nuclear drop invagination. Measuring tension in the lamina in living cells is challenging but may be possible by inserting FRET-based tension-sensing modules in the *LMNA* gene. Tension sensing modules have proven useful in measuring molecular forces in other contexts, such as in focal adhesions [149].

Related to the above discussion is our remarkable observation that the nuclear envelope does not rupture in the vast majority of nuclei that deform around microposts (observed in ~5% of the cell population migrating on microposts). Ruptures typically occur when the envelope blebs and dissociates from the lamina, and the blebs eventually burst if the nuclear pressure increases sufficiently. In the small number of cases where blebbing does occur, it would be useful to track the nuclear membrane and detect if the rupture is accompanied by blebbing or whether there is perhaps a local weakening in the nuclear lamina due to a mechanical stretch that leads to local

blebbing. This possibility is at least partially supported by our observation that nuclei that rupture also tend to stall at the posts and do not continue moving against them. Perhaps the reason for the stall is that the lamina is not able to maintain its constant area, resulting in local tearing and rupture. Imaging experiments that track photobleached spot locations in the GFP-lamin A/C labeled nucleus could again shed light on this question.

An important question relates to the source of the excess area in the nucleus relative to the sphere. We speculate that the approximately spherical nuclei in trypsinized cells have excess area owing to the particular way in which the lamina is assembled post-mitosis. During mitosis, the nuclear envelope is disassembled, and cells are rounded. The mitotic spindle pulls chromosomes apart in daughter cells that still are rounded when the assembly of the nuclear envelope and the nuclear lamins begins again around the irregularly packed chromosomes. We posit that the irregular shape of the packed daughter chromosomes in the rounded cell results in an irregular 'coating' of the lamina (and envelope) around them, resulting in the excess area in the nucleus for its spherical shape. When the daughter cells spread, the irregular, roughly spherical shape of the nucleus must undergo a flattening. As the sphere is a minimum area to volume shape, flattening will necessarily cause an increase in the apparent area of the shape, resulting in the unfolding of the newly assembled irregular lamina and final smoothening of the lamina, at which point the nucleus reaches a steady-state shape. These speculations can be tested by tracking GFP-lamin expressing cells, measuring 3-D geometries of the packed chromosomes and newly assembled nuclei, and tracking these changes as the nucleus flattens in the spread daughter cells. Additionally, it is to be expected that as cells go through interphase and start synthesizing chromosomes, lamin levels should increase with time so as to provide more surface area for the larger nucleus.

Quantifying lamin levels in cells synchronized at different points of the cell cycle using quantitative immunoblotting or RT-qPCR will help address these types of questions.

A further challenge to the nuclear drop model is as follows. We showed in Chapter 3 that a rapid deformation of the nucleus in ~15 s with ~ 1-micron tip of a Tungsten microneedle produced shapes that resembled kidney-bean-like morphologies, in contrast to the slower deformations around the microposts over tens of minutes during migration, that produced invaginations closely wrapped around the nucleus. These differences in shape can be explained by a mechanical resistance to a strain of the nuclear interior on the shorter time scale but a uniform nuclear pressure balanced by surface tension on the longer time scale. An experiment to further challenge this explanation is to perform indentations of the nucleus with a microneedle at slower rates, i.e., over time scales similar to the time scales of migration. A current challenge associated with this experiment in our setup is that we lack computerized control of the movement of the microneedle or alternatively the microscope stage. Currently, we use a manual joystick to move the microneedle relative to the nucleus. A programmed movement of either the microneedle or the stage may provide a solution to this problem; however, because the cells are free to migrate in a 2-D plane, this experimental setup may introduce more complexity. One solution is to prevent the cells from migrating away from the microneedle by performing experiments on micropatterned cells; these cells are not free to move away from the needle as they are constrained by the lack of ECM proteins outside the micropatterned spot.

While our work in Chapter 3 focused solely on the nuclear lamina, chromatin is equally important in determining the drop-like deformation of the nucleus because it is the source of the pressure on the lamina. Condensation or decompaction of DNA by treatment are predicted to decrease or increase, respectively, the pressure inside the nucleus [5]. Treatment with histone

acetyltransferase (HAT) inhibitors like Vorinostat, Romidepsin, Panobinostat, and Belinostat or DNA methyltransferase (DNMT) inhibitors like Decitabine and Azacytidine causes an increase in heterochromatin by inhibiting the acetylation or demethylation of chromatin respectively. As we have demonstrated that a decrease in lamin A/C levels causes nuclear entanglement against obstacles, we predict that condensation of the chromatin in the nucleus will likewise entangle nuclei on the posts owing to a reduction in pressure and hence the lamin A/C tension. Dynamics of nuclear deformation and migration studies of cells treated with these inhibitors on microposts may help better understand the mechanical behavior of the nucleus.

REFERENCES


1 McGregor, A. L., Hsia, C. R. & Lammerding, J. Squish and squeeze-the nucleus as a physical barrier during migration in confined environments. *Curr Opin Cell Biol* **40**, 32-40, doi:10.1016/j.ceb.2016.01.011 (2016).

2 Wolf, K., Te Lindert, M., Krause, M., Alexander, S., Te Riet, J., Willis, A. L., Hoffman, R. M., Figdor, C. G., Weiss, S. J. & Friedl, P. Physical limits of cell migration: control by ECM space and nuclear deformation and tuning by proteolysis and traction force. *J Cell Biol* **201**, 1069-1084, doi:10.1083/jcb.201210152 (2013).

3 Stephens, A. D., Banigan, E. J., Adam, S. A., Goldman, R. D. & Marko, J. F. Chromatin and lamin A determine two different mechanical response regimes of the cell nucleus. *Mol Biol Cell* **28**, 1984-1996, doi:10.1091/mbc.E16-09-0653 (2017).

4 Stephens, A. D., Banigan, E. J. & Marko, J. F. Chromatin's physical properties shape the nucleus and its functions. *Curr Opin Cell Biol* **58**, 76-84, doi:10.1016/j.ceb.2019.02.006 (2019).

5 Stephens, A. D., Liu, P. Z., Banigan, E. J., Almassalha, L. M., Backman, V., Adam, S. A., Goldman, R. D. & Marko, J. F. Chromatin histone modifications and rigidity affect nuclear morphology independent of lamins. *Mol Biol Cell* **29**, 220-233, doi:10.1091/mbc.E17-06-0410 (2018).

6 Dubik, N. & Mai, S. Lamin A/C: Function in Normal and Tumor Cells. *Cancers (Basel)* **12**, 3688, doi:10.3390/cancers12123688 (2020).

7 Lammerding, J., Schulze, P. C., Takahashi, T., Kozlov, S., Sullivan, T., Kamm, R. D., Stewart, C. L. & Lee, R. T. Lamin A/C deficiency causes defective nuclear mechanics and mechanotransduction. *J Clin Invest* **113**, 370-378, doi:10.1172/JCI19670 (2004).

8 Lammerding, J., Fong, L. G., Ji, J. Y., Reue, K., Stewart, C. L., Young, S. G. & Lee, R. T. Lamins A and C but not lamin B1 regulate nuclear mechanics. *J Biol Chem* **281**, 25768-25780, doi:10.1074/jbc.M513511200 (2006).

9 Neelam, S., Hayes, P. R., Zhang, Q., Dickinson, R. B. & Lele, T. P. Vertical uniformity of cells and nuclei in epithelial monolayers. *Sci Rep* **6**, 19689, doi:10.1038/srep19689 (2016).

10 Davidson, P. M. & Lammerding, J. Broken nuclei--lamins, nuclear mechanics, and disease. *Trends Cell Biol* **24**, 247-256, doi:10.1016/j.tcb.2013.11.004 (2014).

11 Schreiber, K. H. & Kennedy, B. K. When lamins go bad: nuclear structure and disease. *Cell* **152**, 1365-1375, doi:10.1016/j.cell.2013.02.015 (2013).

12 Buxboim, A., Swift, J., Irianto, J., Spinler, K. R., Dingal, P. C., Athirasala, A., Kao, Y. R., Cho, S., Harada, T., Shin, J. W. & Discher, D. E. Matrix elasticity regulates lamin-A,C phosphorylation and turnover with feedback to actomyosin. *Curr Biol* **24**, 1909-1917, doi:10.1016/j.cub.2014.07.001 (2014).

13 Swift, J., Ivanovska, I. L., Buxboim, A., Harada, T., Dingal, P. C., Pinter, J., Pajerowski, J. D., Spinler, K. R., Shin, J. W., Tewari, M., Rehfeldt, F., Speicher, D. W. & Discher, D.

E. Nuclear lamin-A scales with tissue stiffness and enhances matrix-directed differentiation. *Science* **341**, 1240104, doi:10.1126/science.1240104 (2013).

14 Denais, C. M., Gilbert, R. M., Isermann, P., McGregor, A. L., te Lindert, M., Weigelin, B., Davidson, P. M., Friedl, P., Wolf, K. & Lammerding, J. Nuclear envelope rupture and repair during cancer cell migration. *Science* **352**, 353-358, doi:10.1126/science.aad7297 (2016).

15 Nader, G. P. F., Aguera-Gonzalez, S., Routet, F., Gratia, M., Maurin, M., Cancila, V., Cadart, C., Palamidessi, A., Ramos, R. N., San Roman, M., Gentili, M., Yamada, A., Williart, A., Lodillinsky, C., Lagoutte, E., Villard, C., Viovy, J. L., Tripodo, C., Galon, J., Scita, G., Manel, N., Chavrier, P. & Piel, M. Compromised nuclear envelope integrity drives TREX1-dependent DNA damage and tumor cell invasion. *Cell* **184**, 5230-5246 e5222, doi:10.1016/j.cell.2021.08.035 (2021).

16 Alam, S. G., Lovett, D., Kim, D. I., Roux, K. J., Dickinson, R. B. & Lele, T. P. The nucleus is an intracellular propagator of tensile forces in NIH 3T3 fibroblasts. *J Cell Sci* **128**, 1901-1911, doi:10.1242/jcs.161703 (2015).

17 Wu, J., Kent, I. A., Shekhar, N., Chancellor, T. J., Mendonca, A., Dickinson, R. B. & Lele, T. P. Actomyosin pulls to advance the nucleus in a migrating tissue cell. *Biophys J* **106**, 7-15, doi:10.1016/j.bpj.2013.11.4489 (2014).

18 Wang, N., Butler, J. P. & Ingber, D. E. Mechanotransduction across the cell surface and through the cytoskeleton. *Science* **260**, 1124-1127, doi:10.1126/science.7684161 (1993).

19 Sims, J. R., Karp, S. & Ingber, D. E. Altering the cellular mechanical force balance results in integrated changes in cell, cytoskeletal and nuclear shape. *J Cell Sci* **103 ( Pt 4)**, 1215-1222, doi:10.1242/jcs.103.4.1215 (1992).

20 Pajerowski, J. D., Dahl, K. N., Zhong, F. L., Sammak, P. J. & Discher, D. E. Physical plasticity of the nucleus in stem cell differentiation. *Proc Natl Acad Sci U S A* **104**, 15619-15624, doi:10.1073/pnas.0702576104 (2007).

21 Dahl, K. N., Engler, A. J., Pajerowski, J. D. & Discher, D. E. Power-law rheology of isolated nuclei with deformation mapping of nuclear substructures. *Biophys J* **89**, 2855-2864, doi:10.1529/biophysj.105.062554 (2005).

22 Versaevel, M., Braquenier, J. B., Riaz, M., Grevesse, T., Lantoine, J. & Gabriele, S. Super-resolution microscopy reveals LINC complex recruitment at nuclear indentation sites. *Sci Rep* **4**, 7362, doi:10.1038/srep07362 (2014).

23 Tocco, V. J., Li, Y., Christopher, K. G., Matthews, J. H., Aggarwal, V., Paschall, L., Luesch, H., Licht, J. D., Dickinson, R. B. & Lele, T. P. The nucleus is irreversibly shaped by motion of cell boundaries in cancer and non-cancer cells. *J Cell Physiol* **233**, 1446-1454, doi:10.1002/jcp.26031 (2018).

24 Khatau, S. B., Hale, C. M., Stewart-Hutchinson, P. J., Patel, M. S., Stewart, C. L., Searson, P. C., Hodzic, D. & Wirtz, D. A perinuclear actin cap regulates nuclear shape. *Proc Natl Acad Sci U S A* **106**, 19017-19022, doi:10.1073/pnas.0908686106 (2009).

25 Vishavkarma, R., Raghavan, S., Kuyyamudi, C., Majumder, A., Dhawan, J. & Pullarkat, P. A. Role of actin filaments in correlating nuclear shape and cell spreading. *PLoS One* **9**, e107895, doi:10.1371/journal.pone.0107895 (2014).

26 Alisafaei, F., Jokhun, D. S., Shivashankar, G. V. & Shenoy, V. B. Regulation of nuclear architecture, mechanics, and nucleocytoplasmic shuttling of epigenetic factors by cell geometric constraints. *Proc Natl Acad Sci U S A* **116**, 13200-13209, doi:10.1073/pnas.1902035116 (2019).

27 Li, Y., Lovett, D., Zhang, Q., Neelam, S., Kuchibhotla, R. A., Zhu, R., Gundersen, G. G., Lele, T. P. & Dickinson, R. B. Moving Cell Boundaries Drive Nuclear Shaping during Cell Spreading. *Biophys J* **109**, 670-686, doi:10.1016/j.bpj.2015.07.006 (2015).

28 Hatch, E. M. & Hetzer, M. W. Nuclear envelope rupture is induced by actin-based nucleus confinement. *J Cell Biol* **215**, 27-36, doi:10.1083/jcb.201603053 (2016).

29 De Vos, W. H., Houben, F., Kamps, M., Malhas, A., Verheyen, F., Cox, J., Manders, E. M., Verstraeten, V. L., van Steensel, M. A., Marcelis, C. L., van den Wijngaard, A., Vaux, D. J., Ramaekers, F. C. & Broers, J. L. Repetitive disruptions of the nuclear envelope invoke temporary loss of cellular compartmentalization in laminopathies. *Hum Mol Genet* **20**, 4175-4186, doi:10.1093/hmg/ddr344 (2011).

30 Mackenzie, K. J., Carroll, P., Martin, C. A., Murina, O., Fluteau, A., Simpson, D. J., Olova, N., Sutcliffe, H., Rainger, J. K., Leitch, A., Osborn, R. T., Wheeler, A. P., Nowotny, M., Gilbert, N., Chandra, T., Reijns, M. A. M. & Jackson, A. P. cGAS surveillance of micronuclei links genome instability to innate immunity. *Nature* **548**, 461-465, doi:10.1038/nature23449 (2017).

31 Davidson, P. M., Sliz, J., Isermann, P., Denais, C. & Lammerding, J. Design of a microfluidic device to quantify dynamic intra-nuclear deformation during cell migration through confining environments. *Integr Biol (Camb)* **7**, 1534-1546, doi:10.1039/c5ib00200a (2015).

32 Zheng, R., Ghirlando, R., Lee, M. S., Mizuuchi, K., Krause, M. & Craigie, R. Barrier-to-autointegration factor (BAF) bridges DNA in a discrete, higher-order nucleoprotein complex. *Proc Natl Acad Sci U S A* **97**, 8997-9002, doi:10.1073/pnas.150240197 (2000).

33 Lele, T. P., Dickinson, R. B. & Gundersen, G. G. Mechanical principles of nuclear shaping and positioning. *J Cell Biol* **217**, 3330-3342, doi:10.1083/jcb.201804052 (2018).

34 Uhler, C. & Shivashankar, G. V. Nuclear Mechanopathology and Cancer Diagnosis. *Trends Cancer* **4**, 320-331, doi:10.1016/j.trecan.2018.02.009 (2018).

35 Denais, C. & Lammerding, J. Nuclear mechanics in cancer. *Adv Exp Med Biol* **773**, 435-470, doi:10.1007/978-1-4899-8032-8_20 (2014).

36 Edens, L. J., White, K. H., Jevtic, P., Li, X. & Levy, D. L. Nuclear size regulation: from single cells to development and disease. *Trends Cell Biol* **23**, 151-159, doi:10.1016/j.tcb.2012.11.004 (2013).

37 Levy, D. L. & Heald, R. Mechanisms of intracellular scaling. *Annu Rev Cell Dev Biol* **28**, 113-135, doi:10.1146/annurev-cellbio-092910-154158 (2012).

38 Neumann, F. R. & Nurse, P. Nuclear size control in fission yeast. *J Cell Biol* **179**, 593-600, doi:10.1083/jcb.200708054 (2007).

39 Jorgensen, P., Edgington, N. P., Schneider, B. L., Rupes, I., Tyers, M. & Futcher, B. The size of the nucleus increases as yeast cells grow. *Mol Biol Cell* **18**, 3523-3532, doi:10.1091/mbc.e06-10-0973 (2007).

40 Hara, Y. & Merten, C. A. Dynein-Based Accumulation of Membranes Regulates Nuclear Expansion in Xenopus laevis Egg Extracts. *Dev Cell* **33**, 562-575, doi:10.1016/j.devcel.2015.04.016 (2015).

41 Levy, D. L. & Heald, R. Nuclear size is regulated by importin alpha and Ntf2 in Xenopus. *Cell* **143**, 288-298, doi:10.1016/j.cell.2010.09.012 (2010).

42 Guo, M., Pegoraro, A. F., Mao, A., Zhou, E. H., Arany, P. R., Han, Y., Burnette, D. T., Jensen, M. H., Kasza, K. E., Moore, J. R., Mackintosh, F. C., Fredberg, J. J., Mooney, D. J., Lippincott-Schwartz, J. & Weitz, D. A. Cell volume change through water efflux impacts cell stiffness and stem cell fate. *Proc Natl Acad Sci U S A* **114**, E8618-E8627, doi:10.1073/pnas.1705179114 (2017).

43 Finan, J. D. & Guilak, F. The effects of osmotic stress on the structure and function of the cell nucleus. *J Cell Biochem* **109**, 460-467, doi:10.1002/jcb.22437 (2010).

44 Kim, D. H., Li, B., Si, F., Phillip, J. M., Wirtz, D. & Sun, S. X. Volume regulation and shape bifurcation in the cell nucleus. *J Cell Sci* **129**, 457, doi:10.1242/jcs.185173 (2016).

45 Munevar, S., Wang, Y. & Dembo, M. Traction force microscopy of migrating normal and H-ras transformed 3T3 fibroblasts. *Biophys J* **80**, 1744-1757, doi:10.1016/s0006-3495(01)76145-0 (2001).

46 Munevar, S., Wang, Y. L. & Dembo, M. Distinct roles of frontal and rear cell-substrate adhesions in fibroblast migration. *Mol Biol Cell* **12**, 3947-3954, doi:10.1091/mbc.12.12.3947 (2001).

47 Naetar, N., Ferraioli, S. & Foisner, R. Lamins in the nuclear interior - life outside the lamina. *J Cell Sci* **130**, 2087-2096, doi:10.1242/jcs.203430 (2017).

48 Kimura, H. & Cook, P. R. Kinetics of core histones in living human cells: little exchange of H3 and H4 and some rapid exchange of H2B. *J Cell Biol* **153**, 1341-1353, doi:10.1083/jcb.153.7.1341 (2001).

49 Zhang, Q., Kota, K. P., Alam, S. G., Nickerson, J. A., Dickinson, R. B. & Lele, T. P. Coordinated Dynamics of RNA Splicing Speckles in the Nucleus. *J Cell Physiol* **231**, 1269-1275, doi:10.1002/jcp.25224 (2016).

50 Versaevel, M., Grevesse, T. & Gabriele, S. Spatial coordination between cell and nuclear shape within micropatterned endothelial cells. *Nat Commun* **3**, 671, doi:10.1038/ncomms1668 (2012).

51 Finan, J. D., Leddy, H. A. & Guilak, F. Osmotic stress alters chromatin condensation and nucleocytoplasmic transport. *Biochem Biophys Res Commun* **408**, 230-235, doi:10.1016/j.bbrc.2011.03.131 (2011).

52 Finan, J. D., Chalut, K. J., Wax, A. & Guilak, F. Nonlinear osmotic properties of the cell nucleus. *Ann Biomed Eng* **37**, 477-491, doi:10.1007/s10439-008-9618-5 (2009).

53 Kumar, S., Maxwell, I. Z., Heisterkamp, A., Polte, T. R., Lele, T. P., Salanga, M., Mazur, E. & Ingber, D. E. Viscoelastic retraction of single living stress fibers and its impact on cell shape, cytoskeletal organization, and extracellular matrix mechanics. *Biophys J* **90**, 3762-3773, doi:10.1529/biophysj.105.071506 (2006).

54 Roca-Cusachs, P., Alcaraz, J., Sunyer, R., Samitier, J., Farre, R. & Navajas, D. Micropatterning of single endothelial cell shape reveals a tight coupling between nuclear

volume in G1 and proliferation. *Biophys J* **94**, 4984-4995, doi:10.1529/biophysj.107.116863 (2008).

55 Chan, C. J., Ekpenyong, A. E., Golfier, S., Li, W., Chalut, K. J., Otto, O., Elgeti, J., Guck, J. & Lautenschlager, F. Myosin II Activity Softens Cells in Suspension. *Biophys J* **108**, 1856-1869, doi:10.1016/j.bpj.2015.03.009 (2015).

56 Uhler, C. & Shivashankar, G. V. Regulation of genome organization and gene expression by nuclear mechanotransduction. *Nat Rev Mol Cell Biol* **18**, 717-727, doi:10.1038/nrm.2017.101 (2017).

57 Edmondson, R., Broglie, J. J., Adcock, A. F. & Yang, L. in *Assay Drug Dev Technol* Vol. 12 207-218 (2014).

58 Antoni, D., Burckel, H., Josset, E. & Noel, G. in *Int J Mol Sci* Vol. 16 5517-5527 (2015).

59 Sieh, S., Taubenberger, A. V., Rizzi, S. C., Sadowski, M., Lehman, M. L., Rockstroh, A., An, J. Y., Clements, J. A., Nelson, C. C. & Hutmacher, D. W. Phenotypic Characterization of Prostate Cancer LNCaP Cells Cultured within a Bioengineered Microenvironment. *Plos One* **7**, e40217, doi:ARTNe4021710.1371/journal.pone.0040217 (2012).

60 Luca, A. C., Mersch, S., Deenen, R., Schmidt, S., Messner, I., Schafer, K. L., Baldus, S. E., Huckenbeck, W., Piekorz, R. P., Knoefel, W. T., Krieg, A. & Stoecklein, N. H. Impact of the 3D microenvironment on phenotype, gene expression, and EGFR inhibition of colorectal cancer cell lines. *PLoS One* **8**, e59689, doi:10.1371/journal.pone.0059689 (2013).

61 Gibbs, C. P., Kukekov, V. G., Reith, J. D., Tchigrinova, O., Suslov, O. N., Scott, E. W., Ghivizzani, S. C., Ignatova, T. N. & Steindler, D. A. Stem-like cells in bone sarcomas: implications for tumorigenesis. *Neoplasia* **7**, 967-976, doi:10.1593/neo.05394 (2005).

62 Tajik, A., Zhang, Y., Wei, F., Sun, J., Jia, Q., Zhou, W., Singh, R., Khanna, N., Belmont, A. S. & Wang, N. Transcription upregulation via force-induced direct stretching of chromatin. *Nat Mater* **15**, 1287-1296, doi:10.1038/nmat4729 (2016).

63 Irianto, J., Xia, Y., Pfeifer, C. R., Greenberg, R. A. & Discher, D. E. As a Nucleus Enters a Small Pore, Chromatin Stretches and Maintains Integrity, Even with DNA Breaks. *Biophys J* **112**, 446-449, doi:10.1016/j.bpj.2016.09.047 (2017).

64 Halfmann, C. T., Sears, R. M., Katiyar, A., Busselman, B. W., Aman, L. K., Zhang, Q., O'Bryan, C. S., Angelini, T. E., Lele, T. P. & Roux, K. J. Repair of nuclear ruptures requires barrier-to-autointegration factor. *J Cell Biol* **218**, 2136-2149, doi:10.1083/jcb.201901116 (2019).

65 Raab, M., Gentili, M., de Belly, H., Thiam, H. R., Vargas, P., Jimenez, A. J., Lautenschlaeger, F., Voituriez, R., Lennon-Dumenil, A. M., Manel, N. & Piel, M. ESCRT III repairs nuclear envelope ruptures during cell migration to limit DNA damage and cell death. *Science* **352**, 359-362, doi:10.1126/science.aad7611 (2016).

66 Pfeifer, C. R., Xia, Y., Zhu, K., Liu, D., Irianto, J., Garcia, V. M. M., Millan, L. M. S., Niese, B., Harding, S., Deviri, D., Greenberg, R. A. & Discher, D. E. Constricted migration increases DNA damage and independently represses cell cycle. *Mol Biol Cell* **29**, 1948-1962, doi:10.1091/mbc.E18-02-0079 (2018).

67 Imbalzano, K. M., Cohet, N., Wu, Q., Underwood, J. M., Imbalzano, A. N. & Nickerson, J. A. Nuclear shape changes are induced by knockdown of the SWI/SNF ATPase BRG1 and are independent of cytoskeletal connections. *PLoS One* **8**, e55628, doi:10.1371/journal.pone.0055628 (2013).

68 Merlo, G. R., Basolo, F., Fiore, L., Duboc, L. & Hynes, N. E. p53-dependent and p53-independent activation of apoptosis in mammary epithelial cells reveals a survival function of EGF and insulin. *J Cell Biol* **128**, 1185-1196, doi:10.1083/jcb.128.6.1185 (1995).

69 Miller, F. R., Soule, H. D., Tait, L., Pauley, R. J., Wolman, S. R., Dawson, P. J. & Heppner, G. H. Xenograft model of progressive human proliferative breast disease. *J Natl Cancer Inst* **85**, 1725-1732, doi:10.1093/jnci/85.21.1725 (1993).

70 Soule, H. D., Maloney, T. M., Wolman, S. R., Peterson, W. D., Jr., Brenz, R., McGrath, C. M., Russo, J., Pauley, R. J., Jones, R. F. & Brooks, S. C. Isolation and characterization of a spontaneously immortalized human breast epithelial cell line, MCF-10. *Cancer Res* **50**, 6075-6086 (1990).

71 Csucs, G., Michel, R., Lussi, J. W., Textor, M. & Danuser, G. Microcontact printing of novel co-polymers in combination with proteins for cell-biological applications. *Biomaterials* **24**, 1713-1720, doi:10.1016/s0142-9612(02)00568-9 (2003).

72 Thery, M. & Piel, M. Adhesive micropatterns for cells: a microcontact printing protocol. *Cold Spring Harb Protoc* **2009**, pdb prot5255, doi:10.1101/pdb.prot5255 (2009).

73 Schindelin, J., Arganda-Carreras, I., Frise, E., Kaynig, V., Longair, M., Pietzsch, T., Preibisch, S., Rueden, C., Saalfeld, S., Schmid, B., Tinevez, J. Y., White, D. J., Hartenstein, V., Eliceiri, K., Tomancak, P. & Cardona, A. Fiji: an open-source platform for biological-image analysis. *Nat Methods* **9**, 676-682, doi:10.1038/nmeth.2019 (2012).

74 Thiam, H. R., Vargas, P., Carpi, N., Crespo, C. L., Raab, M., Terriac, E., King, M. C., Jacobelli, J., Alberts, A. S., Stradal, T., Lennon-Dumenil, A. M. & Piel, M. Perinuclear Arp2/3-driven actin polymerization enables nuclear deformation to facilitate cell migration through complex environments. *Nat Commun* **7**, 10997, doi:10.1038/ncomms10997 (2016).

75 Jia, Z., Barbier, L., Stuart, H., Amraei, M., Pelech, S., Dennis, J. W., Metalnikov, P., O'Donnell, P. & Nabi, I. R. Tumor cell pseudopodial protrusions. Localized signaling domains coordinating cytoskeleton remodeling, cell adhesion, glycolysis, RNA translocation, and protein translation. *J Biol Chem* **280**, 30564-30573, doi:10.1074/jbc.M501754200 (2005).

76 Beadle, C., Assanah, M. C., Monzo, P., Vallee, R., Rosenfeld, S. S. & Canoll, P. The role of myosin II in glioma invasion of the brain. *Mol Biol Cell* **19**, 3357-3368, doi:10.1091/mbc.E08-03-0319 (2008).

77 Friedl, P., Wolf, K. & Lammerding, J. Nuclear mechanics during cell migration. *Curr Opin Cell Biol* **23**, 55-64, doi:10.1016/j.ceb.2010.10.015 (2011).

78 Xia, Y., Pfeifer, C. R. & Discher, D. E. Nuclear mechanics during and after constricted migration. *Acta Mechanica Sinica* **35**, 299-308, doi:10.1007/s10409-018-00836-9 (2019).

79 Nader, G. P. F., Williart, A. & Piel, M. Nuclear deformations, from signaling to perturbation and damage. *Curr Opin Cell Biol* **72**, 137-145, doi:10.1016/j.ceb.2021.07.008 (2021).

80 Broers, J. L., Peeters, E. A., Kuijpers, H. J., Endert, J., Bouten, C. V., Oomens, C. W., Baaijens, F. P. & Ramaekers, F. C. Decreased mechanical stiffness in LMNA-/- cells is caused by defective nucleo-cytoskeletal integrity: implications for the development of laminopathies. *Hum Mol Genet* **13**, 2567-2580, doi:10.1093/hmg/ddh295 (2004).

81 Schape, J., Prausse, S., Radmacher, M. & Stick, R. Influence of lamin A on the mechanical properties of amphibian oocyte nuclei measured by atomic force microscopy. *Biophys J* **96**, 4319-4325, doi:10.1016/j.bpj.2009.02.048 (2009).

82 Raab, M., Swift, J., Dingal, P. C., Shah, P., Shin, J. W. & Discher, D. E. Crawling from soft to stiff matrix polarizes the cytoskeleton and phosphoregulates myosin-II heavy chain. *J Cell Biol* **199**, 669-683, doi:10.1083/jcb.201205056 (2012).

83 Davidson, P. M., Denais, C., Bakshi, M. C. & Lammerding, J. Nuclear deformability constitutes a rate-limiting step during cell migration in 3-D environments. *Cell Mol Bioeng* **7**, 293-306, doi:10.1007/s12195-014-0342-y (2014).

84 Neelam, S., Chancellor, T. J., Li, Y., Nickerson, J. A., Roux, K. J., Dickinson, R. B. & Lele, T. P. Direct force probe reveals the mechanics of nuclear homeostasis in the mammalian cell. *Proc Natl Acad Sci U S A* **112**, 5720-5725, doi:10.1073/pnas.1502111112 (2015).

85 Bell, E. S., Shah, P., Zuela-Sopilniak, N., Kim, D., McGregor, A. L., Isermann, P., Davidson, P. M., Elacqua, J. J., Lakins, J. N., Vahdat, L., Weaver, V. M., Smolka, M. B., Span, P. N. & Lammerding, J. Low lamin A levels enhance confined cell migration and metastatic capacity in breast cancer. *bioRxiv*, 2021.2007.2012.451842, doi:10.1101/2021.07.12.451842 (2021).

86 Vortmeyer-Krause, M., Lindert, M. t., Riet, J. t., Boekhorst, V. t., Marke, R., Perera, R., Isermann, P., van Oorschot, T., Zwerger, M., Yang, F., Svoreň, M., Madzvamuse, A., Lammerding, J., Friedl, P. & Wolf, K. Lamin B2 follows lamin A/C- mediated nuclear mechanics and cancer cell invasion efficacy. *bioRxiv*, 2020.2004.2007.028969, doi:10.1101/2020.04.07.028969 (2020).

87 Frantz, C., Stewart, K. M. & Weaver, V. M. The extracellular matrix at a glance. *J Cell Sci* **123**, 4195-4200, doi:10.1242/jcs.023820 (2010).

88 Young, A. M., Gunn, A. L. & Hatch, E. M. BAF facilitates interphase nuclear membrane repair through recruitment of nuclear transmembrane proteins. *Mol Biol Cell* **31**, 1551-1560, doi:10.1091/mbc.E20-01-0009 (2020).

89 Zhang, Q., Tamashunas, A. C., Agrawal, A., Torbati, M., Katiyar, A., Dickinson, R. B., Lammerding, J. & Lele, T. P. Local, transient tensile stress on the nuclear membrane causes membrane rupture. *Mol Biol Cell* **30**, 899-906, doi:10.1091/mbc.E18-09-0604 (2019).

90 Lammerding, J. Mechanics of the nucleus. *Compr Physiol* **1**, 783-807, doi:10.1002/cphy.c100038 (2011).

91 Liu, H., Wen, J., Xiao, Y., Liu, J., Hopyan, S., Radisic, M., Simmons, C. A. & Sun, Y. In situ mechanical characterization of the cell nucleus by atomic force microscopy. *ACS Nano* **8**, 3821-3828, doi:10.1021/nn500553z (2014).

92 Beicker, K., O'Brien, E. T., 3rd, Falvo, M. R. & Superfine, R. Vertical Light Sheet Enhanced Side-View Imaging for AFM Cell Mechanics Studies. *Sci Rep* **8**, 1504, doi:10.1038/s41598-018-19791-3 (2018).

93 Hobson, C. M., Kern, M., O'Brien, E. T., 3rd, Stephens, A. D., Falvo, M. R. & Superfine, R. Correlating nuclear morphology and external force with combined atomic force microscopy and light sheet imaging separates roles of chromatin and lamin A/C in nuclear mechanics. *Mol Biol Cell* **31**, 1788-1801, doi:10.1091/mbc.E20-01-0073 (2020).

94 Dickinson, R. B., Katiyar, A., Dubell, C. R. & Lele, T. P. Viscous shaping of the compliant cell nucleus. *APL Bioeng* **6**, 010901, doi:10.1063/5.0071652 (2022).

95 Kochin, V., Shimi, T., Torvaldson, E., Adam, S. A., Goldman, A., Pack, C. G., Melo-Cardenas, J., Imanishi, S. Y., Goldman, R. D. & Eriksson, J. E. Interphase phosphorylation of lamin A. *J Cell Sci* **127**, 2683-2696, doi:10.1242/jcs.141820 (2014).

96 Guilak, F., Tedrow, J. R. & Burgkart, R. Viscoelastic properties of the cell nucleus. *Biochem Biophys Res Commun* **269**, 781-786, doi:10.1006/bbrc.2000.2360 (2000).

97 Ivanovska, I., Swift, J., Harada, T., Pajerowski, J. D. & Discher, D. E. Physical plasticity of the nucleus and its manipulation. *Methods Cell Biol* **98**, 207-220, doi:10.1016/S0091-679X(10)98009-6 (2010).

98 Shin, J. W., Spinler, K. R., Swift, J., Chasis, J. A., Mohandas, N. & Discher, D. E. Lamins regulate cell trafficking and lineage maturation of adult human hematopoietic cells. *Proc Natl Acad Sci U S A* **110**, 18892-18897, doi:10.1073/pnas.1304996110 (2013).

99 Harada, T., Swift, J., Irianto, J., Shin, J. W., Spinler, K. R., Athirasala, A., Diegmiller, R., Dingal, P. C., Ivanovska, I. L. & Discher, D. E. Nuclear lamin stiffness is a barrier to 3D migration, but softness can limit survival. *J Cell Biol* **204**, 669-682, doi:10.1083/jcb.201308029 (2014).

100 Wintner, O., Hirsch-Attas, N., Schlossberg, M., Brofman, F., Friedman, R., Kupervaser, M., Kitsberg, D. & Buxboim, A. A Unified Linear Viscoelastic Model of the Cell Nucleus Defines the Mechanical Contributions of Lamins and Chromatin. *Adv Sci (Weinh)* **7**, 1901222, doi:10.1002/advs.201901222 (2020).

101 Zuela-Sopilniak, N., Bar-Sela, D., Charar, C., Wintner, O., Gruenbaum, Y. & Buxboim, A. Measuring nucleus mechanics within a living multicellular organism: Physical decoupling and attenuated recovery rate are physiological protective mechanisms of the cell nucleus under high mechanical load. *Mol Biol Cell* **31**, 1943-1950, doi:10.1091/mbc.E20-01-0085 (2020).

102 Katiyar, A., Antani, J. D., McKee, B. P., Gupta, R., Lele, P. P. & Lele, T. P. A method for direct imaging of x-z cross-sections of fluorescent samples. *J Microsc* **281**, 224-230, doi:10.1111/jmi.12965 (2021).

103 Dutov, P., Antipova, O., Varma, S., Orgel, J. P. & Schieber, J. D. Measurement of Elastic Modulus of Collagen Type I Single Fiber. *PLoS One* **11**, e0145711, doi:10.1371/journal.pone.0145711 (2016).

104 Birendra, K., May, D. G., Benson, B. V., Kim, D. I., Shivega, W. G., Ali, M. H., Faustino, R. S., Campos, A. R. & Roux, K. J. VRK2A is an A-type lamin-dependent nuclear envelope kinase that phosphorylates BAF. *Mol Biol Cell* **28**, 2241-2250, doi:10.1091/mbc.E17-03-0138 (2017).

105 Kim, Y. & Zheng, Y. Generation and characterization of a conditional deletion allele for Lmna in mice. *Biochem Biophys Res Commun* **440**, 8-13, doi:10.1016/j.bbrc.2013.08.082 (2013).

106 Guo, Y., Kim, Y., Shimi, T., Goldman, R. D. & Zheng, Y. Concentration-dependent lamin assembly and its roles in the localization of other nuclear proteins. *Mol Biol Cell* **25**, 1287-1297, doi:10.1091/mbc.E13-11-0644 (2014).

107 D'Angelo, M. A., Anderson, D. J., Richard, E. & Hetzer, M. W. Nuclear pores form de novo from both sides of the nuclear envelope. *Science* **312**, 440-443, doi:10.1126/science.1124196 (2006).

108 Kuypers, L. C., Decraemer, W. F., Dirckx, J. J. & Timmermans, J. P. A procedure to determine the correct thickness of an object with confocal microscopy in case of refractive index mismatch. *J Microsc* **218**, 68-78, doi:10.1111/j.1365-2818.2005.01457.x (2005).

109 Crocker, J. C. & Grier, D. G. Methods of digital video microscopy for colloidal studies. *J Colloid Interf Sci* **179**, 298-310, doi:DOI 10.1006/jcis.1996.0217 (1996).

110 Penfield, L., Wysolmerski, B., Mauro, M., Farhadifar, R., Martinez, M. A., Biggs, R., Wu, H. Y., Broberg, C., Needleman, D. & Bahmanyar, S. Dynein pulling forces counteract lamin-mediated nuclear stability during nuclear envelope repair. *Mol Biol Cell* **29**, 852-868, doi:10.1091/mbc.E17-06-0374 (2018).

111 Cai, M., Huang, Y., Ghirlando, R., Wilson, K. L., Craigie, R. & Clore, G. M. Solution structure of the constant region of nuclear envelope protein LAP2 reveals two LEM-domain structures: one binds BAF and the other binds DNA. *EMBO J* **20**, 4399-4407, doi:10.1093/emboj/20.16.4399 (2001).

112 Lee, K. K., Haraguchi, T., Lee, R. S., Koujin, T., Hiraoka, Y. & Wilson, K. L. Distinct functional domains in emerin bind lamin A and DNA-bridging protein BAF. *J Cell Sci* **114**, 4567-4573, doi:10.1242/jcs.114.24.4567 (2001).

113 Shumaker, D. K., Lee, K. K., Tanhehco, Y. C., Craigie, R. & Wilson, K. L. LAP2 binds to BAF.DNA complexes: requirement for the LEM domain and modulation by variable regions. *EMBO J* **20**, 1754-1764, doi:10.1093/emboj/20.7.1754 (2001).

114 Capanni, C., Squarzoni, S., Cenni, V., D'Apice, M. R., Gambineri, A., Novelli, G., Wehnert, M., Pasquali, R., Maraldi, N. M. & Lattanzi, G. Familial partial lipodystrophy, mandibuloacral dysplasia and restrictive dermopathy feature barrier-to-autointegration factor (BAF) nuclear redistribution. *Cell Cycle* **11**, 3568-3577, doi:10.4161/cc.21869 (2012).

115 Holaska, J. M., Lee, K. K., Kowalski, A. K. & Wilson, K. L. Transcriptional repressor germ cell-less (GCL) and barrier to autointegration factor (BAF) compete for binding to emerin in vitro. *J Biol Chem* **278**, 6969-6975, doi:10.1074/jbc.M208811200 (2003).

116 Montes de Oca, R., Shoemaker, C. J., Gucek, M., Cole, R. N. & Wilson, K. L. Barrier-to-autointegration factor proteome reveals chromatin-regulatory partners. *PLoS One* **4**, e7050, doi:10.1371/journal.pone.0007050 (2009).

117 Huang, Y., Cai, M., Clore, G. M. & Craigie, R. No interaction of barrier-to-autointegration factor (BAF) with HIV-1 MA, cone-rod homeobox (Crx) or MAN1-C in absence of DNA. *PLoS One* **6**, e25123, doi:10.1371/journal.pone.0025123 (2011).

118 Wang, X., Xu, S., Rivolta, C., Li, L. Y., Peng, G. H., Swain, P. K., Sung, C. H., Swaroop, A., Berson, E. L., Dryja, T. P. & Chen, S. Barrier to autointegration factor interacts with the cone-rod homeobox and represses its transactivation function. *J Biol Chem* **277**, 43288-43300, doi:10.1074/jbc.M207952200 (2002).

119 Chen, H. & Engelman, A. The barrier-to-autointegration protein is a host factor for HIV type 1 integration. *Proc Natl Acad Sci U S A* **95**, 15270-15274, doi:10.1073/pnas.95.26.15270 (1998).

120 Ibrahim, N., Wicklund, A., Jamin, A. & Wiebe, M. S. Barrier to autointegration factor (BAF) inhibits vaccinia virus intermediate transcription in the absence of the viral B1 kinase. *Virology* **444**, 363-373, doi:10.1016/j.virol.2013.07.002 (2013).

121 Jamin, A., Thunuguntla, P., Wicklund, A., Jones, C. & Wiebe, M. S. Barrier to auto integration factor becomes dephosphorylated during HSV-1 Infection and Can Act as a host defense by impairing viral DNA replication and gene expression. *PLoS One* **9**, e100511, doi:10.1371/journal.pone.0100511 (2014).

122 Lee, M. S. & Craigie, R. A previously unidentified host protein protects retroviral DNA from autointegration. *Proc Natl Acad Sci U S A* **95**, 1528-1533, doi:10.1073/pnas.95.4.1528 (1998).

123 Wiebe, M. S. & Traktman, P. Poxviral B1 kinase overcomes barrier to autointegration factor, a host defense against virus replication. *Cell Host Microbe* **1**, 187-197, doi:10.1016/j.chom.2007.03.007 (2007).

124 Gorjanacz, M., Klerkx, E. P., Galy, V., Santarella, R., Lopez-Iglesias, C., Askjaer, P. & Mattaj, I. W. Caenorhabditis elegans BAF-1 and its kinase VRK-1 participate directly in post-mitotic nuclear envelope assembly. *EMBO J* **26**, 132-143, doi:10.1038/sj.emboj.7601470 (2007).

125 Haraguchi, T., Koujin, T., Segura-Totten, M., Lee, K. K., Matsuoka, Y., Yoneda, Y., Wilson, K. L. & Hiraoka, Y. BAF is required for emerin assembly into the reforming nuclear envelope. *J Cell Sci* **114**, 4575-4585, doi:10.1242/jcs.114.24.4575 (2001).

126 Samwer, M., Schneider, M. W. G., Hoefler, R., Schmalhorst, P. S., Jude, J. G., Zuber, J. & Gerlich, D. W. DNA Cross-Bridging Shapes a Single Nucleus from a Set of Mitotic Chromosomes. *Cell* **170**, 956-972 e923, doi:10.1016/j.cell.2017.07.038 (2017).

127 Diaspro, A., Federici, F. & Robello, M. Influence of refractive-index mismatch in high-resolution three-dimensional confocal microscopy. *Appl Opt* **41**, 685-690, doi:10.1364/ao.41.000685 (2002).

128 Hell, S., Reiner, G., Cremer, C. & Stelzer, E. H. K. Aberrations in Confocal Fluorescence Microscopy Induced by Mismatches in Refractive-Index. *Journal of Microscopy* **169**, 391-405, doi:DOI 10.1111/j.1365-2818.1993.tb03315.x (1993).

129 Van Elburg, H., Kuypers, L., Decraemer, W. & Dirckx, J. J. J. o. m. Improved correction of axial geometrical distortion in index-mismatched fluorescent confocal microscopic images using high-aperture objective lenses. **228**, 45-54 (2007).

130 Feric, M., Vaidya, N., Harmon, T. S., Mitrea, D. M., Zhu, L., Richardson, T. M., Kriwacki, R. W., Pappu, R. V. & Brangwynne, C. P. Coexisting Liquid Phases Underlie Nucleolar Subcompartments. *Cell* **165**, 1686-1697, doi:10.1016/j.cell.2016.04.047 (2016).

131 Lee, G. S., Miele, L. F., Turhan, A., Lin, M., Hanidziar, D., Konerding, M. A. & Mentzer, S. J. Spatial calibration of structured illumination fluorescence microscopy using capillary tissue phantoms. *Microsc Res Tech* **72**, 85-92, doi:10.1002/jemt.20647 (2009).

132 Alam, S. G., Zhang, Q., Prasad, N., Li, Y., Chamala, S., Kuchibhotla, R., Kc, B., Aggarwal, V., Shrestha, S., Jones, A. L., Levy, S. E., Roux, K. J., Nickerson, J. A. & Lele, T. P. The mammalian LINC complex regulates genome transcriptional responses to substrate rigidity. *Sci Rep* **6**, 38063, doi:10.1038/srep38063 (2016).

133 Shiu, J. Y., Aires, L., Lin, Z. & Vogel, V. Nanopillar force measurements reveal actin-cap-mediated YAP mechanotransduction. *Nat Cell Biol* **20**, 262-271, doi:10.1038/s41556-017-0030-y (2018).

134 Patteson, A. E., Vahabikashi, A., Pogoda, K., Adam, S. A., Mandal, K., Kittisopikul, M., Sivagurunathan, S., Goldman, A., Goldman, R. D. & Janmey, P. A. Vimentin protects cells against nuclear rupture and DNA damage during migration. *J Cell Biol* **218**, 4079-4092, doi:10.1083/jcb.201902046 (2019).

135 Katiyar, A., Tocco, V. J., Li, Y., Aggarwal, V., Tamashunas, A. C., Dickinson, R. B. & Lele, T. P. Nuclear size changes caused by local motion of cell boundaries unfold the nuclear lamina and dilate chromatin and intranuclear bodies. *Soft Matter* **15**, 9310-9317, doi:10.1039/c9sm01666j (2019).

136 Kent, I. A., Zhang, Q., Katiyar, A., Li, Y., Pathak, S., Dickinson, R. B. & Lele, T. P. Apical cell protrusions cause vertical deformation of the soft cancer nucleus. *J Cell Physiol* **234**, 20675-20684, doi:10.1002/jcp.28672 (2019).

137 Keeling, M. C., Flores, L. R., Dodhy, A. H., Murray, E. R. & Gavara, N. Actomyosin and vimentin cytoskeletal networks regulate nuclear shape, mechanics and chromatin organization. *Sci Rep* **7**, 5219, doi:10.1038/s41598-017-05467-x (2017).

138 Lovett, D. B., Shekhar, N., Nickerson, J. A., Roux, K. J. & Lele, T. P. Modulation of Nuclear Shape by Substrate Rigidity. *Cell Mol Bioeng* **6**, 230-238, doi:10.1007/s12195-013-0270-2 (2013).

139 Hanson, L., Zhao, W., Lou, H. Y., Lin, Z. C., Lee, S. W., Chowdary, P., Cui, Y. & Cui, B. Vertical nanopillars for in situ probing of nuclear mechanics in adherent cells. *Nat Nanotechnol* **10**, 554-562, doi:10.1038/nnano.2015.88 (2015).

140 Hoffman, L. M., Smith, M. A., Jensen, C. C., Yoshigi, M., Blankman, E., Ullman, K. S. & Beckerle, M. C. Mechanical stress triggers nuclear remodeling and the formation of transmembrane actin nuclear lines with associated nuclear pore complexes. *Mol Biol Cell* **31**, 1774-1787, doi:10.1091/mbc.E19-01-0027 (2020).

141 Ingram, V. M. A side view of moving fibroblasts. *Nature* **222**, 641-644, doi:10.1038/222641a0 (1969).

142 Howard, J. *Mechanics of Motor Proteins and the Cytoskeleton*. (Sinauer Associates, Publishers, 2001).

143 Sheppard, C. J. R. & Torok, P. Effects of specimen refractive index on confocal imaging. *Journal of Microscopy-Oxford* **185**, 366-374, doi:DOI 10.1046/j.1365-2818.1997.d01-627.x (1997).

144 Wilson, T. & Tan, J. B. Three dimensional image reconstruction in conventional and confocal microscopy. *Bioimaging* **1**, 176-184, doi:10.1002/1361-6374(199309)1:3<176::Aid-bio6>3.0.Co;2-y (1993).

145 Sheppard, C. J. R., Choudhury, A. & Gannaway, J. Electromagnetic field near the focus of wide-angular lens and mirror systems. *IEE Journal on Microwaves, Optics and Acoustics* **1**, 129-132, doi:10.1049/ij-moa.1977.0015 (1977).

146 Sheppard, C. J. R. Axial Resolution of Confocal Fluorescence Microscopy. *Journal of Microscopy-Oxford* **154**, 237-241, doi:DOI 10.1111/j.1365-2818.1989.tb00586.x (1989).

147 North, A. J. Seeing is believing? A beginners' guide to practical pitfalls in image acquisition. *J Cell Biol* **172**, 9-18, doi:10.1083/jcb.200507103 (2006).

148 Sieck, G. C., Mantilla, C. B. & Prakash, Y. S. in *Confocal Microscopy* Vol. 307 *Methods in Enzymology* 296-315 (Academic Press, 1999).

149 Grashoff, C., Hoffman, B. D., Brenner, M. D., Zhou, R., Parsons, M., Yang, M. T., McLean, M. A., Sligar, S. G., Chen, C. S., Ha, T. & Schwartz, M. A. Measuring mechanical tension across vinculin reveals regulation of focal adhesion dynamics. *Nature* **466**, 263-266, doi:10.1038/nature09198 (2010).